TRANSFORMATIONS IN INORGANIC NANOMATERIALS: ROLE OF DEFECTS, SURFACES, AND SIZE

BY

SARAH LANGLOIS WHITE

DISSERTATION

Submitted in partial fulfillment of the requirements
for the degree of Doctor of Philosophy in Chemistry
in the Graduate College of the
University of Illinois at Urbana-Champaign, 2016

Urbana, Illinois

Doctoral Committee:

Professor Prashant K. Jain, Chair
Professor Catherine J. Murphy
Professor Moonsub Shim
Professor Yi Lu

Abstract

As our ability to synthesize and manipulate nanomaterials increases, so does our ability to investigate the properties and transformations of materials as they evolve in size from precise clusters akin to molecules to extended solids exhibiting bulk-like properties. In this thesis, we look at a how critical features of nanomaterials like size, shape, surface chemistry or ligand shell, and defect profile affect properties and transformations on the nanoscale. In Chapter 1, we investigate the mechanism of cation exchange in an ensemble of CdSe nanocrystals with Ag^+ and Cu^+ in solution. We find that the generation of defects induced by non-native cations is a critical intermediate in the exchange reaction and that positive co-operativity stemming from interactions between charged defects results in an abrupt chemical transformation of the entire nanocrystal, i.e. a particle-by-particle exchange rather than an atom-by-atom mechanism. In Chapter 2, we leverage the high sensitivity of excitonic absorption of ultrasmall CdSe clusters to changes in surface chemistry to optically probe cation exchange and identify a stable, long-lived intermediate in the cation exchange transformation. The stability of the intermediate was found to be dependent on the ligand coating on the initial clusters, leading to a better understanding of how ligand passivation can play a role in chemical reactions occurring at the solid-liquid interface. In Chapter 3, we probe how the optical and structural properties of the semiconductor, cuprous selenide are affected by a decrease in crystallite size and find an ultrasmall form of cuprous selenide in which a disordered phase, known to exist in the bulk at high temperature, is stable at ambient conditions suggesting that the order-to-disorder phase transition temperature is depressed in ultrasmall Cu_2Se clusters. Finally, in Chapters 4 and 5, we explore how the structure of metamolecules consisting of complex assemblies of hexagonal Au nanoplates and Au nanospheres affects their localized surface plasmon resonance properties. . We find using electrodynamic simulations combined with correlated electron microscopy/optical spectroscopy at the single-construct level that the nature and strength of plasmonic coupling within the resulting assembly is strongly dependent on the site of attachment of the nanosphere/s and the nanosphere size. In addition to the large, regio-selective polarizability of Au nanoplates, we also uncover a synergy in the polarizing effect of multiple nanospheres. The dissertation ends with an outlook of the scientific impact and potential future studies that may emanate from the work presented here.

Acknowledgements

This work presented in this thesis is a collection of collaborative efforts that would not have been possible without the contribution of many people. First and foremost, I must thank my adviser, Prof. Prashant Jain, who conceived of and developed the theory for much of the following work. The following studies are the product not simply of hours in the lab or at MRL, but of vast hours of discussion, emails, literature searches, whiteboard sketches, drafts, drafts_pjed, and so many figure folders. Thank you for taking me on as a graduate student, teaching me how to be an ambitious yet vigilant scientist, and teaching me how to make real connections between seemingly disparate ideas in science. Finally, more than anything, my views on data archiving will never be the same.

The work in this thesis would not have been possible without contributions from many past and present members of the Jain lab. The TEM and XPS data for my first project was collected by Jeremy Smith and Mayank Behl respectively, who continued to provide me with great TEM and XPS help and advice during my time here. The work with copper selenide clusters conducted in our lab was an ongoing effort contributed to by Alex Stanton and Progna Banerjee, the latter of who collected and analyzed the plasmonic absorption data presented in Chapter 3. Some of the early experiments on cation exchange were done by Melika Fini, an undergraduate in our lab. A good portion of this thesis involves DDA simulations using a Fortran code written and made freely available by Profs. Bruce Draine and Piotr Flatau, which I learned to perform with a lot of help from Jacob Faucheaux. The rest of the Jain group, many of whom I consider friends, provided a helpful and friendly lab environment that I have enjoyed being a part of the last five years.

I thank my collaborators: Dr. Aiqin Fang and Prof. Frank Zamborini at the University of Louisville. The data presented in Chapter 4 and 5 was the result of a collaboration with Aiqin, who collected all the experimental data, helped with analysis, and co-wrote the chapters. I thank the Frank Seitz Materials Research Laboratory for training and use of their TEM, XRD, and XPS facilities, and Dr. Rick Haasch for help with XPS data collection. I thank the George R. Clark X-ray Facility for training and use of their XRD facilities and the SCS Microanalysis Laboratory for elemental analysis.

I thank my PhD committee members: Profs. Cathy Murphy, Moonsub Shim, Yi Lu and Steve Granick for their advice and input on my research. I thank Nahil Sobh and the nanoBIO node for letting me become a part of the development and dissemination of the nanoDDSCAT tool. The Department of Chemistry has provided me with a lot of support including the Silvia Stoesser Fellowship, the J and M Witt Fellowship, and the Walter G. Klemperer Dissertation Award. I also need to thank some of the people who have helped

me greatly with the non-scientific aspects of the doctoral process including Dr. Ellen Wang Althaus, Patricia Simpson, the secretaries in the IMP office, and Connie Knight, the latter of whom I would not be graduating without because I would still have some missing research credit from my first semester here.

The occasional tedium and frustration of graduate life was made far more manageable with the help of great friends: Ariane, Elissa, Windy, Tracy, Maria, Josh, Tony, and Stephen. I need to thank my parents for being the constant voice of reason only a phone call away, and occasionally my test lay-person audience. Finally, I need to thank Max, for taking my challenges, successes, failures, and moments of complete irrationality as seriously as I did, and helping me get through them all.

Table of Contents

Chapter 1: Co-operativity in a nanocrystalline solid-state transition*

1.1 Abstract

Co-operativity is a remarkable phenomenon exhibited by several macromolecular systems, where initial reaction events significantly alter the propensity of subsequent reaction events, giving rise to a non-linear tightly regulated synergistic response. Whereas most instances are seen in biology – classic examples being oxygen-binding in hemes, protein folding/unfolding, and denaturation of nucleic acids – we have found unique evidence of atomic level co-operativity in an inorganic material. A thousand-atom nanocrystal of the inorganic solid cadmium selenide exhibits strong positive co-operativity in its ionic reaction with copper ions. The transition of a nanocrystal does not proceed until the nanocrystal has acquired copper impurities; but once a critical amount of copper doping has occurred, the nanocrystal makes a rather abrupt transition to copper selenide, which is manifested in a strongly sigmoidal response in optical spectroscopy and electron diffraction measurements. Defect luminescence measurements along with an allosteric model show that a nanocrystal doped with a few copper impurities becomes highly prone to be doped even further, driving an abrupt transition of the entire nanocrystal to the copper selenide phase. The examples presented here suggest that co-operative phenomena may play an important role in the solid-state, especially in the nucleation of new chemical phases, crystal growth, and other materials' transformations.

1.2 Introduction

Since the first observation in 1910 of the co-operative binding of oxygen to hemoglobin,[1,2] where binding at each of the four sites of hemoglobin increases the oxygen affinity of the other sites, co-operative phenomena have been displayed in a host of macromolecular systems,[3] ranging from the unwinding of DNA and protein folding[4] to self-assembly in supramolecular systems.[5] A common feature of co-operative systems is that they possess multiple binding sites with some mechanism for feedback or coupling between the binding sites. The feedback itself may be positive or negative. Positive co-operativity is manifested as an apparent all-or-nothing behavior:[6] rather than making a *gradual* progression through intermediary states, the system undergoes a relatively *abrupt* transition from the initial to the final state in response to an

* Reproduced with permission from White, S. L., Smith, J. G., Behl, M. & Jain, P. K. Co-operativity in a nanocrystalline solid-state transition. *Nat. Commun.* **4,** 2933 (2013).

extremely small change in conditions (e.g., ligand, denaturing agent, pH, or temperature). The system spends little time in the intermediary states, resulting in their low population. The strongly sigmoidal oxygen binding curve of hemoglobin is the archetypal example of such behaviour.[1]

While examples of co-operativity seem limited to macromolecules, mostly biological,[3] we found evidence of co-operative behavior in an inorganic solid material. The observation was made in nanocrystals (NCs) of cadmium selenide[7] (CdSe) undergoing a cation exchange in the presence of monovalent ions as:

$$(CdSe)_n + 2n.Cu^+_{(aq)} \leftrightharpoons (Cu_2Se)_n + n.Cd^{2+}$$

In this transformation,[8,9] the Cd^{2+} cationic sub-lattice is replaced by Cu^+ ions (two for every Cd^{2+} ion) to form a nanocrystal of cuprous selenide (Cu_2Se). Each CdSe NC is ~4 nm or ~1300 atoms in size, and loosely speaking, can be thought of as a "macromolecular system" with multiple "sites" for foreign cations. The cation exchange reaction[10] itself has received a lot of fundamental attention due to its remarkably fast (millisecond time-scale) kinetics[11] in nanosized crystals. The transformation, if well understood, can be exploited for topotaxially templated synthesis of nanostructures with novel compositions and morphologies,[12,13] designing heterojunctions in nanocrystals,[14] sensing heavy metal ions,[15] and achieving electronic doping.[16,17]

With limited mechanistic insight available, cation exchange is often assumed to be a diffusion-limited transformation: as long as the cation can diffuse to a lattice site, exchange can take place at that site. By this assumption, all lattice sites exposed to Cu^+ would have an equal affinity for exchange and the CdSe ensemble would transform in a random site-by-site manner to the Cu_2Se phase as adequate Cu^+ becomes available. However, our optical and electron diffraction measurements show that the exchange transformation does not follow such a memoryless, diffusion-limited process. Instead, we see positive co-operative behavior, where initial Cu^+ doping of a NC strongly enhances the likelihood of further Cu^+ doping within the same NC, causing the NC to transition sharply from a lightly-doped CdSe NC to the Cu_2Se phase.

1.3 Results

1.3.1 Optical probing of cation exchange

We used excitonic absorption spectra (Fig. 1.1A) to monitor the cation exchange of a solution of 4-nm CdSe NCs as it was titrated with Cu^+. With increasing Cu^+ feed concentration, the excitonic band at 2.1 eV, corresponding to the $1S_h$-$1S_e$ transition in the CdSe NCs, decreased in intensity, which is expected as the conversion to Cu_2Se proceeded. Concomitantly, the absorption in the near-infrared region associated with Cu_2Se increased. Two important features emerge in these spectra.

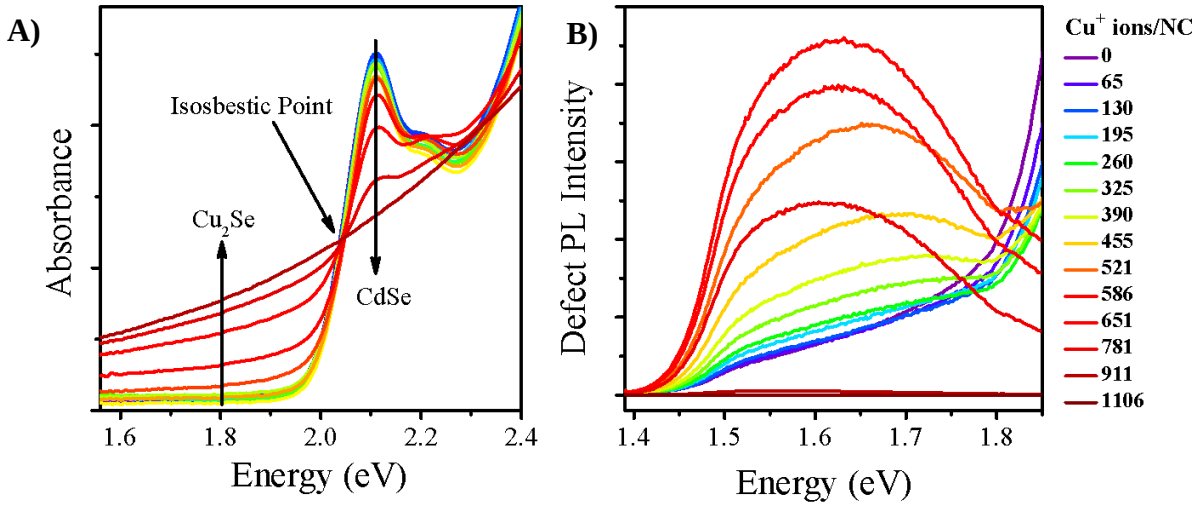

Figure 1.1 Optical monitoring of the cation exchange reaction of CdSe NCs with Cu^+ ions. *Excitonic absorption spectra* ***(A)*** *of an ensemble of CdSe NCs as a function of added Cu^+. Feed Cu^+ concentrations are denoted as the number of ions available per 1300-atom CdSe NC. With increasing addition of Cu^+, the CdSe NC exciton peak decreases without undergoing any shift. Concomitantly, the Cu_2Se absorption in the near-infrared increases. A clear isosbestic point is seen. Following complete exchange, the absorption spectrum of the NCs resembles that of Cu_2Se with a band-gap onset around 1 eV. Note, Cu_2Se is an indirect semiconductor and therefore has no excitonic band, rather only a featureless absorption above its band-gap. Photoluminescence spectra* ***(B)*** *in the sub-band gap region show the emergence of defect luminescence when Cu^+ is added, which evolves further with increasing Cu^+ feed concentration. The excitonic band-gap luminescence of CdSe was subtracted out from these spectra, as detailed in Section 1.6.2.*

First, the spectral position of the CdSe exciton stayed relatively unchanged throughout the titration, which indicates an absence[13] of any significant fraction of binary CdSe/Cu_2Se NCs formed by partial cation exchange. Such heterostructures would exhibit strongly shifted excitonic peaks, because the excitonic peak position is highly dependent on the CdSe crystallite size.[18] While it is possible that partial conversion of a CdSe NC to Cu_2Se completely quenches its excitonic absorption, this possibility is excluded by a key observation: the decrease in the fraction of CdSe NCs (estimated from the CdSe exciton height) is perfectly correlated with the increase in the fraction of Cu_2Se NCs (estimated from the Cu_2Se absorbance at 1.82 eV), as shown in Fig. 1.2.

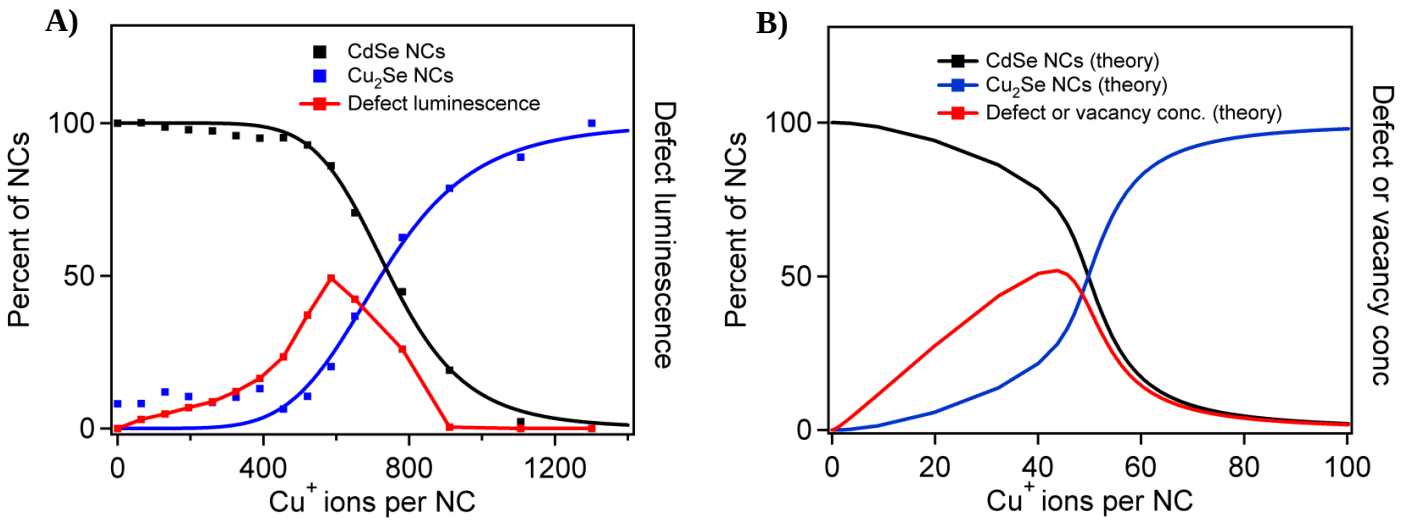

Figure 1.2 Sigmoidal nature of the cation exchange titration. ***(A)*** *Experimental plot of the fraction of NCs in the CdSe state (black dots) and those in the Cu_2Se state (blue) as a function of added Cu^+ is strikingly sigmoidal, representative of a strongly co-operative process. Below a critical concentration of ~500 Cu^+/NC, very few NCs undergo a transition to the Cu_2Se state. A fit to the Hill plot (solid black line, R=0.996) yields a co-operativity factor of n_H = 7.1. Note we use total Cu^+ concentration, although the Hill equation is strictly valid for free concentrations. The fraction of NCs in the CdSe state was determined from the height of the CdSe excitonic peak from Fig. 1.1A and the fraction in the Cu_2Se state was determined from the Cu_2Se band-to-band absorption at 1.82 eV. The procedure for analysis is described in Section 1.6.2. The rise in the Cu_2Se fraction tracks well the drop in the CdSe fraction, further confirming two-state behavior. The defect luminescence intensity (red), integrated across broad band, increased as Cu^+ was added, until it reached a maximum around the critical concentration, beyond which it decreased until it reached zero. (**B**) A theoretical simulation of a 20-site NC reproduced the observed nature of the cation exchange transformation. Sequential binding was used to model the positive co-operative behavior. The simulated fraction of Cu_2Se NCs in solution as a function of the total Cu^+ concentration, plotted as number of ions per NC, follows a strongly sigmoidal curve (blue). The fraction of all NCs in the CdSe state, either pure or doped, is also shown (black). The simulated concentration of Cu^+ dopants and associated Cd^{2+} vacancies (red) reproduces the evolution of the defect luminescence. The defect concentration reaches a maximum around the critical Cu^+ concentration, beyond which it gradually decreases to zero.*

A clear isosbestic point (Fig. 1.1A) is identified, which is a well-known indicator of a two species system, where one species converts to another over the course of the titration. Thus, it appears that individual CdSe NCs switch fully to Cu_2Se as sufficient Cu^+ becomes available. With increasing amount of Cu^+, more and more NCs make this transition from CdSe to Cu_2Se. Thus, each NC is either in the CdSe state (albeit with some Cu^+ dopants) or in the fully exchanged Cu_2Se state, manifesting the classic two-state behavior of a co-operative system.

Across a range of systems, sigmoidal binding curves are a definitive manifestation of co-operative behavior.[1] Fig. 1.2 shows such a curve for the cation exchange process: this plot of the fraction of NCs in

the CdSe state as a function of Cu^+ concentration is strikingly sigmoidal, as also is the plot of the fraction of NCs in the Cu_2Se state. Only a small to negligible fraction of NCs is exchanged at low Cu^+ feed concentrations. However, once a critical concentration is reached, a major fraction of NCs switch to the Cu_2Se state over a narrow concentration window about the critical concentration. The titration curve fits well (R = 0.996) the Hill equation,[1] with a Hill coefficient or co-operativity factor of n_H = 7. As a comparison, strongly co-operative oxygen binding by hemoglobin shows a value of n_H = 2.3-3.0. We have found some experiment-to-experiment variation in the measured n_H (range 4-7). Size/shape/surface related heterogeneities inherent to NC samples may contribute to such a variation.

1.3.2 Structural probing of cation exchange

Electron diffraction measurements (Fig. 1.3) provide structural evidence of the sharp onset of the the cation exchange process. The initial NC samples show wurtzite CdSe diffraction features, which persist up to a Cu^+ feed concentration as high as 549 ions/NC. Around this Cu^+ concentration (the half-way point), a significant fraction of NCs undergo a conversion to Cu_2Se, as indicated by the emergence of diffraction features corresponding to the tetragonal belladoite phase of Cu_2Se, albeit superimposed on wurtzite diffraction features from the remnant CdSe NCs. With further addition of Cu^+, the tetragonal Cu_2Se diffraction pattern becomes more prominent as additional NCs convert to Cu_2Se. Concomitantly, the wurtzite CdSe diffraction pattern wanes. Eventually, at about 1317 Cu^+ ions/NC (slightly higher than a full stoichiometric amount), only the tetragonal Cu_2Se diffraction pattern is seen, indicating conversion of all NCs to Cu_2Se.

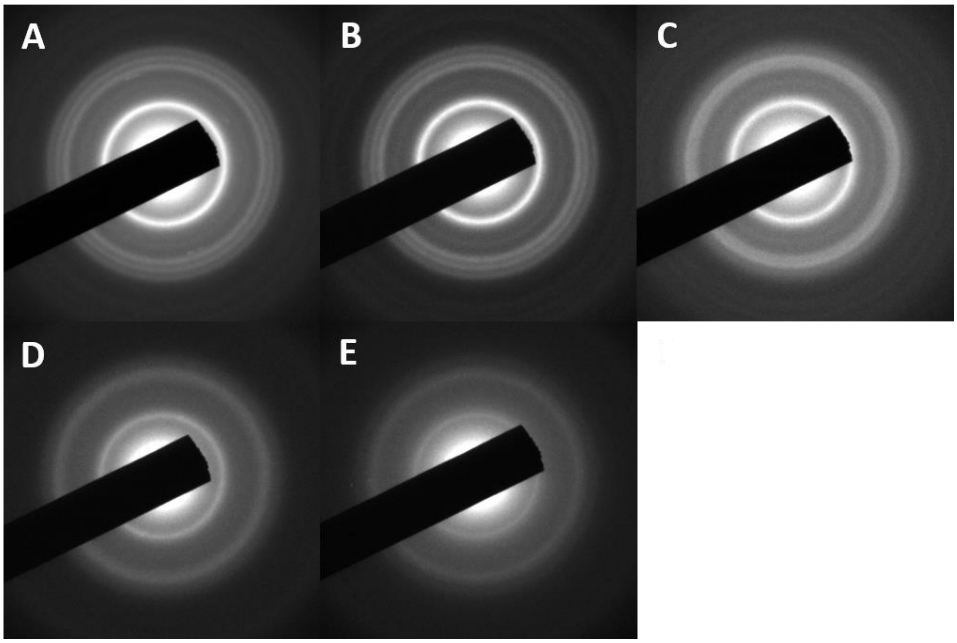

Figure 1.3 Selected-area electron diffraction (SAED) reveals the sharp onset of cation exchange. *For nanocrystals subject to 0 Cu^+ ions/NC and 384 Cu^+ ions/NC (A and B), the SAED patterns are indicative of the CdSe wurtzite (cadmoselite) structure. The innermost ring at 3.55 Å is a combination of the (100), (002), and (101) planes, which are Debye-Scherrer broadened into one ring. The three outer rings, measured at 2.15, 2.00, and 1.88 Å, match those for the (100), (103), and (200) planes of cadmosellite. In addition, there is a ring corresponding to the (102) plane, at a lattice spacing of 2.55 Å. These features are seen for samples (A-C). At 1317 Cu^+ ions/NC (in slight excess of the stoichiometric amount needed for full conversion), the tetragonal Cu_2Se phase (bellidoite) is seen (E). The highest intensity reflections include ones at 3.46 Å for the (113), (311), and (222) planes, 2.04 Å for the (404) plane, and 1.76 Å for the (226) and (533) plane. The diffraction features of Cu_2Se seem to first appear at 549 Cu^+ ions/NC, overlapped with CdSe diffraction features. As exchange progresses, CdSe diffraction features wane, until a pure bellidoite diffraction pattern is obtained for the fully converted sample. All d-spacings are determined relative to the (111) reflection of an Au standard taken under the same conditions. Samples were prepared by a slow titration of CdSe nanocrystals in toluene with increasing amounts of a methanolic solution of Cu^+, similar to the titration experiments described in the previous figures. At various points in the titration, a small aliquot was drop-casted onto an ultrathin carbon TEM grid and washed with methanol several times. The total amount of Cu^+ added is indicated in the form of number of ions per nanocrystal, estimated as described in Section 1.6.2.*

Table 1.1 *Measured lattice spacings from selected-area electron diffraction (SAED) patterns shown in Fig. 1.3.*

Sample A) 0 Cu^+/NC	**Sample B) 384 Cu^+/NC**	**Sample C) 549 Cu^+/NC**	**Sample D) 659**	**Sample E) 1317**
3.57 Å	3.57 Å	3.54 Å	3.47 Å	3.46 Å
2.55 Å	2.55 Å	2.57 Å	2.04 Å	2.04 Å
2.17 Å	2.17 Å	2.17 Å	1.77 Å	1.76 Å
2.02 Å	2.01 Å	2.05 Å		
1.88 Å	1.89 Å	1.79 Å		

1.3.3 Cu^+ doping as a precursor to exchange

In the regime below the critical concentration, it is clear that there is little conversion to Cu_2Se and most of the NCs exhibit the CdSe crystal structure. However, in this regime, the NCs are doped with Cu^+ impurities, as found from X-ray photoelectron spectroscopy (Figs. 1.4 and 1.11) and elemental analyses (Fig. 1.7). Cu^+ is a common interstitial dopant in CdSe.[19,20] It is known that such dopants do not necessarily disrupt the excitonic band or the overall crystallographic structure of CdSe,[18,19] which is consistent with our optical and electron diffraction measurements.

Cu^+ doping can, however, cause lattice defects: for instance, for every two interstitial Cu^+ impurities in a NC, charge compensation would require the formation of a Cd^{2+} vacancy. Both Cu^+ impurities and vacancies serve as mid-gap trap states and give rise to sub-bandgap luminescence,[21–24] which we employed for monitoring the doping of NCs at various stages in the cation exchange titration (Fig. 1.1B). Whereas pure CdSe NCs show no sub-bandgap luminescence, addition of Cu^+ induces a broad defect luminescence in the sub-band gap 1.4-1.8 eV region. With increasing Cu^+ feed concentration, the defect luminescence increased in intensity, as would be consistent with an increase in copper impurities and associated defects prior to the onset of cation exchange. The defect luminescence intensity reached a maximum around the critical Cu^+ concentration, beyond which it started decreasing. Such a decrease is expected from the sharp onset of cation exchange, since the transition to Cu_2Se involves mutual annihilation of Cu^+ impurities with Cd^{2+} vacancies, expressed in Kroger-Vink notation as:

$$2.Cu_{i}^{\cdot} + V_{Cd}^{x} + Se^{2-} \leftrightharpoons Cu_2Se$$

Thus, doping of a CdSe NC with Cu^+ appears to be a critical precursor to the onset of cation exchange (Fig. 1.4A). The strongest affirmation comes from two observations in Fig. 1.2A: (i) The point in the titration where the defect level reaches a maximum is coincident with the point of onset of cation exchange. (ii) The

plot of defect level as a function of feed Cu^+ concentration resembles the derivative of the sigmoidal titration curve.

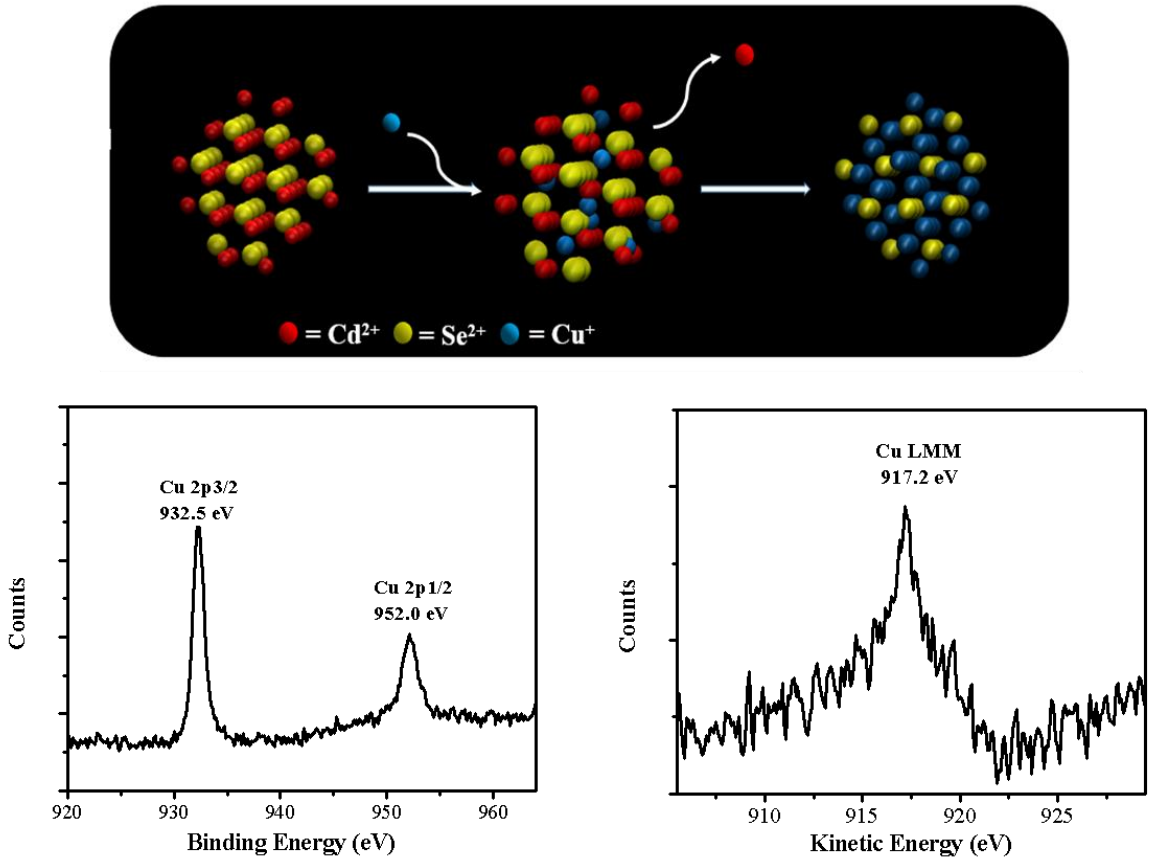

Figure 1.4 Cation exchange is preceded by doping with Cu^+. *A model of a CdSe wurtzite crystal (**top**) with ordered cadmium (red) and selenium (yellow) atoms. Below the critical concentration, the CdSe NC uptake Cu^+ (blue) in the form of interstitial dopants, in turn creating Cd^{2+} vacancies within the NC for charge compensation. These impurities and vacancies are manifested in the emergence of defect luminescence in Fig. 1.1B. Initial doping events can greatly enhance the affinity of the NC for additional Cu^+, eventually triggering a sharp transition to the Cu_2Se state. The formation of a Cu_2Se NC involves the mutual annihilation of Cu^+ dopants and Cd^{2+} vacancies, resulting in the decrease in the defect luminescence seen above the critical concentration. High resolution X-ray photoelectron spectra (XPS) of NCs (**bottom left**) treated with a copper concentration of 325 Cu^+ ions/NC. NCs were thoroughly washed with methanol to remove excess Cu^+ before measurements. The fitted peak position of the Cu 2p band (932.5 eV) is indicative of copper ions in the 1+ oxidation state. The Cu LMM peak in the X-ray induced Auger spectrum (**bottom right**), used to differentiate between Cu^{1+} and Cu^0, shows a fitted peak position of 917.2 eV, characteristic of Cu^{1+}. Additional XPS data is shown in Section 1.7.*

1.4 Discussion

The extended latent region below the critical concentration suggests that the initial incorporation of Cu^+ into the lattice is a relatively low-probability process. However, initial doping of a NC can occur stochastically, possibly at surface or defect sites of a NC. These initial doping events activate the NC for further doping. Each doping event enhances the affinity of the NC for a subsequent doping event and so on, until the NC reaches a critical state where it is likely to take up every available Cu^+ ion, resulting in a cascade of Cu^+ incorporation and an abrupt phase transition from a low doped NC to Cu_2Se. In other words, a NC already doped with Cu^+ is much more likely to take up additional Cu^+ and make a sharp transition to Cu_2Se, albeit at the expense of another NC which has acquired none or relatively few dopants. This bias represents positive co-operativity between "sites" on the same NC.

When energetic aspects of such positive co-operative behavior were included in a lattice site model (Section 1.6.1),[25] we were able to simulate all our experimental observations (Fig. 1.2B). We started with an ensemble of CdSe NCs, each with 20 bivalent sites for Cu^+. For the first doping event within any NC, the magnitude of the free energy change ΔG was assumed to be small, making it a low probability event. However, each doping event increased, by an amount Δg, the free energy change stabilization resulting from subsequent doping on the *same* NC. Thus, it is energetically more and more favorable for a NC to incorporate Cu^+ ions. This simple model reproduced the strongly sigmoidal response of the NC ensemble to added Cu^+. There was an extended latent region during which only a tiny fraction of NCs made a transition to Cu_2Se. Most of the NCs made a transition over a narrow window around a critical Cu^+ feed concentration. The simulations also reproduced the rise in the number of defects in the ensemble with increasing Cu^+ feed concentration. The number of defects reached a maximum around the critical concentration, following which it gradually decreased to zero. If there were no such positive co-operative bias (i.e., if every site in the CdSe ensemble had a similar affinity for Cu^+ regardless of whether it is on an already doped NC or an undoped one), the exchange process would be a diffusion-limited one, where each NC would exchange gradually via a continuum of intermediary $CdSe/Cu_2Se$ heterostructure states. The titration curve would be Langmuirian ($n_H = 1$) rather than sigmoidal ($n_H > 1$).

Thus, a positive co-operative model, similar to one employed in biomacromolecular systems,[26] captures the observed behavior of the cation exchange process. Nevertheless it still leaves open the question of the atomistic mechanism for co-operativity. In hemoglobin, oxygen binding at one of the heme subunits leads to a conformational change in the neighboring subunits, which increases the affinity of the neighbor site for oxygen binding, a phenomenon known as allostery.[25] Allosteric coupling between lattice sites of a NC can originate from a few different structural factors. As described earlier, due to charge compensation, Cu^+ doping results in the creation of Cd^{2+} vacancies, one vacancy for every two interstitial Cu^+ impurities. These

lattice vacancies provide hopping sites for enhanced in-diffusion of additional Cu^+ ions into the NC and out-diffusion of Cd^{2+} ions from the NC. Secondly, the local negative polarization at a Cd^{2+} vacancy site could electrostatically attract other positively charged Cu^+ ions. Thirdly, inclusion of interstitial impurities and formation of vacancies would strain the NC lattice greatly enhancing the thermodynamic driving force for Cu^+ substitutions and structural transition to Cu_2Se. Such mechanisms have been found to be operative in superionic solids.[27]

Cation exchange with another common monovalent cation Ag^+ showed similar results: a sigmoidal titration curve and a maximum in the defect luminescence intensity around the critical concentration (Fig. 1.5), indicating that the co-operative mechanism of cation exchange is not specific just to Cu^+. The Ag system appears to be less co-operative than the Cu system: the titration curve is not as steep. The Hill fit shows a value of $n_H = 3$ smaller than for Cu^+. The plot of the defect luminescence intensity as a function of feed concentration does not show a sharp peak, rather a plateau. While the physical reason for this difference is not understood, it could be due to the much larger size of Ag^+ than Cu^+. The larger Ag^+ ions may have a lower propensity to occupy interstitial sites and substitutional doping may be more prevalent than in the Cu^+ case.

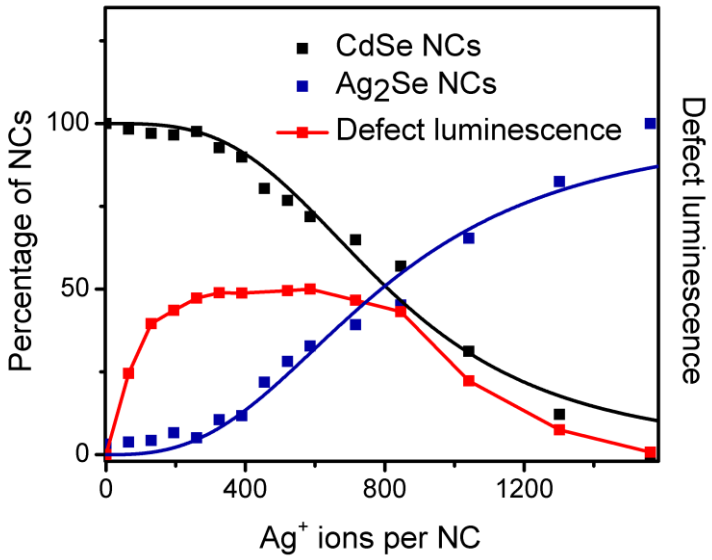

Figure 1.5 Co-operativity is also observed in the cation exchange of CdSe NCs with Ag^+, another common monovalent ion. *A plot of the fraction of NCs in the CdSe state (black dots) and those in the Ag_2Se state (blue) as a function of added Ag^+ is sigmoidal, indicative of co-operative behavior. Below a critical concentration of ~500 Ag^+/NC, very few NCs undergo a transition to the Ag_2Se state. A fit to the Hill plot (solid black line, R=0.973) yields a co-operativity factor of n_H = 3.2. The fraction of NCs in the CdSe state was determined from the height of the CdSe excitonic peak and the fraction in the Ag_2Se state was determined from the Ag_2Se band-to-band absorption at 1.82 eV. The procedure for analysis is described in Section 1.6.2. The rise in the Ag_2Se fraction tracks well the drop in the CdSe fraction. The defect luminescence intensity (red), integrated across broad band, increases as Ag^+ is added, until it reaches a maximum around the critical concentration, beyond which it decreases until it reaches zero.*

While positive co-operativity between sites of individual NCs explains all our observed results, a related mechanism is worth considering. It is possible for initial Cu^+ (or Ag^+) impurities formed within a NC to cluster together into a critical-size nucleus, initiating spontaneous growth of the Cu_2Se (or Ag_2Se) phase within the NC. This is reminiscent of the photographic development of silver iodide, where a latent four-atom nucleation cluster triggers rapid/spontaneous growth of Ag.[28–30] Such a nucleation-growth mechanism could give rise to the observed two-state behavior and the sharp sigmoidal transition. However, the topotactic nature of cation exchange[31] is not compatible with a nucleation-driven mechanism, wherein the final nanostructure morphology would be dictated by the growing nucleus, rather than by the starting ionic template.

A common feature across many co-operative systems is that each binding event pre-organizes other sites for binding, thereby reducing the number of non-productive configurations and resulting in greatly

enhanced reaction rates. For instance, co-operativity allows a protein to fold rapidly within milliseconds, rather than requiring the protein to sample all possible configurations, which would need a time longer than the age of the universe. It is possible that cation exchange reactions in NCs are driven to completion due to the strongly co-operative nature of the transition.

1.5 Conclusion

Akin to co-operativity between molecular units in the biological world, co-operativity between atoms may be ubiquitous in the solid-state, where there is no dearth of multi-site systems. Formation of defects, interfaces, or strain may provide the required inter-site interactions. Co-operative behavior in solid-state systems needs closer attention, especially in relation with closely linked processes such as phase transitions and nucleation[32,33] and due to the utility of such phenomena in predicting and controlling materials' transformation outcomes. Non-linear behavior induced by co-operativity may allow the design of sensors with tight regulation.

1.6 Methods

1.6.1 Model

We simulated the response of NCs using a lattice-site model. Each NC was assumed to have a size of n = 20 sites, each of which can incorporate two Cu^+ ions. Co-operativity was introduced in this model by requiring that binding takes place sequentially: only when a doping event has taken place at the first site does the second binding site become available, and so on...

$$(CdSe)_n + 2.Cu^+ \leftrightharpoons (CdSe)_{n-1}(Cu_2Se) + Cd^{2+}$$

$$M \qquad\qquad ML \qquad\qquad k_1$$

$$(CdSe)_{n-1}(Cu_2Se) + 2.Cu^+ \leftrightharpoons (CdSe)_{n-2}(Cu_2Se)_2 + Cd^{2+}$$

$$ML \qquad\qquad ML_2 \qquad\qquad k_2$$

$$(CdSe)_{n-2}(Cu_2Se)_2 + 2.Cu^+ \leftrightharpoons (CdSe)_{n-3}(Cu_2Se)_3 + Cd^{2+}$$

$$ML_2 \qquad\qquad ML_3 \qquad\qquad k_3$$

$$| \qquad\qquad | \qquad\qquad |$$

$$(CdSe)(Cu_2Se)_{n-1} + 2.Cu^+ \leftrightharpoons (Cu_2Se)_n + Cd^{2+}$$

ML_{n-1} ML_n k_n

Here M, ML, ML_2, … are relative concentrations of NC complexes from CdSe through to Cu_2Se and k_1, k_2, k_3,...are binding association constants for each sequential step.

$$k_1. = \exp^{-\Delta G/kT}$$

We assumed that the first binding constant k_1 has a relatively small magnitude (10^{-2} M^{-1}). However, the first step enhances the binding free energy of the second step by an amount Δg, and the second step enhances that of the third one and so on… Therefore,

$$k_2. = \exp^{-(\Delta G+\Delta g)/kT}$$

$$k_3. = \exp^{-(\Delta G+2\Delta g)/kT}$$

$$| \qquad |$$

$$k_n. = \exp^{-(\Delta G+(n-1)\Delta g)/kT}$$

or,

$$k_2/k_1 = k_3/k_2 = k_4/k_3 = \ldots\ldots k_n/k_{n-1} = a$$

where $a = \exp^{-\Delta g/kT}$. Since Δg is negative, a is a positive integer, which we term as the interaction parameter. The magnitude of a depends directly on the relative value of the binding free energy stabilization relative to the thermal energy. For instance, a 0.1-eV stabilization can result in a ~55, which was a typical value used in the simulations. A higher value of a allows the transition to be achieved over a narrower concentration window for the same value of k_1.

For a free Cu^+ concentration c and Cd^{2+} concentration d, concentrations of the different NC complexes can be given in terms of the concentration of unexchanged CdSe NCs M as:

$$ML = k_1.M.c^2/d$$

$$ML_2 = k_2.ML.c^2/d$$

$$ML_3 = k_3.ML_2.c^2/d$$

$$| \qquad |$$

$$ML_n = k_n.ML_{n-1}.c^2/d$$

In general,

$$ML_i = M/a.(k.a)^i$$

where we define a dimensionless k:

$$k = k_1.c^2/d$$

The fraction of NCs in the pure CdSe state is given by:

$$M/M_T = a/\{a+\sum_{i=1}^{n}(k.a)^i\}$$

where:

$$M_T = M+ML+ML_2+.....ML_n = M\{1+1/a.\sum_{i=1}^{n}(k.a)^i\}$$

The fraction of NCs in the Cu_2Se state is given by:

$$ML_n/M_T = (k.a)^n/\{a+\sum_{i=1}^{n}(k.a)^i\}$$

$1-ML_n/M_T$ gives the fraction of NCs that are either purely CdSe or Cu-doped CdSe. The total concentration of Cu^+ dopants is given by:

$$c_d = 2.\{ML+2.ML_2+.....+(n-1).ML_n\}/M_T = 2.\{\sum_{i=1}^{n-1}(k.a)^i\}/\{a+\sum_{i=1}^{n}(k.a)^i\}$$

Note in the above expression Cu^+ ions in Cu_2Se state are not included since they are no longer in the form of dopants and do not contribute to defect luminescence. Neither are free Cu^+ ions in solution included. c_d is also equal to two times the concentration of Cd^{2+} vacancies. The bound Cu^+ concentration can be given by:

$$c_b = 2.\{\sum_{i=1}^{n}(k.a)^i\}/\{a+\sum_{i=1}^{n}(k.a)^i\}$$

The free Cd^{2+} concentration is given by:

$$d = c_b/2.$$

The free Cu^+ concentration is given by:

$$c_f = \sqrt{c_b.k/2k_1}$$

and the total Cu^+ concentration as:

$$c_t = c_b+c_f$$

1.6.2 Experimental methods

Synthesis of CdSe nanocrystals. The procedure for synthesis of CdSe nanocrystals was adapted from Manna and coworkers.[34] 3.0 g of trioctlyphosphine Oxide (TOPO), 0.280 g of octadecylphosphonic acid (ODPA), and 0.060 g of cadmium oxide (CdO) were mixed in a 25 mL three neck flask, heated to 150°C, and exposed to vacuum for one hour. Under argon the solution was heated to 320°C until optically clear to dissolve CdO. At this point, 1.5 g of tri-n-octylphosphine was injected into the flask. The flask was heated to 370°C and a TOP-Se solution (0.058 g of selenium powder and 0.360g of TOP) was injected into the flask. The reaction time, before the heating source was removed, was modified to obtain CdSe nanocrystals of a particular size. After the synthesis, the nanocrystals were repeatedly precipitated with methanol followed by re-dissolution in toluene. The CdSe NC diameter was calculated from the position of the first exciton.[iii] The NCs used in all the titrations had an excitonic peak at 587 nm corresponding to a diameter of 4.1 nm.

Stoichiometry calculations for cation exchange titrations. For titrations, the initial concentration of Cd^{2+} ions from the CdSe NCs in each reaction cuvette was determined. From the position of the first exciton, λ, the diameter, D, of the NC and the extinction coefficient were calculated using the equations[35]:

$$D = (1.6122 \times 10^{-9})\lambda^4 - (2.6575 \times 10^{-6})\lambda^3 + (1.6242 \times 10^{-3})\lambda^2 - (0.4277)\lambda + (41.57) \quad (1)$$

$$\epsilon = 5857(D)^{2.65} \quad (2)$$

The extinction coefficient ϵ and the absorbance at the first exciton were used to determine the concentration of NCs. From the diameter, the volume and mass of the NCs was calculated, from which the total mass and molar amount of Cd^{2+} ions for each CdSe solution was determined. All titrations were done with approximately equal concentrations of CdSe NCs Each Cu^+ titration involved 4.8 x 10^{-6} mol of Cd^{2+} ions being exchanged with one stoichiometric equivalent of Cu^+ ions (9.6 x 10^{-6} mol of $Cu(I)PF_6$) dissolved in 200 µL of methanol. The details for each incremental addition in the titration is given in the table below. The right-most column was used as the x-axis value for the titration plots shown in Fig. 1.2.

Table 1.2 *Concentration calculations for Cu^+ exchange titrations*

Addition Number	$[Cu^+]$ added (moles)	Total $[Cu^+]$ in cuvette (moles)	Cu^+ ions per nanocrystal
0	0	0	0
1	4.8E-07	4.8E-07	65
2	4.8E-07	9.6E-07	130
3	4.8E-07	1.4E-06	195
4	4.8E-07	1.9E-06	260
5	4.8E-07	2.4E-06	325
6	4.8E-07	2.9E-06	390
7	4.8E-07	3.3E-06	455
8	4.8E-07	3.8E-06	521
9	4.8E-07	4.3E-06	586
10	4.8E-07	4.8E-06	651
11	9.6E-07	5.7E-06	781
12	9.6E-07	6.7E-06	911
13	1.4E-06	8.1E-06	1106
14	1.4E-06	9.6E-06	1301

Cation exchange procedure. All exchange reactions were carried out in septa-capped 3.5 mL quartz cuvettes. In an oxygen and moisture-free glove box, CdSe NCs were dispersed in 3.0 mL of toluene. Initial Cd^{2+} molar amounts were calculated as described above to be 4.8 x 10^{-6} mol Cd^{2+}. In total, 9.6 x 10^{-6} mol of tetrakis(acetonitrile)copper(I) hexafluorophosphate ($Cu(I)PF_6$) in 200 µL of methanol was added during each titration. NC samples were prepared in the glove box in air-free conditions and kept in air-free cuvettes during the exchange reactions. Additions took place outside of the glove box. A sealed solution of $Cu(I)PF_6$ in methanol prepared in the glove box was sequentially added to the reaction cuvette with a microliter syringe taking care that the solution or sample were not exposed to air. Samples were stirred vigorously after each addition and the solution was allowed to equilibrate while stirring for approximately one hour, which is a time much in excess of the typical reaction time for complete cation exchange (<1 sec). Absorption and photoluminscence (PL) spectra were then taken.

Optical spectroscopy measurements. Absorption spectra of exchanged CdSe NCs were collected on a Shimadzu UV-3600 scanning spectrophotometer with a 1-nm step-size in the toluene with toluene as a

reference solvent. PL spectra of NCs were taken in toluene on a Cary Eclipse fluorimeter. Spectra were taken in the 650-900 nm wavelength range, where trap luminescence appears. All PL measurements were performed using the same slit width, scan speeds, excitation energies, and PMT voltages.

Analysis of absorption and photoluminescence spectra. The total volume change over the entire titration was less than 10%, therefore correction of spectra for volumetric dilution was not necessary. The uncorrected absorbance spectra (Fig. 1.6A), shown from 1.55 to 3.0 eV, contain absorption from both unexchanged CdSe NCs and formed Cu_2Se NCs. The absorption contribution of the formed Cu_2Se NCs was subtracted from the uncorrected spectrum to isolate the absorption of only unexchanged CdSe NCs as follows:

$$\text{Corrected spectrum} = \text{Uncorrected spectrum} - \left(\text{Cu}_2\text{Se spectrum x } \frac{\text{Absorbance of Uncorrected spectrum at 1.82 eV}}{\text{Absorbance of Cu}_2\text{Se spectrum at 1.82eV}}\right)$$

Here, we use the fact that at 1.82 eV, the absorption contribution from CdSe is negligible. The absorbance A at the first exciton peak of the corrected spectrum is proportional to the concentration of unexchanged CdSe NCs in solution as per Beer-Lambert's law. This absorbance A normalized to a value of 100% at 0% exchange is equal to the percentage of CdSe NCs that is still unexchanged. This percentage was plotted as a function of Cu^+ added in Fig. 1.2A.

The absorbance of Cu_2Se at 1.82 eV (i.e., above its band-gap absorption onset) can be used to quantify the relative concentration of Cu_2Se NCs produced over the course of the titration. The absorbance at 1.82 eV normalized to a value of 100% at full exchange is equal to the percentage of Cu_2Se NCs formed. This percentage was also plotted as a function of Cu^+ added in Fig. 1.2A.

PL spectra were corrected by removing the contribution from the excitonic PL of CdSe NCs as follows:

$$\text{Corrected Spectrum} = \text{Uncorrected Spectrum} - (\text{Unexchanged CdSe Spectrum} \times \frac{\text{PL intensity of Uncorrected Spectrum at 650nm}}{\text{PL intensity of Unexchanged CdSe at 650nm}})$$

After this correction, the defect PL bands were integrated between 650 and 900 nm. The integrated PL signal was plotted as a function of Cu^+ added in Fig. 1.2A.

Electron microscopy. High resolution transmission electron microscopy (HRTEM) images were taken using a JEOL 2010 LaB_6 operating at 200 kV. High-angle annular dark field scanning electron transmission microscopy (HAADF-STEM) were acquired on a JEOL 2010F at 200 kV with a 0.5 nm size beam. Samples

of NCs were prepared by drop-casting NCs in toluene on an ultrathin carbon grid and repeatedly washing with methanol.

NC morphology. The HAADF-STEM and HRTEM images below display 4-nm NCs as a function of the concentration of copper added in Cu^+ ions per NC. Samples were made from adding $Cu(I)PF_6$ in 200 uL methanol to CdSe NCs in toluene. The NCs were drop-casted from this toluene:methanol mixture onto a Cu grid, followed by washing with methanol to remove excess Cu^+ and Cd^{2+} resulting from exchange. Images show preservation of size and morphology throughout the exchange process. Sizing analysis was done using HAADF-STEM images. Lattice fringes in HRTEM show the NCs maintain crystallinity throughout the exchange process.

Elemental analysis. Inductively-coupled optical emission spectrometry was acquired on a Perkin-Elmer 2000DV ICP-OES. To prepare samples, NCs were repeatedly washed and precipitated with methanol to remove excess ions in solution. ~1 mg of each sample was digested with 16 M HNO_3 and subject to ICP-MS analysis for determination of the molar ratios of Cd, Cu, and Se.

Exchange with Ag^+. All titration experiments were performed in an identical manner with Ag^+ as the extrinsic ion. Initial Cd^{2+} molar amounts were calculated as described above to be 4.4×10^{-6} mol of Cd^{2+} in each cuvette. In total, 8.9×10^{-6} mol of silver nitrate ($AgNO_3$), corresponding to 1 stoichiometric equivalent was the calculated amount to be added over the titration Slightly more was actually found to be needed (1.1×10^{-5} mol of $AgNO_3$ in 240 µL of methanol) to ensure complete disappearance of the first exciton peak of CdSe.

Absorption and PL spectra were corrected and processed using the same methods described earlier. Uncorrected absorption spectra (Fig. 1.10A) were baseline corrected (Fig. 1.10B) to account for absorption of Ag_2Se NCs. The CdSe exciton peak heights were then analyzed to estimate the percentage of NCs exchanged as a function of Ag^+ added (Fig. 1.5). The PL spectra (Fig. 1.10C) were corrected (Fig. 1.10D) to account for the band-edge PL. Following correction, the defect PL band was integrated to show the trend in defect PL intensity as a function of Ag^+ added (Fig. 1.5).

X-ray photoelectron spectroscopy (XPS). XPS analysis was performed on NCs exchanged with 0%, 25%, and 50% stoichiometric equivalent of Cu^+. A Kratos Axis ULTRA instrument was used, which uses a monochromatized Al Kα X-ray source of 15 kV (~10 mA). The instrument consisted of separate specimen transfer and analysis chambers, typically operated at 5E-07 Torr and 1E-09 Torr, respectively. Fig. 1.4B shows copper XPS peaks (Cu $2p_{3/2}$ and Cu LMM). Cu $2p_{3/2}$ spectrum was fitted with 30% Gaussian/70% Lorentzian peak shapes. C 1S peak position was used as a reference. The samples subject to 25% and 50% Cu^+ (Fig. 1.4 and Fig. 1.11C) show a Cu $2p_{3/2}$ with a fitted peak position of 932.5eV, which suggests a Cu^{1+}

oxidation state. To distinguish between Cu^0 and Cu^{1+}, high resolution spectra were collected around the X-ray induced Cu LMM Auger peak (shown in Fig. 1.4C). The peak position of 917.2eV (K.E.) corresponds to Cu^{1+}. The absence of the Cu^{1+} peak in the Cu $2p_{3/2}$ (Fig. 1.11A) and Cu LMM (Fig. 1.11B) spectra in the unexchanged sample shows that there is no copper in the original CdSe NCs.

1.7 Additional figures

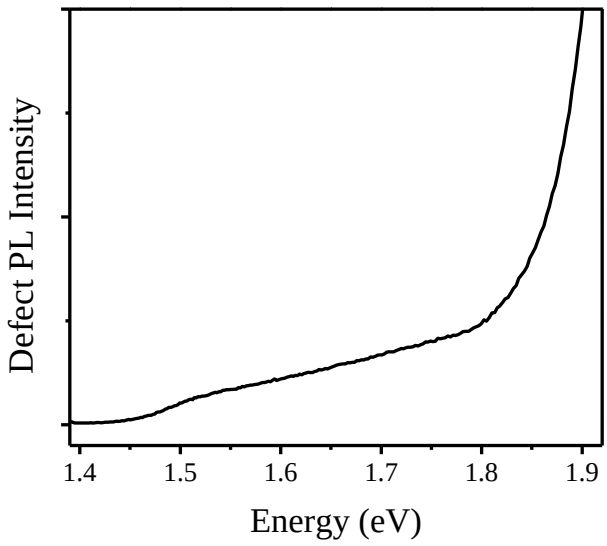

Figure 1.6 *In a control experiment, 200 µL of methanol was added to a solution of CdSe NCs. PL spectrum taken after 70 min showed that no trap PL emerged as a result of methanol addition over the timescale of each data-point in our titrations.*

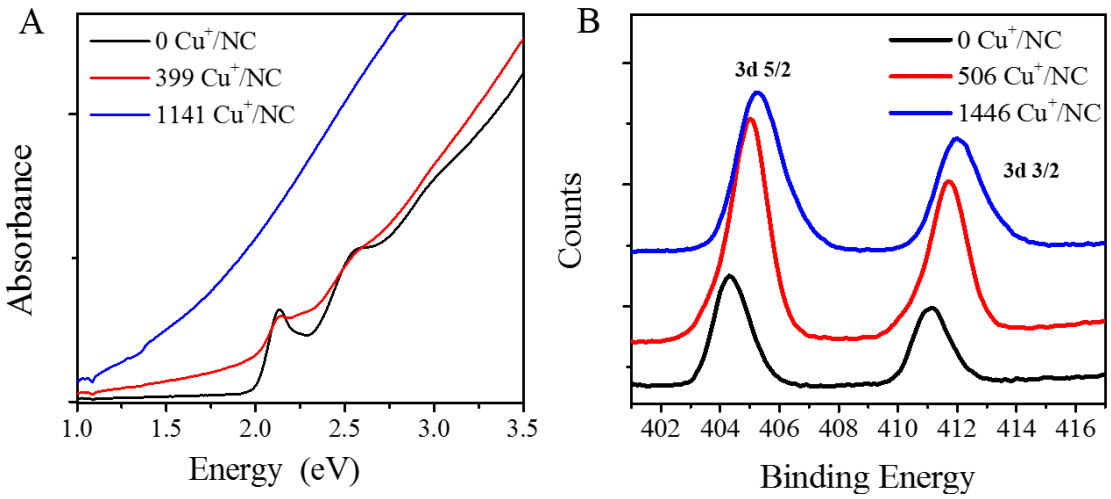

C

Cu^+ Ions/NC	Cd:Se Ratio	Cu:Se Ratio	Se:Se Ratio
0	0.99	0.00	1
399	0.69	0.68	1
1141	0.28	1.86	1

Figure 1.7 ICP-OES elemental analysis and X-ray photoelectron spectroscopy. *The actual amount of copper incorporated in the NCs was detected at three points along the conversion from CdSe to Cu_2Se using ICP-OES. (C) The starting NCs show a Cd to Se ratio of 1:1. With 399 Cu^+ ions/NC added, nearly all the available Cu^+ ions appears to be incorporated within the nanocrystals, with a proportional decrease in the number of Cd^{2+} ions. When the concentration reaches 1141 Cu^+/NC, the NCs are predominantly copper selenide with an average stoichiometry of $Cu_{1.86}Se$, with some residual Cd, possibly in the form of dopants in the nanocrystals or leftover cadmium oxide or hydroxide. Formation of cadmium oxide or hydroxide has been suggested in literature[iv] to increase the Cd 3d binding energy by ca. 1 eV, which we observed in our XPS. Absorption spectra signifying the degree of conversion for each of the samples are shown. (A) XPS with Cd 3d3/2 and 3d5/2 peaks are shown for CdSe NCs treated with different amounts of Cu^+ ions in methanol solution. (B) All XPS spectra were calibrated relative to the C 1s/7 peak.*

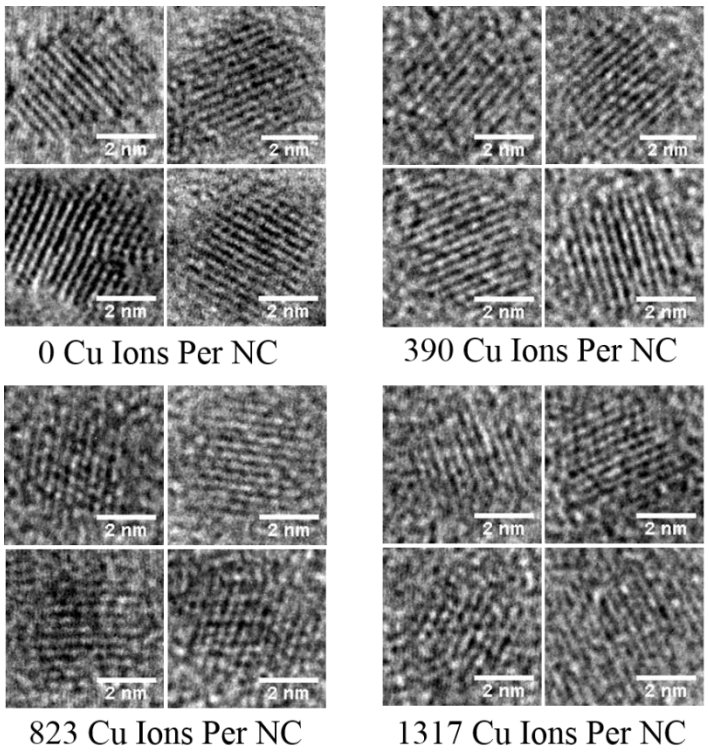

Figure 1.8 High resolution transmission electron microscopy (HRTEM) *verifies crystalline nature of nanocrystals throughout the cation exchange process. High resolution images were taken using a JEOL 2010 LaB_6 operating at 200 kV. Four representative images each are shown at various stages of the conversion from CdSe to Cu_2Se. At all stages of the conversion, images show lattice fringes with a spacing of 0.35 nm (in a majority of cases, although a few nanocrystals were identified with other lattice orientations at all stages of the conversion). This lattice spacing matched the longest lattice spacing measured in electron diffraction patterns (shown in the main text) for all samples from CdSe through Cu_2Se. Since the lattice spacing for the unexchanged CdSe and the Cu_2Se nanocrystals are similar, HRTEM cannot be used to characterize the state of exchange for individual nanocrystals. Samples were prepared by a slow titration of CdSe nanocrystals in toluene with increasing amounts of a methanolic solution of Cu^+, similar to the titration experiments described in the main text figures. At various points in the titration, a small aliquot was drop-casted onto an ultrathin carbon TEM grid and washed with methanol several times. The total amount of Cu^+ added is indicated below each image in the form of number of ions per nanocrystal, estimated as described earlier in Section 1.6.2.*

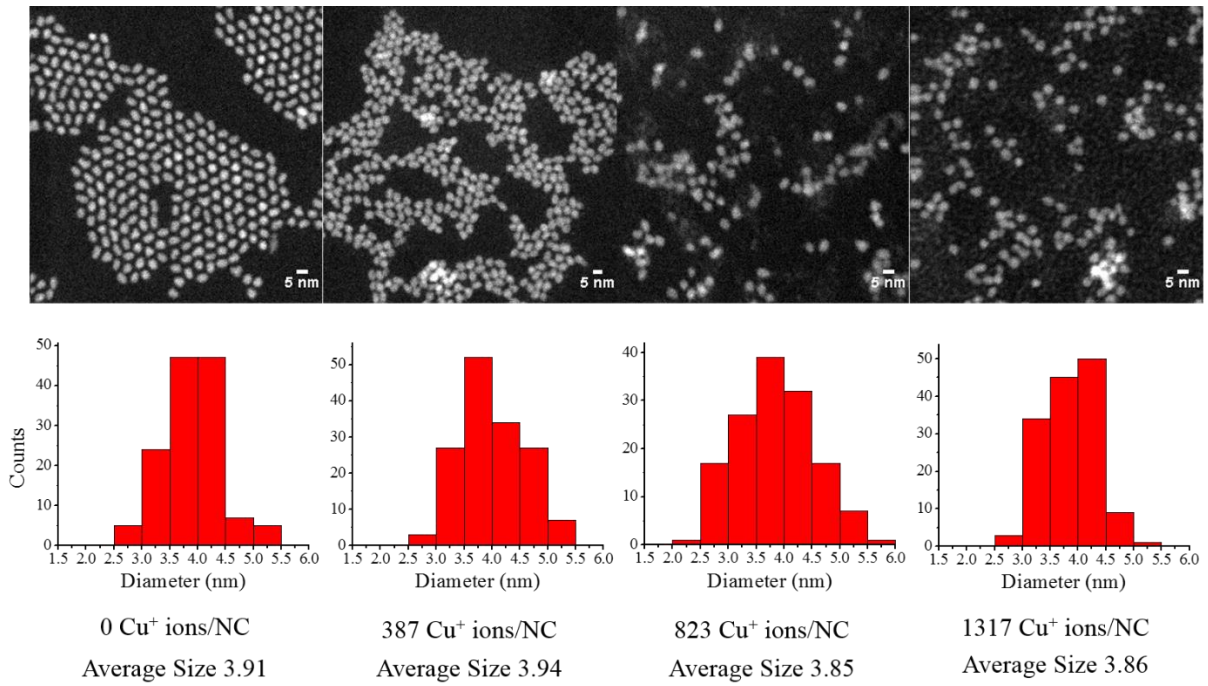

Figure 1.9 High-angle annular dark field scanning electron transmission microscopy (HAADF-STEM) *displays size and shape retention throughout cation exchange. Top panel shows representative HAADF-STEM images for nanocrystals at various stages of conversion from CdSe to Cu_2Se. Nanocrystal sizes were estimated manually in Image J by measuring the diameter of the nanocrystal using the line tool from several representative images. Data from at ca. 200 nanocrystals was used to make the size histograms shown in the bottom panel. Average diameters were determined by Gaussian fitting of the histograms. At all stages, the nanocrystals are 3.9 nm in size and spherical in shape. Samples were prepared by a slow titration of CdSe nanocrystals in toluene with increasing amounts of a methanolic solution of Cu^+, similar to the titration experiments described in the main text figures. At various points in the titration, a small aliquot was drop-casted onto an ultrathin carbon TEM grid and washed with methanol several times. The total amount of Cu^+ added is indicated below each image in the form of number of ions per nanocrystal, estimated as described earlier in Section 1.6.2. HAADF-STEM were acquired on a JEOL 2010F at 200 kV with a 0.5 nm size beam.*

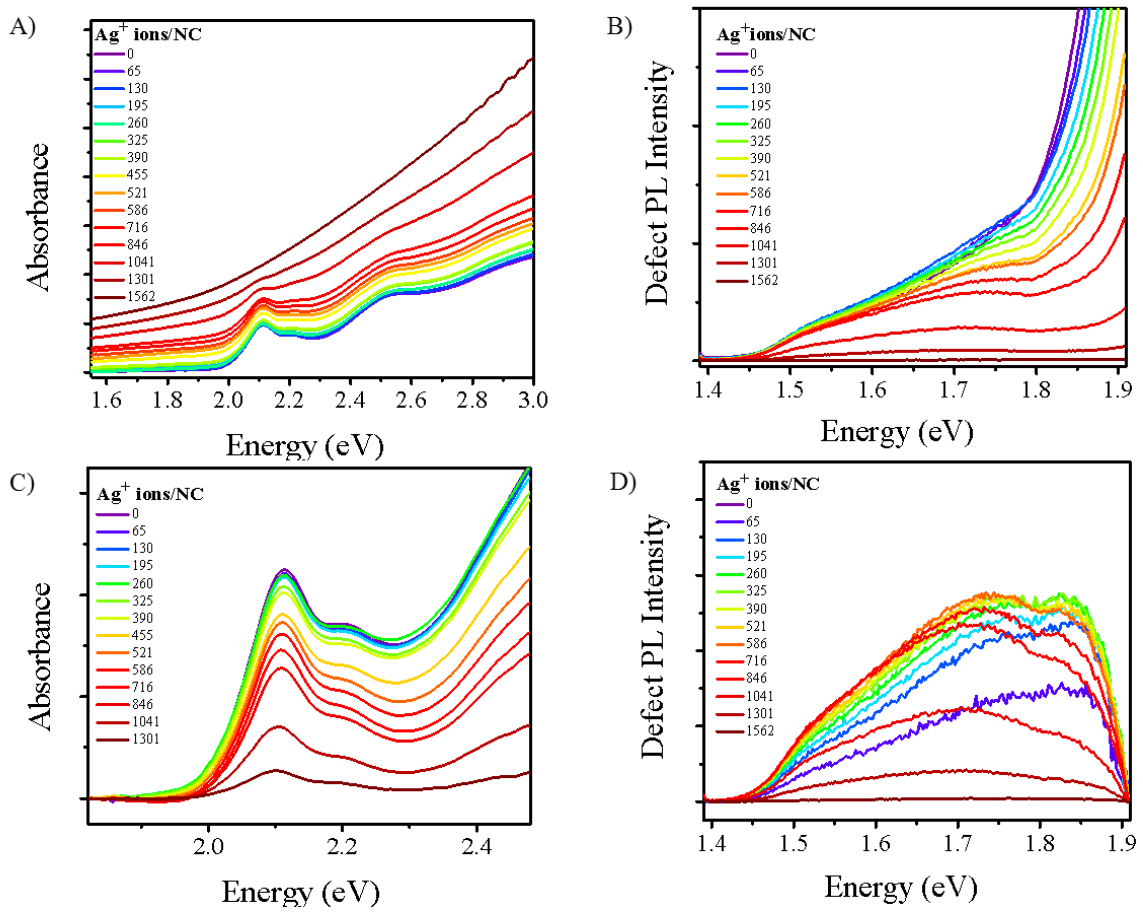

Figure 1.10 *The absorption spectra for CdSe exchanged with Ag $^{+}$are presented in uncorrected (A) and baseline corrected (C) form. The defect PL spectra are presented in uncorrected (B) and baseline corrected (D) form. The method used for baseline correction was identical to that used for titrations with Cu^{+} ions. The cleft feature at 1.79 eV in the corrected (D) and uncorrected (B) PL spectra is an instrumental artifact.*

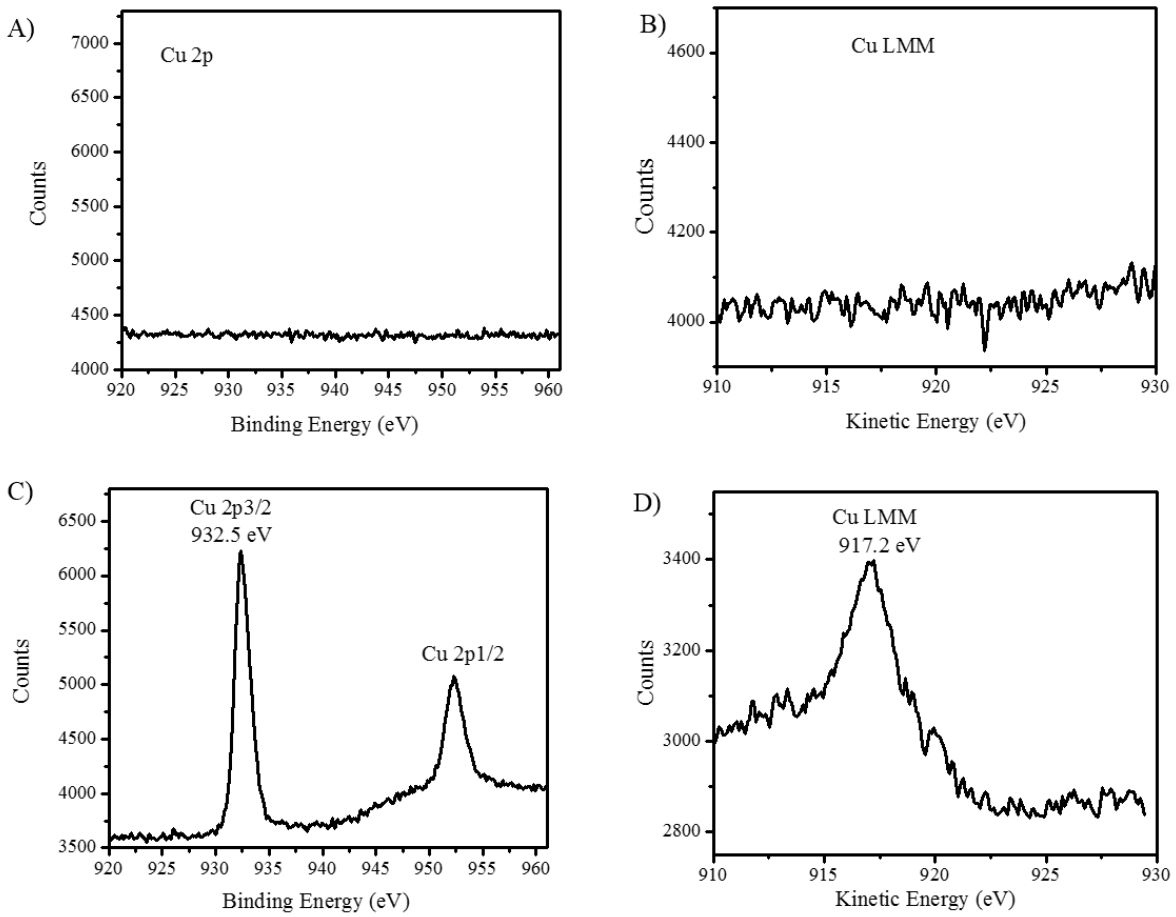

Figure 1.11 High-resolution XPS spectra. *Cu 2p and Cu LMM spectra for CdSe treated with 50% stoichiometric equivalent of Cu^{+} are shown in (A) and (B) respectively and for unexchanged in (C) and (D) respectively.*

1.8 References

1. Hill, A. V. The possible effects of the aggregation of the molecule of hemoglobin on its dissociation curves. *J. Physiol.* **40,** iv–vii (1910).

2. Ackers, G. K., Doyle, M. L., Myers, D. & Daugherty, M. A. Molecular code for cooperativity in hemoglobin. *Science* **255,** 54–63 (1992).

3. Whitty, A. Cooperativity and biological complexity. *Nat. Chem. Biol.* **4,** 435–9 (2008).

4. Shank, E. a, Cecconi, C., Dill, J. W., Marqusee, S. & Bustamante, C. The folding cooperativity of a protein is controlled by its chain topology. *Nature* **465,** 637–40 (2010).

5. Prince, R. B., Saven, J. G., Wolynes, P. G. & Moore, J. S. Cooperative conformational transitions in phenylene ethynylene oligomers: Chain-length dependence. *J. Am. Chem. Soc.* **121,** 3114–3121 (1999).

6. Hunter, C. A. & Anderson, H. L. What is cooperativity? *Angew. Chemie - Int. Ed.* **48,** 7488–7499 (2009).

7. Dukes, A. D., McBride, J. R. & Rosenthal, S. J. Synthesis of magic-sized CdSe and CdTe nanocrystals with diisooctylphosphinic acid. *Chem. Mater.* **22,** 6402–6408 (2010).

8. Son, D. H. *et al.* Cation Exchange Reactions in Ionic Nanocrystals. *Science (80-.).* **306,** 1009–1012 (2004).

9. Robinson, R. D. *et al.* Spontaneous Superlattice Partial Cation Exchange. **317,** 355–358 (2007).

10. Pollok, K., Putnis, C. V. & Putnis, A. Mineral replacement reactions in solid solution-aqueous solution systems: Volume changes, reactions paths and end-points using the example of model salt systems. *Am. J. Sci.* **311,** 211–236 (2011).

11. Chan, E. M. *et al.* Millisecond kinetics of nanocrystal cation exchange using microfluidic X-ray absorption spectroscopy. *J. Phys. Chem. A* **111,** 12210–12215 (2007).

12. Miszta, K. *et al.* Hierarchical self-assembly of suspended branched colloidal nanocrystals into superlattice structures. *Nat. Mater.* **10,** 872–876 (2011).

13. Kovalenko, M. V. *et al.* Quasi-seeded growth of ligand-tailored PbSe nanocrystals through cation-exchange-mediated nucleation. *Angew. Chemie - Int. Ed.* **47,** 3029–3033 (2008).

14. Jain, P. K., Amirav, L., Aloni, S. & Alivisatos, A. P. Nanoheterostructure cation exchange: Anionic framework conservation. *J. Am. Chem. Soc.* **132,** 9997–9999 (2010).

15. Li, J., Zhang, T., Ge, J., Yin, Y. & Zhong, W. Fluorescence signal amplification by cation exchange in ionic nanocrystals. *Angew. Chemie - Int. Ed.* **48,** 1588–1591 (2009).

16. Sahu, A. *et al.* Electronic impurity doping in CdSe nanocrystals. *Nano Lett.* **12,** 2587–2594 (2012).

17. Mocatta, D. *et al.* Heavily doped semiconductor nanocrystal quantum dots. *Science* **332,** 77–81 (2011).

18. Norris, D. J., Sacra, A., Murray, C. B. & Bawendi, M. G. Measurement of the size dependent hole spectrum in CdSe quantum dots. *Phys. Rev. Lett.* **72,** 2612–2615 (1994).

19. Varvas, J. A. Defect Structure of Cu-Doped Cadmium Selenide. **467,** 0–6 (1982).

20. Grandhi, G. K., Tomar, R. & Viswanatha, R. Study of surface and bulk electronic structure of II-

VI semiconductor nanocrystals using Cu as a nanosensor. *ACS Nano* **6,** 9751–9763 (2012).

21. Meulenberg, R. W. *et al.* Structure and composition of Cu-doped CdSe nanocrystals using soft X-ray absorption spectroscopy. *Nano Lett.* **4,** 2277–2285 (2004).

22. Sakalas, A. Scattering Centres and Their Relation to the Recombination Centres in Single Crystals of CdSe. **301,** 301–307 (1975).

23. Ture, I. E., Claybourn, A., Brinkman, A. W. Defects in Cadmium Selenide,. **72,** 189–193 (1985).

24. Kokubun, Y., Watanabe, H., Wada, M. Photoluminescence of CdSe Single Crystals. *J. App. Phys.* **13,** 1393-1398 (1974).

25. Monod, J., Wyman, J. & Changeux, J. P. on the Nature of Allosteric Transitions: a Plausible Model. *J. Mol. Biol.* **12,** 88–118 (1965).

26. Weiss, J. N. The Hill equation revisited: uses and misuses. *FASEB J.* **11,** 835–841 (1997).

27. Hainovsky, N. & Maier, J. Premelting, sublattice melting, and overall melting in Frenkel disordered ionic crystals. *Solid State Ionics* **76,** 199–205 (1995).

28. Fayet, P. *et al.* The role of small silver clusters in photography. *Zeitschrift f??r Phys. D Atoms, Mol. Clust.* **3,** 299–302 (1986).

29. R. W. Gurney & Mott, N. F. The Theory of the Photolysis of Silver Bromide and the Photographic Latent Image. doi:10.1098/rspa.1983.0054

30. Thompson, A. B. & Woods, D. W. The Photographic Process. *Nature* **175,** 642–643 (1955).

31. Rivest, J. B. & Jain, P. K. Cation exchange on the nanoscale: an emerging technique for new material synthesis, device fabrication, and chemical sensing. *Chem. Soc. Rev.* 89–96 (2013). doi:10.1039/c2cs35241a

32. Baumgartner, J. *et al.* Nucleation and growth of magnetite from solution. *Nat. Mater.* **12,** 310–4 (2013).

33. Chase, J. M. Stable Prenucleation Calcium Carbonate Clusters. **19,** (2009).

34. Carbone, L. *et al.* Synthesis and micrometer-scale assembly of colloidal CdSe / CdS nanorods prepared by a seeded growth approach. *Nano Lett.* **7,** 2942–2950 (2007).

35. Yu, W. W., Qu, L., Guo, W. & Peng, X. Experimental determination of the extinction coefficient of CdTe, CdSe, and CdS nanocrystals. *Chem. Mater.* **15,** 2854–2860 (2003).

Chapter 2: Atomistic insights into the intermediate state of cation exchange obtained from ultrasmall clusters*

2.1 Abstract

The optical attributes of ultrasmall semiconductor clusters are sensitive probes for chemical or electronic changes occurring either on the surface or within the core of the cluster. We leverage the high sensitivity of excitonic absorption of ultrasmall cadmium selenide clusters to changes in doping density and surface chemistry to investigate the mechanism of a solid-state transformation: cation exchange. This increased sensitivity has allowed us to identify a stable, long-lived intermediate in the cation exchange transformation. Isolation and characterization of this intermediate provides atomistic insight into the structure of the cationic sub-lattice during cation exchange. Through a change in the ligand shell, we find the occurrence of this intermediate depends on the electronic stabilization of surface Cd ions by ligand passivation. A better understanding of how ligand passivation affects ion exchange at the solid-liquid interface could help engineer improved materials for solid-state electrolytes and energy storage devices.

2.2 Introduction

Thermodynamically stable, ultrasmall clusters are an exciting class of materials because they are structurally and electronically homogeneous materials with a composition more akin to molecules than extended solids.[1,2] As a result, ensemble properties of ultrasmall clusters can be studied without having to consider broadening from a heterogeneous distribution of particle sizes and surface morphologies, as is typically the case with larger nanoparticles. For example, thermodynamically-stable "magic-size" cadmium selenide (CdSe) clusters exhibit a very narrow size-dependent excitonic absorption energy indicative of a homogeneous size distribution.[1,3] Since particle-to-particle heterogeneity can have an impact on the reactivity of a nanoparticle ensemble, structurally and electronically homogeneous ultrasmall clusters offer an attractive alternative for studying reactions and phase transformations in solids. In additional to being homogeneous, ultrasmall clusters often have optical and electronic properties that are more sensitive to changes occurring at the surface such as ligand binding, because a significant percentage of atoms in each cluster are at the surface, and to single atomic-scale events like electron or ion transfer, because a

* Reproduced with permission from: White, S. L., Jain, P. K., Atomistic insights into the intermediate stage of cation exchange obtained from ultrasmall clusters, *In preparation*.

single electron or ion transfer can have a significant effect on the density of charge carriers in each ultrasmall cluster.[4–6]

Recent studies have shown that cation exchange, a topotactic transformation that occurs in ionic solids in which the native cations of an ionic solid are place-exchanged for cations of another type while the anionic framework is preserved, is a rapid reaction that is preceded by doping of the initial ionic lattice with positively charged impurity cations and the subsequent creation of negatively charged cationic vacancies.[7,8] In this study, we investigate cation exchange of CdSe magic-size clusters with Cu^+ ions in solution to form copper (I) selenide (Cu_2Se) clusters. We leverage the high sensitivity of the excitonic absorption energy of CdSe clusters to changes in surface chemistry and defect density to identify a distinctive, long-lived intermediate formed during the cation exchange transformation. Through isolation and characterization of this unexpectedly stable intermediate, we develop insight into the structure of the native Cd^{2+} ions and dopant Cu^+ ions that make up the cationic framework in the early stages of cation exchange. We also leverage the high surface-to-volume ratio of CdSe clusters to investigate the role of ligand chemistry on the formation of this Cu-doped intermediate. We find that, in the presence of certain surface ligands, this intermediate is stabilized and a large intermediate population is formed during exchange, while in the presence of other surface ligands, no long-lived intermediate is formed. This work demonstrates the use of ultrasmall clusters as model systems for developing atomistic-level understanding of the chemical reactivity of nanoparticles, in particular, the influence of a high fraction of uncoordinated surface atoms and of the ligand interface.

2.3 Results and discussion

2.3.1 Optical spectroscopy reveals a long-lived, stable intermediate in cation exchange

We used excitonic absorption spectroscopy to monitor cation exchange in an ensemble of magic-size CdSe clusters as a solution of Cu^+ ions in a methanolic solution was added. (Fig. 2.1A & 2.1B) As Cu^+ is added to a solution of CdSe clusters, the excitonic absorption band at 406 nm corresponding to the $1S_h - 1S_e$ excitonic transition decreases and is eventually replaced with a broad band-edge absorption starting in the near-infrared (NIR) region from the formation of Cu_2Se clusters. Before the increase in Cu_2Se cluster absorption, the narrow excitonic absorption peak at 406 nm decreases and is replaced by an equally narrow intermediate excitonic absorption peak at 425 nm, which is then gradually replaced by the NIR band-edge associated with Cu_2Se as more Cu^+ is added to the system. There is a clear isosbestic point between the absorption spectra of the initial CdSe clusters (excitonic peak at 406 nm), the optically-distinct population occurring at an intermediate point in the titration (excitonic peak at 425 nm), and the final Cu_2Se clusters.

In fact, when both the 406 nm and 425 nm peaks are present, two distinct peaks are seen (green spectrum, Fig. 2.1B) suggesting the initial homogeneous population of CdSe clusters forms an equally homogeneous population of intermediate clusters rather than a broad distribution of heterogeneous intermediates. High-resolution transmission electron microscopy images (HR-TEM) and high-angle annular dark-field scanning transmission electron microscopy images (HAADF-STEM) of the initial CdSe clusters and exchanged Cu_2Se clusters show that the size and crystallinity of the clusters are preserved during cation exchange. (Fig. 2.7)

Present in a large excess during synthesis, trioctylphosphine (TOP) is the predominant ligand on the surface of the CdSe clusters after synthesis.[9] Although tertiary phosphines like TOP bind both Cd and Se surface atoms, they more strongly bind Se and are known to stabilize surface Se dangling bonds.[10] (We note that recent publications have proposed that secondary phosphines such as dioctylphosphine and diphenylphosphine, present as impurities in TOP, could also play a role when TOP is present in a high concentration during synthesis.[11]) Tertiary phosphines like TOP, due to both electronic structure and significant steric hindrance from bulky chains, are among the weakest binding ligands for Cd resulting in low ligand coverages and a high percentage of uncoordinated surface Cd atoms compared to surfaces capped with less bulky, more strongly binding ligands including primary amines or carboxylates.[12]

The unfavorability of tertiary phosphines as ligands for CdSe, which is typically thought to have a Cd-rich surface, prompted us to try ligand-exchanging TOP for a ligand that more strongly binds Cd and results in higher ligand coverage. Primary amines, which strongly bind surface Cd, easily displace phosphines from Cd surface atoms of CdSe.[13,14] We performed a ligand exchange on the TOP-capped CdSe clusters with the primary amine, octylamine (OA). Upon addition of an excess of OA followed by purification, the excitonic $1S_h - 1S_e$ peak shifted from 406 nm to 416 nm, which matches observed excitonic energies for OA-capped CdSe clusters.[5] (Fig. 2.1D)

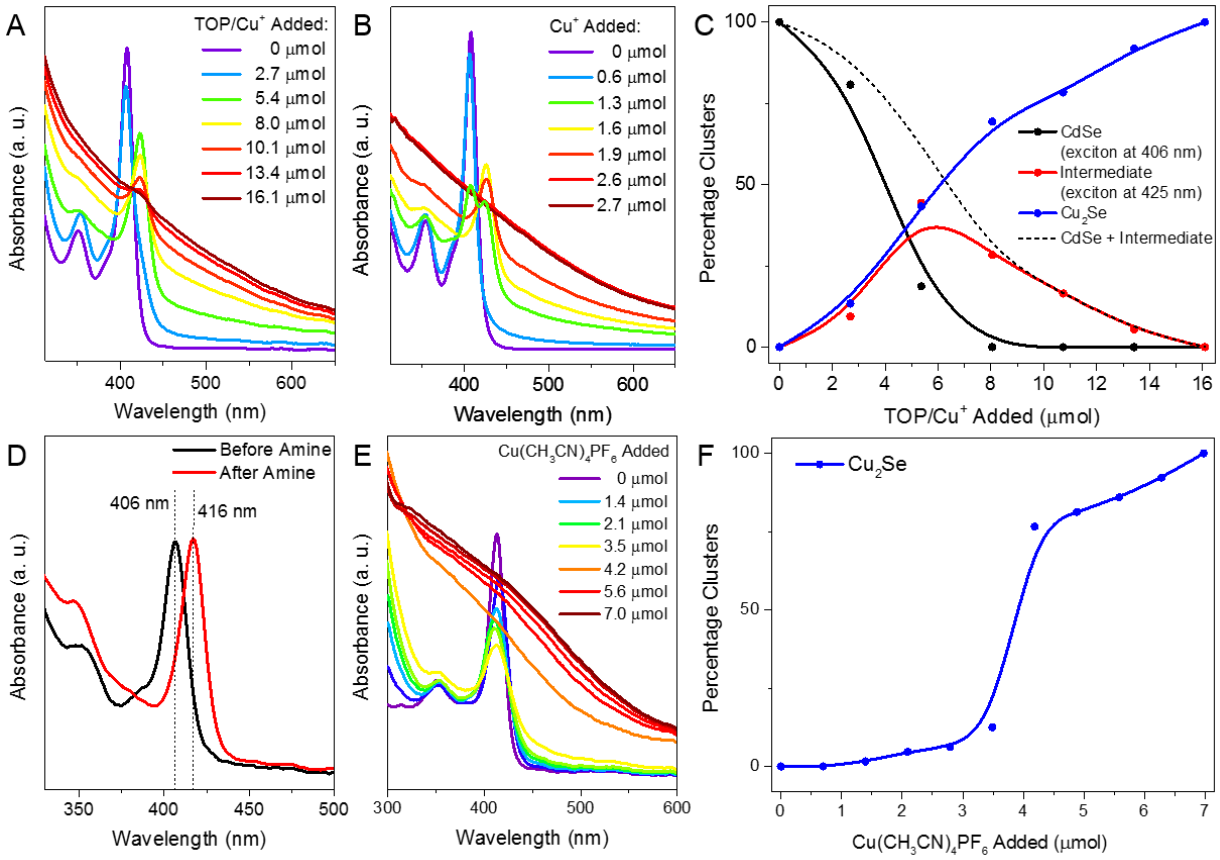

Figure 2.1 Excitonic absorption spectra of an ensemble of CdSe clusters as a function of Cu^+ added, in the form of TOP/Cu^+ (A) or Cu^+ without added TOP (B). *Initially at a wavelength of 406 nm, at a particular concentration of Cu^+, the narrow excitonic peak at 406 nm is replaced by a peak at 425 nm with a clear isosbestic point. After this, the excitonic peak decreases as the concentration of Cu^+ in solution increases. In (C), which corresponds to the spectral data from (A), a plot of the percentage of clusters in the initial CdSe state (exciton at 406 nm) is shown in black points connected with a spline, the percentage of clusters in the intermediate state (exciton at 425 nm) is shown in red points connected with a spline, and the percentage of clusters in the Cu_2Se state is shown in blue points connected with a spline as a function of Cu^+ ions added. The percentage of clusters in either the initial (exciton at 406 nm) or intermediate (exciton at 425 nm) states is shown in a black dotted line. After ligand exchange with OA, the excitonic absorption spectra of CdSe clusters shifts from 407 nm (black line) to 416 nm (red line), shown in (D). The excitonic absorption spectra of TOP-free, OA-capped CdSe clusters as a function of Cu^+ added is shown in (E). As the concentration of Cu^+ increases, the CdSe exciton decreases without shifting. A plot of the fraction of clusters in the Cu_2Se state (blue line) as a function of Cu^+ ions added is shown in (F). The initial concentration of CdSe clusters and hence µmol of Cu^+ ions added vary from titration to titration, but this variation was not found to affect intermediate formation.*

Cation exchange with Cu^+ ions in solution was then carried out with OA-capped CdSe clusters. (Fig. 2.1E) Surprisingly, there was no formation of an intermediate during cation exchange. As Cu^+ is added to a solution of CdSe clusters, the excitonic band, now at 416 nm after ligand exchange, is replaced with the

Cu_2Se band-edge absorption without the formation of a long-lived intermediate. When surface TOP ligands are replaced with OA ligands, a long-lived intermediate is not formed. To confirm the formation of an intermediate is dependent on TOP ligands at the cluster surface, we performed a control in which OA-capped clusters were exchanged with Cu^+ in the form of TOP/Cu^+, but no intermediate formation was observed in this case either. (Fig. 2.5 and 2.6) The intermediate is dependent on the presence of surface tertiary phosphines and/or the absence of surface primary amines. The optical behavior of both TOP-capped and OA-capped CdSe clusters during cation exchange raises two questions: (1) what is the structure of the distinct intermediate formed during exchange with TOP-capped ligands, and (2) how does the presence of surface-bound TOP stabilize the intermediate? Since we can use optical data to isolate a population of intermediate, we can perform further characterization on this intermediate to better understand how it is chemically and structurally unique from both the initial CdSe and final Cu_2Se.

We performed x-ray photoelectron spectroscopy (XPS) on an ensemble of clusters at three points during the cation exchange titration: the initial point when there are only CdSe clusters, the final point when there are only exchanged Cu_2Se clusters, and at a point when there is a high concentration of the intermediate clusters. In Fig. 2.2A and 2.2B there is a clear shift of both the Se 3d and Cd 3d peaks to higher binding energy at each point in the cation exchange transformation. This shift suggests a change in chemical environment for each atom: likely Cd^{2+} leaves the lattice and diffuses into solution and Se^{2-} binds with the more electronegative Cu^+ ions. Integration of the Cd 3d and Se 3d XPS peaks reveals that the initial clusters have an approximately 2:1 Cd:Se ratio, suggesting a metal-rich surface common to ionic nanocrystals, that is generally consistent throughout the exchange resulting in a nearly 4:1 Cu:Se ratio in fully exchanged Cu_2Se. After exchange, the absence of the Cd 3d peaks confirms the lack of Cd in the final Cu_2Se clusters. The presence of Cu 2p peaks in the intermediate indicates that the intermediate contains Cu^+ ions. This is consistent with studies claiming that doping of a CdSe nanocrystals with Cu^+ impurities precedes cation exchange. A red-shifted excitonic absorption peak, as seen in the intermediate clusters, has also been associated with Cu doping in CdSe nanocrystals.[15]

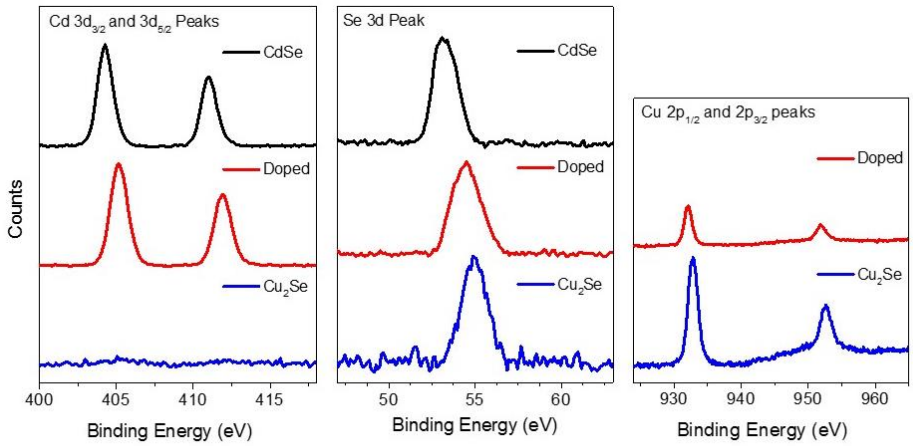

Figure 2.2 High resolution XPS of clusters at the same three stages of cation exchange. *The relative intensities of Cd 3d and Cu 2p peaks in each sample was determined by normalizing the Se 3d peak between all samples. Binding energies of fitted peaks and determined atomic percentages of Cd, Cu, and Se are included in Table 1.*

Table 2.1 *XPS binding energies and atomic percentages for spectra shown in Fig. 2.2.*

Table 2.1 XPS Binding Energies and Atomic Percentages

Sample	Binding Energy Se $3d_{3/2}$ & $3d_{5/2}$	Binding Energy Cd $3d_{5/2}$	Binding Energy Cu $2p_{3/2}$	Atomic % Cd:Se	Atomic % Cu:Se
CdSe	53.3 eV	404.3 eV	--	1.90	--
Intermediate	54.5 eV	405.2 eV	932.1 eV	2.10	1.10
Cu_2Se	55.0 eV	--	932.8 eV	--	3.73

2.3.2 XRD reveals structural intermediate

To yield insights into how the structure of ultrasmall CdSe clusters is changing during cation exchange, powder X-ray diffraction (PXRD) patterns were also collected at three points during the cation exchange titration: the initial point when there are only CdSe clusters, the final point when there are only exchanged Cu_2Se clusters, and at a point when there is a high concentration of the intermediate clusters. (Fig. 2.3) PXRD, although widely used to determined crystal structure in semiconductor nanomaterials, becomes limited in predicting structure at small crystallite size due to Scherrer broadening and surface reconstruction in small nanomaterials. However, in cation exchange, the general structure of the anion framework is preserved and, although PXRD cannot be used to deduce the exact structure of ultrasmall clusters, it can

provide information on how the cationic sub-lattice is changing during this topotactic transformation. We compared experimental XRD patterns with several calculated XRD patterns based on a zincblende face-centered cubic (*fcc*) anionic framework. The *fcc* anionic framework was maintained during exchange (except for a slight contraction of the cubic lattice constant upon conversion to Cu_2Se) but the cationic lattice positions and occupancies were varied to generate a wide range of patterns that were compared to the experimental patterns. Based on this, we proposed a series of structural changes occurring to the cationic framework during cation exchange. The lattice parameters used for all calculated XRD patterns are shown in Table 2. We assign the initial CdSe clusters to a strained cubic structure, similar to the bulk zincblende phase of CdSe. (Fig. 2.3A, black pattern) It matches well a calculated PXRD pattern of a zincblende structure with a slightly compressed lattice constant that incorporates Scherrer broadening of the XRD peaks based on a 2 nm crystallite size (Fig. 2.3B, black pattern). When the intermediate is formed during cation exchange, there are two striking changes that occur in the PXRD pattern. First, there is a significant shift of the lowest 2θ value peak which can either be explained by a significant contraction in the unit cell, or a suppression of the {111} peak and an increase in the scattering factor of the {200} peak. Because the position of other peaks, namely the {400} peak at $2\theta = 60^{o}$, do not appear to shift, it is more likely that the latter is the cause. This change can be explained by a shift of the Cd cations from tetrahedral positions to octahedral position, similar to the rock salt phase of CdSe. The rock salt phase of CdSe is typically only stable at high pressure due to high Cd-Cd repulsion energy. In this case, a decrease in the Cd-Cd repulsion energy due to high Cd vacancy density could lead to a stabilization of Cd atoms in octahedral positions. Second, there is a significant suppression of the {220} peak, which returns after exchange to Cu_2Se, suggesting that it is a unique signature of the intermediate. This trend is observed in the calculated XRD pattern when there is some occupancy of the interstitial *24f* Wyckoff positions in the unit cell. Suppression of the {220} is not observed when Cu atoms are placed in other common positions such as tetrahedral or octahedral positions. (Fig. 2.11)

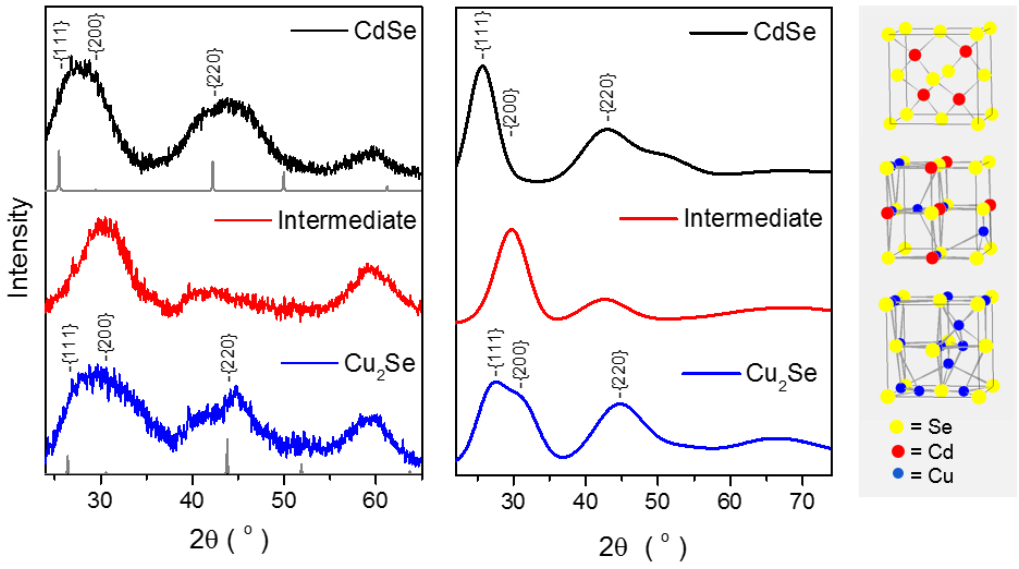

Figure 2.3 Experimental and calculated XRD patterns of CdSe, Cu_2Se and intermediate clusters. *Experimental PXRD patterns of clusters at three stages of cation exchange: initial CdSe clusters (CdSe exciton at 406 nm), intermediate (CdSe exciton at 423 nm), and final Cu_2Se clusters (no CdSe exciton), are shown (left). On the right, calculated XRD patterns of Scherrer-broadened initial zincblende CdSe, Cu doped, and final Cu_2Se structures are shown with representative lattice structures.*

Structural and chemical analysis of the intermediate suggest that a Cu-doped CdSe cluster, in which Cu atoms occupy interstitial positions, forms a metastable intermediate during cation exchange of TOP-capped clusters. For OA-capped clusters, this intermediate is not seen, suggesting it is too short-lived. The latter suggests that the presence of TOP on the surface of CdSe clusters undergoing cation exchange leads to the stabilization of an intermediate structure that is unstable when TOP is not present.

As shown in Chapter 1, cation exchange proceeds through the doping of the initial CdSe clusters with Cu^+ ions, triggering the removal of Cd^{2+} ions such that charge neutrality is preserved. Thus, cation exchange is potentially limited by the ability to create a Cd vacancy at the surface. Justo et al. have also found that the presence of cationic surface vacancies are vital to cation exchange.[16] Since surface atoms are typically stabilized through coordination with ligands, it is important to consider the effect of ligand binding on the energetics of vacancy formation.[17–19]As mentioned earlier, tertiary phosphines are sterically bulky ligands that bind only weakly to surface Cd atoms. Stronger binding affinities for surface Se atoms suggest that on Se-rich ({111} or {100}) or stoichiometric ({110}) CdSe surfaces, TOP preferentially binds only Se atoms leaving Cd atoms unpassivated. As a result, in the presence of TOP bound to Se atoms, the creation of a Cd vacancy on the surface of the NC is likely to result in energy stabilization. As a result, the intermediate structure is likely to be metastable. By contrast, OA-capped clusters have well-passivated Cd surface atoms

in which a high percentage of surface Cd is bound to OA. As a result, desorption of surface Cd is energetically expensive, making the intermediate state less stable. In Fig. 2.4, we contrast the two reaction mechanisms. For an OA-capped CdSe cluster, there is a large energetic barrier to Cu ion doping because of the higher energy cost of creating a surface Cd vacancy. However, once a cluster is doped, the formation of a Cd vacancy creates a negatively charged surface site that further stabilizes Cu doping events and vacancy formation. This mechanism is similar to what we proposed in an earlier study of cation exchange in 4 nm CdSe nanocrystals. In the case of TOP-capped CdSe clusters, the intermediate stage structure consisting of a Cu-doped CdSe NC with surface Cd vacancies is metastable. There is a second energetic barrier associated to further doping.

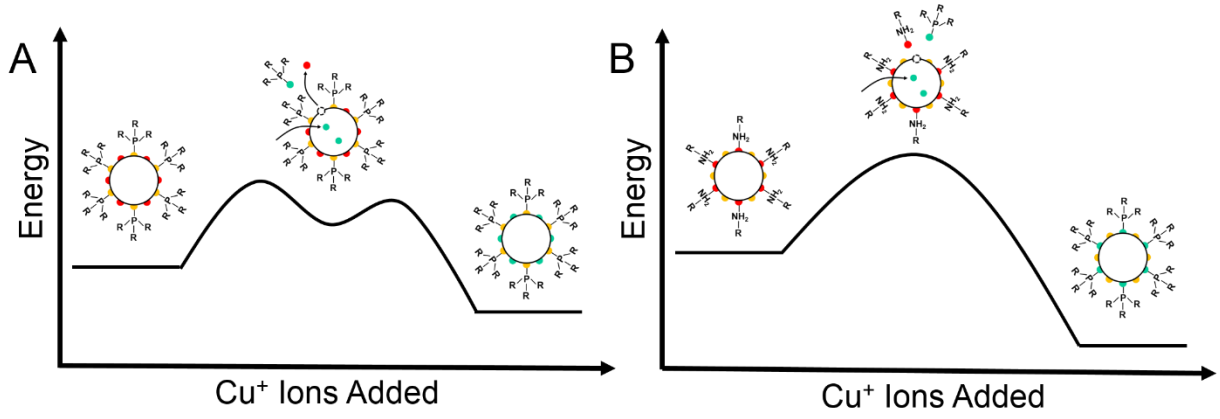

Figure 2.4 *Proposed reaction mechanism of cation exchange in the presence of TOP (left) and in the absence of TOP (right). In (A), the initial cluster is capped with TOP passivated selenium atoms (yellow dots) and unpassivated cadmium atoms (red dots). In (B), the initial cluster is capped with OA passivated cadmium atoms and unpassivated selenium atoms. Doping with copper atoms (green dots) leads to the formation of cadmium vacancies (white dots). There is a higher energetic cost associated with removing an OA passivated cadmium atom than removing an unpassivated cadmium atoms. The presence of TOP passivated selenium surface atoms could also lead to stabilization of an intermediate with surface cadmium vacancies in (A).*

2.4 Conclusion

Ultrasmall CdSe clusters have a size and surface-to-volume atom fraction that make their optical properties highly sensitive to small changes in doping and defect density and to changes occurring at the particle-solution interface. We have found that cation exchange of homogeneous CdSe clusters with Cu^+ ions in solution leads to the formation of an optically distinct intermediate. Isolation and characterization of this intermediate suggests that there is a stable, long-lived Cu doped intermediate formed during cation

exchange of CdSe clusters. By altering the surface chemistry of these CdSe clusters and introducing ligands that more strongly bind surface Cd^{2+} ions, we find a cation exchange pathway that does not involve such a stable intermediate. In other words, the stability of the intermediate is dependent on the surface ligand chemistry, specifically on the presence of tertiary phosphines. Based on this we propose that the energetic cost of creating a Cd surface vacancy is what differentiates these two cation exchange transformations: in the absence of ligands that can bind surface Cd atoms, the energetic cost of creating a surface vacancy is lower, creating a metastable structure. Although ultrasmall clusters are likely more sensitive to changes occurring at the surface, the formation of surface cationic vacancies is central to the cation exchange transformation. The role of surface ligands in the stabilization of reaction intermediate is likely applicable to a wide range of materials in which surface atom removal and/or vacancy formation play a role.

2.5 Methods

Chemicals. Cadmium acetate dehydrate (98+%) was purchased from Sigma Aldrich. Trioctylphosphine (97%) and tetrakis(acetonitrile)copper (I) hexafluorophosphate (98+%) were purchased from Strem Chemicals. Oleic acid (90%), 1-octylamine (99%), and Se powder (99.5%) were purchased from Alfa Aesar. Anhydrous toluene, methanol, and acetonitrile were obtained from DriSolv.

Synthesis of CdSe clusters. The procedure for the synthesis of CdSe clusters was adapted from Yu et al.[9] Cadmium acetate (0.20 mmol, 53.3 mg) and oleic acid (0.13 mmol, 41 μL) were added to a 25 mL three-neck flask. The flask was repeatedly purged with Ar to remove O_2. Under Ar, 5 g of trioctylphosphine (TOP) was added to the flask using a syringe. The resulting solution was heated to 120 ^{o}C and subject to vacuum for 45 min. The contents of the flask was brought to an Ar atmosphere, the temperature was dropped to 100 ^{o}C, and a TOP-Se solution (0.05 mmol, i.e., 4 mg of selenium powder in 0.4 mL of TOP) was added to the flask. The temperature was raised to 120 ^{o}C and the reaction was allowed to proceed for 60 min. The resulting solution was a light yellow color. After synthesis, the clusters were washed repeatedly with toluene and methanol and dispersed in toluene.

Ligand exchange with octylamine (OA). For CdSe clusters capped with OA, 1 mL of OA was added to the cluster solution after synthesis. The solution immediately turns from one with high turbidity to one with a transparent yellow color. The amine-capped clusters were washed repeatedly with toluene and methanol and dispersed in toluene. UV-vis characterization of OA-capped clusters reveals that the excitonic absorption peak maximum shifts from 406 nm (before ligand exchange) to 415 nm (after ligand exchange).

Exchange with Cu^+. All cation exchange reactions were carried out in an oxygen-free, moisture-free glove box. CdSe clusters were dispersed in toluene. A solution of tetrakis(acetonitrile) copper(I) hexafluorophosphate ($[(CH_3CN)_4Cu]PF_6$) in a methanolic solution (10% methanol in acetonitrile by volume) was then added dropwise to the cluster solution. The reaction mixture was stirred vigorously after each addition. Exchange was monitored by UV-Vis absorption spectroscopy. In exchange reactions where TOP/Cu^+ was the reagent, 1.5 molar equivalents of TOP per equivalent of $[(CH_3CN)_4Cu]PF_6$ was added to the cluster solution.

Absorption spectroscopy. Absorption spectra were collected on a Shimadzu UV-3600 scanning spectrophotometer with a 1 nm step size using either toluene, chloroform, or hexanes as a reference solvent. For the majority of figures, the raw absorption data without corrections is plotted unless otherwise stated.

Analysis of absorption spectra. For Fig. 2.1C, the absorption spectroscopy data was analyzed for the determination of the relative percentages of each cluster species during cation exchange. Spectra comprised of absorption contributions from CdSe, intermediate Cu-doped CdSe, and product Cu_2Se clusters. The absorption contribution of Cu_2Se clusters was determined from the absorption at 650 nm, which is well outside the excitonic band of either the CdSe clusters or the intermediate ones. The percentage of clusters that have converted to the Cu_2Se state at each stage in the titration was determined by dividing the absorbance at 650 nm in each spectrum by the absorbance at 650 nm in the spectrum at the final stage, wherein all clusters have converted to Cu_2Se.

$$\%\ of\ clusters\ in\ Cu_2Se\ state = \frac{Abs.\ at\ 650\ nm}{Abs.\ at\ 650\ nm\ for\ final\ Cu_2Se\ spectrum}$$

The CdSe and intermediate contributions to the absorption were determined by correcting each spectrum as follows.

$$Corrected\ spectrum = Original\ spectrum - (Final\ Cu_2Se\ spectrum) \times (\%\ Abs.of\ Cu_2Se)$$

From corrected spectra, the separate percent contributions of CdSe and intermediate states were determined. The percentage of clusters in the CdSe state at each stage was determined by dividing the absorbance at 406 nm (425 nm) in each spectrum by the absorbance at 406 nm in the spectrum at the initial stage, wherein all clusters are in the CdSe state:

$$\%\ clusters\ in\ the\ CdSe\ state = \frac{Abs.\ at\ 406\ nm}{Abs.\ at\ 406\ nm\ for\ initial\ CdSe\ spectrum}$$

Likewise, the percentage of clusters in the intermediate state was determined by dividing the absorbance at 425 nm in each spectrum by the absorbance at 406 nm in the spectrum at the initial stage, wherein all

clusters are in the CdSe state. It must be noted that for analysis of spectra where both the exciton at 406 nm and the one at 425 nm are present, the exciton peaks were fit to individual Gaussian functions and the height of each Gaussian was used as a measure of the absorbance of the respective exciton.

X-ray photoelectron spectroscopy (XPS). XPS analysis was performed on CdSe, intermediate, and Cu_2Se clusters, determined from absorption spectra. A Kratos Axis ULTRA instrument was used, which employs a monochromatized Al Kα X-ray source of 15 kV. For each sample, the carbon 1s peak was used as a reference. Background subtracted peaks were fit to single Voigt functions and peak areas were used to determined atomic percentages of Se, Cd, and Cu in each sample.

Electron microscopy. High-resolution electron microscopy (HRTEM) images and high-angle annular dark-field STEM (HAADF-STEM) images were acquired on a JEOL 2010F field-emission TEM instrument operating at 200 kV. Samples were prepared by drop-casting clusters on ultrathin carbon TEM grids followed by repeated washing with methanol followed by drying *in vacuo*.

NC morphology. HRTEM and HAADF-STEM images (Fig. 2.7) show the morphology of initial CdSe clusters and cation-exchanged Cu_2Se clusters. Sizing analysis was performed on CdSe and Cu_2Se clusters using HAADF-STEM images. Cluster sizes (measured along the short axis for non-spherical domains) were estimated from HAADF-STEM images manually in Image J by using the line tool and. Data from ~50 clusters was used for the determination of average size and size distributions. HRTEM images show crystallinity of clusters before and after cation-exchange and the change in lattice parameter from CdSe to Cu_2Se.

Powder X-ray diffraction (PXRD). PXRD patterns were collected on a Rigaku Miniflex 600 powder X-ray diffractometer operated at full power (40kV - 15 mA) with Cu K_α radiation with a wavelength of 1.54 Å. Data was collected in reflection mode from $2\theta = 15^o$-65^o using step-wise scans of 0.04^o with scans running for 2-3 h. Samples were drop-cast into thick films on a zero-background quartz slide.

X-Ray diffraction simulations. Calculated powder diffraction patterns were generated using the program Powder Cell, which generates a powder pattern based on a structure factor calculation from lattice parameters and atomic positions.[20] Input cell parameters used for simulations presented in Fig. 2.3 are given in Table 2.2. The calculated powder patterns also include peak broadening due to small crystallite size determined through the Debye-Scherrer equation:

$$B(2\theta) = \frac{K\lambda}{L\cos\theta}$$

where B is the full-width-half-max (FWHM) of the peak in 2θ ^{o} units, K is the Scherrer constant assumed here to have a value of 0.94, λ is the X-ray wavelength, θ is the Bragg angle, and L is the crystallite size assumed to be 2 nm.

2.6 Additional figures

Table 2.2 *Lattice parameters and occupancies for calculated XRD patterns shown in Fig. 2.3*

Table 2.2 Parameters for calculated XRD patterns

2 nm – CdSe			Space Group: *F-43m*, a = 6.0 Å		
Element	**Wycoff Pos.**	**x**	**Y**	**Z**	**Occ.**
Se	4a	0	0	0	1
Cd	4c	0.25	0.25	0.25	1
2 nm – Intermediate CdSe			Space Group: *F-43m*, a = 6.0 Å		
Element	**Wycoff Pos.**	**x**	**y**	**z**	**Occ.**
Se	4a	0	0	0	1
Cd	4b	0.5	0.5	0.5	0.5
Cu	24f	0.25	0	0	0.1667
2 nm – Cu_2Se			Space Group: *Fm-3m*, a = 5.85 Å		
Element	**Wycoff Pos.**	**x**	**y**	**z**	**Occ.**
Se	4a	0	0	0	1
Cu	8c	0.25	0.25	0.25	0.3
Cu	4b	0.5	0.5	0.5	0.3
Cu	24e	0.25	0	0	0.1833

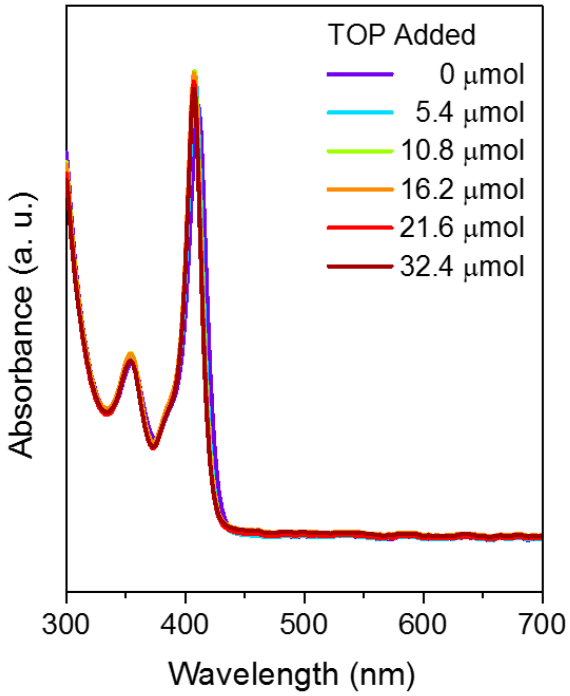

Figure 2.5 *In a control experiment, we monitored the optical absorption spectrum of a solution of TOP-capped CdSe clusters in toluene as a solution of TOP (20 mg) in methanol (10%) and acetonitrile (90%) was added. The spectrum showed no significant changes. The amount of TOP added in this control experiment is representative of the amount of TOP added during a titration with TOP/Cu^{+}. Absorption spectra are plotted here without any correction or scaling.*

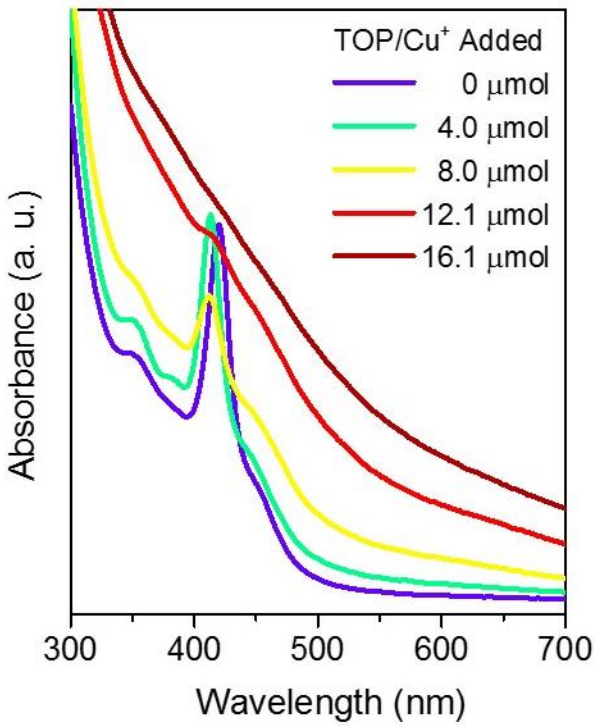

Figure 2.6 *A titration was also carried out in which Cu^+ was added in the form of a methanolic solution of TOP/Cu^+ to a solution of OA-capped CdSe clusters in toluene. Optical absorption spectra acquired in the course of the titration do not reveal the formation of the intermediate structure which is seen in the experiments without OA. One may note a shoulder in all spectra around 445 nm, however this band is distinct from the 425 nm position of the intermediate excitonic peak and is presumed to be from aggregates present in the initial CdSe cluster solution formed as a result of the ligand exchange procedure.*

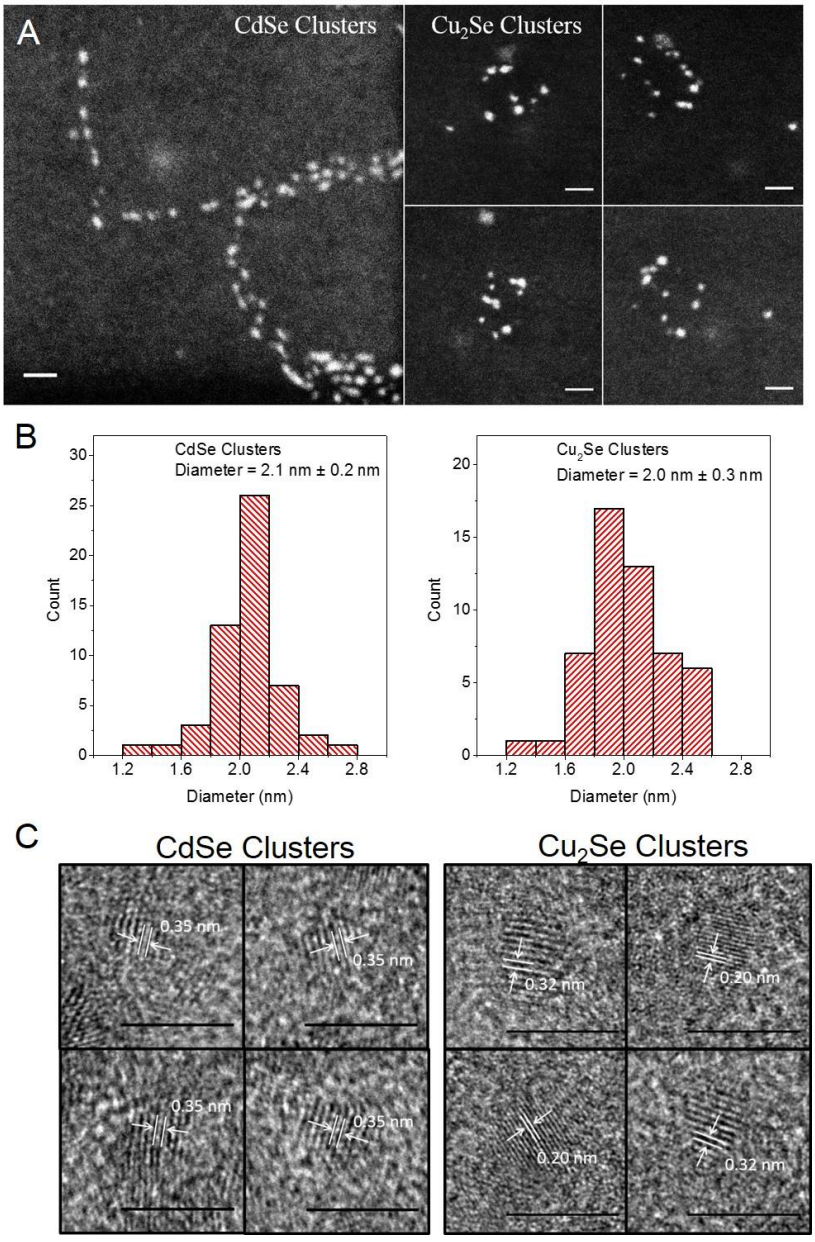

Figure 2.7 *HAADF-STEM imaging reveals that the initial CdSe clusters (image on left) retain their shape and size during cation exchange to Cu_2Se clusters (four images on right). Cluster sizes (measured along the short axis for non-spherical domains) were estimated from HAADF-STEM images manually in Image J by using the line tool. A histogram of the sizes of ~50 clusters shows that the average size is ca. 2 nm both before and after cation exchange, with a standard deviation of 0.2 nm before exchange and of 0.3 nm after exchange. HRTEM imaging shows that the crystallinity of the clusters is preserved during exchange. Before exchange, CdSe clusters display lattice fringes with a d-spacing of 0.35 nm assigned to {111} planes. After exchange, Cu_2Se clusters display lattice fringes with d-spacings of 0.32 nm and 0.20 nm corresponding to {111} and {220} planes, respectively. Scale bars in (A) represent 10 nm. Scale bars in (C) represent 5 nm.*

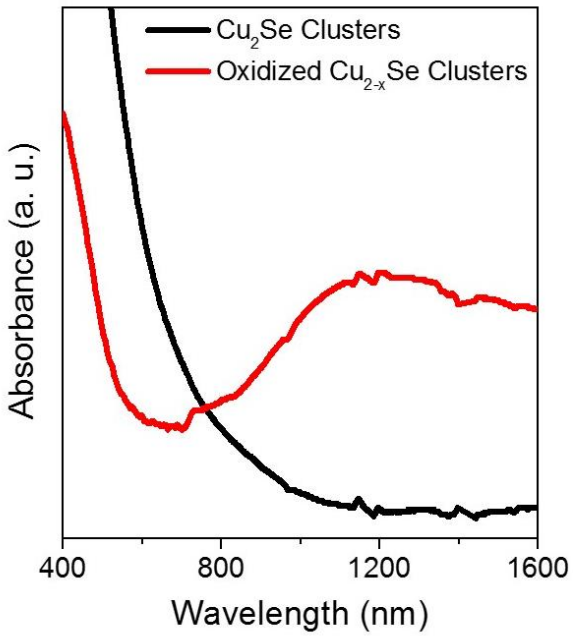

Figure 2.8 *UV-Vis-NIR absorption spectra of exchanged Cu_2Se clusters before (black line) and after (red line) 4 h of air exposure show the emergence of a near-infrared (NIR) plasmonic resonance band in the clusters upon oxidation. Oxidation in air leads to the removal of Cu^0 from the Cu_2Se lattice. The resulting formation of Cu vacancies leads to a heavily p-doped material with a NIR plasmon resonance. The oxidation of Cu_2Se clusters to $Cu_{2-x}Se$ clusters accompanied by the development of a NIR plasmonic resonance shows that, despite their ultrasmall size, $Cu_{2-x}Se$ clusters preserve the hallmark properties of $Cu_{2-x}Se$ solids.*

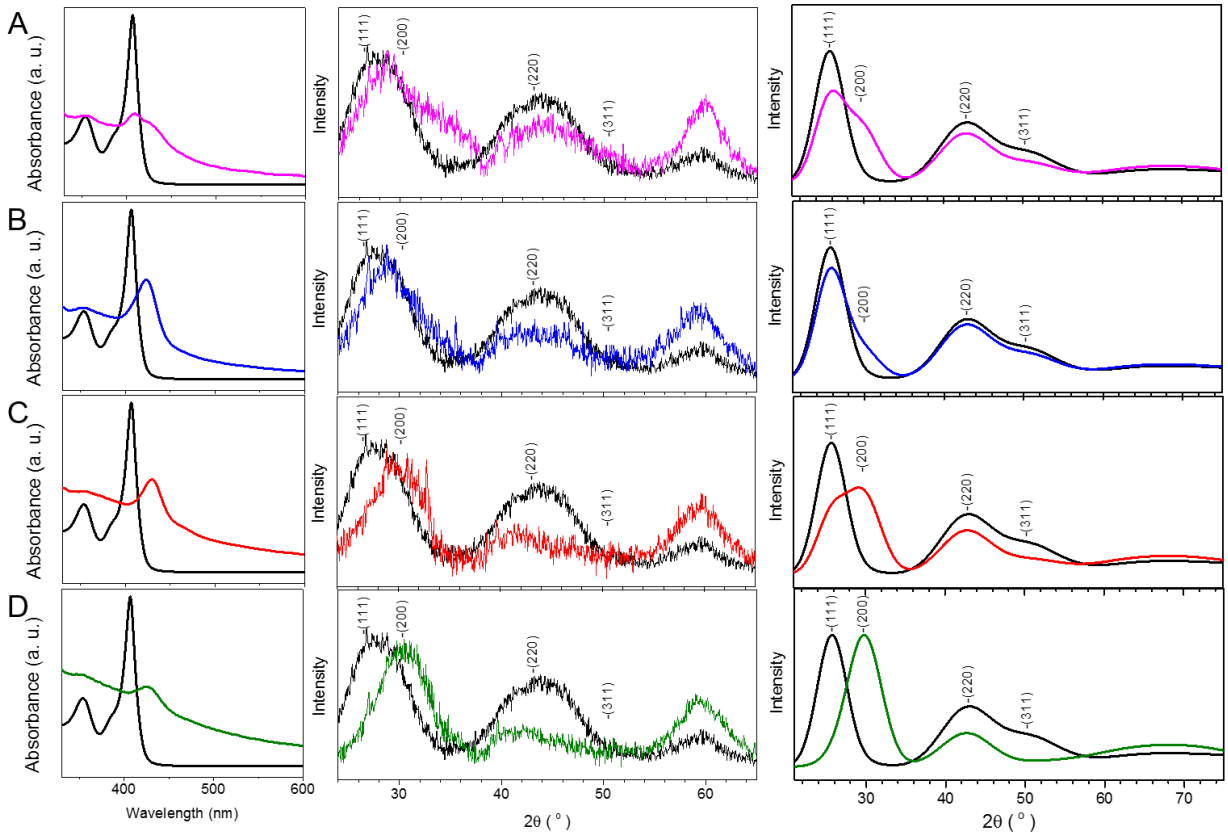

Figure 2.9 *UV-vis absorption spectra (left column) and experimental PXRD patterns (middle column) of intermediate clusters (with an exciton peak at 425 nm) at various points in the course of exchange (from A to D). For comparison, the absorption spectrum and PXRD pattern of the initial CdSe clusters is shown by black curves. It is seen from the PXRD patterns that at further points in the exchange (B, C &D), there is a decrease in the {111} peak intensity, an increase in the {200} peak intensity, and a near-complete suppression of the {311} peak intensity. Simulated XRD patterns (right column) were generated through a linear combination of simulated XRD patterns of two structures, the initial zincblende CdSe structure and the intermediate Cu-doped CdSe structure from Fig. 2.3B. The simulations that provided a close match to the experimental patterns were found to consist of the following combination of the two structures: (A) 60% CdSe, 40% Intermediate, (B) 80% CdSe, 20% Intermediate, (C) 40% CdSe, 60% Intermediate, and (D) 100% Intermediate. Experimental XRD patterns were scaled such that the {111} or {200} peak intensity was approximately similar across the four samples (A-D). Absorption spectra, which varied in peak height due to differences in concentration, were appropriately scaled for easy comparison. In simulated XRD patterns, Debye-Scherrer peak broadening corresponding to a 2 nm crystallite size was included.*

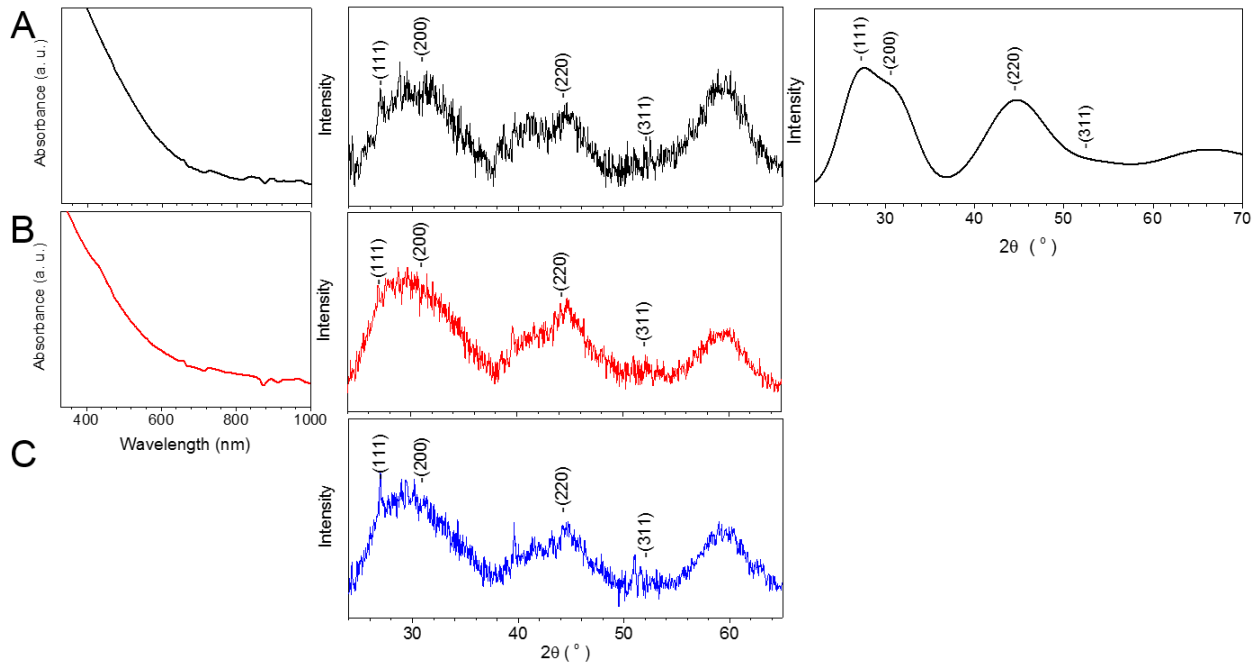

Figure 2.10 *PXRD patterns (middle column) of fully exchanged, Cu_2Se cluster samples alongside their absorbance spectra (left column). Multiple examples (A, B, and C) are shown to indicate reproducibility. The {220} diffraction peak at $2\theta = 45^o$ that is absent in the intermediate cluster sample is seen to be restored in the fully exchanged sample. The experimental XRD patterns match the simulated pattern shown in the rightmost column and in Fig. 2.3. In the simulated XRD pattern, Debye-Scherrer peak broadening corresponding to a 2 nm crystallite size was included.*

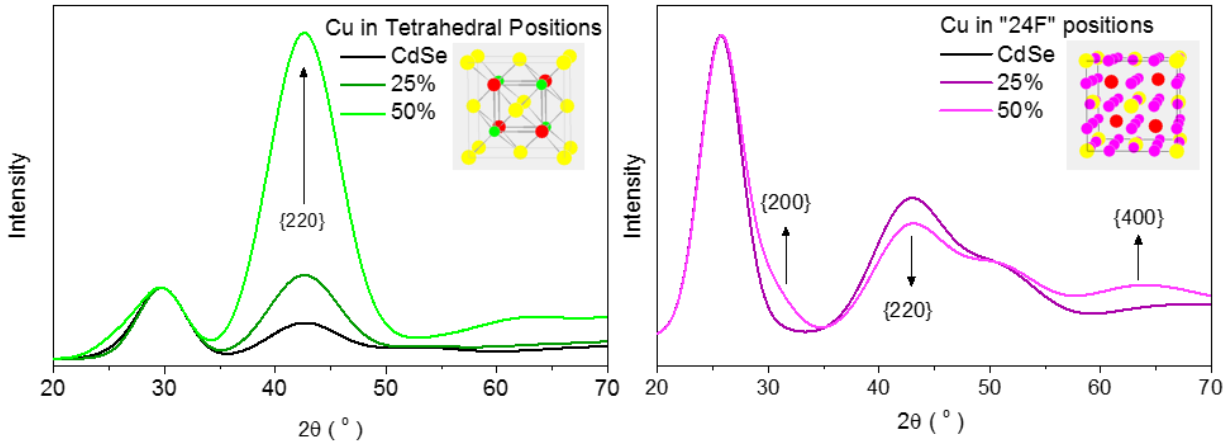

Figure 2.11 *Simulated diffraction patterns of zincblende CdSe (with Se atoms shown in yellow and Cd atoms in red) with Cu^+ dopants in different locations. The calculated diffraction pattern of the initial, undoped zincblende CdSe structure is shown by black curves. (left) When an increasing percentage of Cu^+ ions are placed in tetrahedral positions (indicated by green) within the zincblende lattice, simulations show an increase in the {220} peak intensity. Since experimentally, the Cu-doped intermediate exhibits a decreased {220} peak intensity, we can rule out tetrahedral sites as the initial location of added Cu^+ dopants. (right) When an increasing percentage of Cu^+ ions are placed in the zincblende lattice in 24F positions (indicated in pink) such as (¼, 0, 0)*a, simulations show a decrease in the {220} peak intensity and an increase in the {200} and {400} peak intensities, reproducing the trends seen in experimental PXRD patterns. Thus, initial Cu^+ dopants occupy 24F interstitial sites rather than tetrahedral sites. The simulated XRD patterns were scaled by normalizing the {111} peak intensity to a value of 1. In simulated XRD patterns, Debye-Scherrer peak broadening corresponding to a 2 nm crystallite size was included.*

2.7 References

1. Kasuya, A. *et al.* Ultra-stable nanoparticles of CdSe revealed from mass spectrometry. *Nat. Mater.* **3,** 99–102 (2004).

2. McBride, J. R., Dukes, A. D., Schreuder, M. A. & Rosenthal, S. J. On ultrasmall nanocrystals. *Chem. Phys. Lett.* **498,** 1–9 (2010).

3. Kudera, S. *et al.* Sequential growth of magic-size CdSe nanocrystals. *Adv. Mater.* **19,** 548–552 (2007).

4. Cossairt, B. M., Juhas, P., Billinge, S. & Owen, J. S. Tuning the Surface Structure and Optical Properties of CdSe Clusters Using Coordination Chemistry. *J. Phys. Chem. Lett.* **2,** 3075–3080 (2011).

5. Newton, J. C. *et al.* Low-temperature synthesis of magic-sized cdse nanoclusters: Influence of ligands on nanocluster growth and photophysical properties. *J. Phys. Chem. C* **116,** 4380–4389 (2012).

6. Faucheaux, J. A., Stanton, A. L. D. & Jain, P. K. Plasmon Resonances of Semiconductor Nanocrystals: Physical Principles and New Opportunities. *J. Phys. Chem. Lett.* **5,** 976–985 (2014).

7. White, S. L., Smith, J. G., Behl, M. & Jain, P. K. Co-operativity in a nanocrystalline solid-state transition. *Nat. Commun.* **4,** 2933 (2013).

8. Ott, F. D., Spiegel, L. L., Norris, D. J. & Erwin, S. C. Microscopic theory of cation exchange in CdSe nanocrystals. *Phys. Rev. Lett.* **113,** (2014).

9. Yu, K. *et al.* Thermodynamic equilibrium-driven formation of single-sized nanocrystals: Reaction media tuning CdSe magic-sized versus regular quantum dots. *J. Phys. Chem. C* **114,** 3329–3339 (2010).

10. Jasieniak, J. & Mulvaney, P. From Cd-rich to Se-rich - The manipulation of CdSe nanocrystal surface stoichiometry. *J. Am. Chem. Soc.* **129,** 2841–2848 (2007).

11. Evans, C. M., Evans, M. E. & Krauss, T. D. Mysteries of TOPSe revealed: Insights into quantum dot nucleation. *J. Am. Chem. Soc.* **132,** 10973–10975 (2010).

12. Rempel, J. Y., Trout, B. L., Bawendi, M. G. & Jensen, K. F. Density functional theory study of ligand binding on CdSe (0001), (0001??), and (112??0) single crystal relaxed and reconstructed surfaces: Implications for nanocrystalline growth. *J. Phys. Chem. B* **110,** 18007–18016 (2006).

13. Anderson, N. C. & Owen, J. S. Soluble, chloride-terminated CdSe nanocrystals: Ligand exchange monitored by 1H and 31P NMR spectroscopy. in *Chemistry of Materials* **25,** 69–76 (2013).

14. Landes, C., Braun, M., Burda, C. & El-Sayed, M. A. Observation of Large Changes in the Band Gap Absorption Energy of Small CdSe Nanoparticles Induced by the Adsorption of a Strong Hole Acceptor. *Nano Lett.* **1,** 667–670 (2001).

15. Jawaid, A. M., Chattopadhyay, S., Wink, D. J., Page, L. E. & Snee, P. T. Cluster-seeded synthesis of doped CdSe:Cu4 quantum dots. *ACS Nano* **7,** 3190–3197 (2013).

16. Justo, Y. *et al.* Less is more. Cation exchange and the chemistry of the nanocrystal surface. *ACS Nano* **8,** 7948–7957 (2014).

17. Lim, S. J., Kim, W. & Shin, S. K. Surface-dependent, ligand-mediated photochemical etching of

CdSe nanoplatelets. *J. Am. Chem. Soc.* **134,** 7576–7579 (2012).

18. Siy, J. T. & Bartl, M. H. Insights into reversible dissolution of colloidal cdse nanocrystal quantum dots. *Chem. Mater.* **22,** 5973–5982 (2010).

19. Li, R. *et al.* Amine-assisted facetted etching of CdSe nanocrystals. *J. Am. Chem. Soc.* **127,** 2524–2532 (2005).

20. Nolze, G. & Kraus, W. PowderCell 2.0 for Windows. *Powder Diffr.* **13,** 256–259 (1998).

Chapter 3: Superionic copper selenide clusters*

3.1 Abstract

Cation exchange is a synthetic technique that can be used to obtain materials in new size regimes. We utilize cation exchange of magic-size clusters to template the synthesis of ultra small copper selenide clusters. Through comparison of the optical and structural properties of ultrasmall Cu_2Se clusters to larger Cu_2Se nanocrystals (NCs) made though a similar synthetic method, we have discovered that atomic structures of Cu_2Se are affected by a decrease in crystallite size. In particular, we have found that the crystal structure associated with the high temperature superionic phase is stable at ambient temperature in ultrasmall Cu_2Se clusters suggesting that the phase transition temperature to the high temperature superionic phase is depressed to below room temperature at ultrasmall crystallite size and that ultrasmall Cu_2Se clusters have potential as room temperature superionic conductors.

3.2 Introduction

The field of nanoscience is rife with examples of nano-size crystals displaying unique optical, electronic, chemical, and structural materials properties not found in their bulk counterparts. For example, when crystallite size is reduced to the nanoscale, quantum effects lead to discretization of energy levels in the conduction and valence bands which can affect the energy of opto-electronic transitions in the nanoscale material.[1,2] As crystallite size is reduced in a material, there is a resulting increase in the proportion of surface energy to internal bulk energy in each nanocrystal which can affect the thermodynamic stability of the overall nanocrystalline phase.[3] The depression of order-disorder phase transition temperatures or melting point temperatures is common when crystallite size is reduced to the nanoscale as well as the stabilization of different crystal phases, occasionally allowing high energy, metastable phases to be accessed at ambient conditions.[4–6] Furthermore, it has long been known that an increase in interface-to-volume ratio in ionic materials, through reduction in size or increase in nanostructuring of interfaces, can lead to a decrease in the formation energy of defects and increases in ionic transport in solids.[7,8] Investigation of how nanocrystal size affects the electronic and structural properties of materials is limited by the ability to synthesize materials uniformly on very small size regimes. The implementation of cation

* Reproduced with permission from: S. L. White, P. Banerjee, P. K. Jain, Superionic copper selenide clusters. *In preparation*

exchange as a tool for post-synthetically altering the composition of ionic nanomaterials has expanded the number of materials that can be made in very small size regimes.[9]

In this study, we employ cation exchange to make ultrasmall clusters of copper (I) selenide (Cu_2Se). Through the addition of Cu^+ ions in solution to an ensemble of 2 nm magic-size cadmium selenide (CdSe) clusters, we are able to isolate a monodisperse solution of Cu_2Se clusters that preserve the initial selenium anionic framework, and hence ultrasmall size, of the original clusters. Cu_2Se is a material of interest because: (1) it can be easily doped to a carrier density at which it is a NIR plasmonic semiconductor[10,11] and (2) at high temperature it undergoes an order-disorder phase transition to a superionic conducting material.[12,13] Superionic conductors are solids with ionic conductivities akin to molten salts. Many chalcogenide and halide salts with Ag^+ and Cu^+ cations are known for displaying high-temperature crystallographic phases with high cationic conductivity, as high as 4-5 Ω^{-1} cm^{-1} for silver chalcogenides.[14] Generally, these materials undergo a first-order phase transition at some critical temperature from a rigid lattice phase in which cations are in an ordered structure to a high temperature superionic phase in which cations are mobile and statistically occupy a variety of interstitital sites much greater in number than the total number of cations in the unit cell.[15] This phase transition is often accompanied by a structural transition of both the mobile cationic and immobile anionic sub-lattice. The high temperature superionic phase of Cu_2Se has a rigid selenium ion sub-lattice and a liquid-like copper ion sub-lattice. Through comparison of the optical and structural properties of ultrasmall Cu_2Se clusters to larger Cu_2Se nanocrystals (NCs) made though a similar synthetic method, we have discovered that both of these properties are affected by a decrease in crystallite size. Remarkably, we have found that the crystal structure associated with the high temperature superionic phase is stable at ambient conditions in ultrasmall Cu_2Se clusters suggesting that the phase transition temperature to the high temperature superionic phase is depressed to below room temperature at ultrasmall crystallite size and that ultrasmall Cu_2Se clusters are room temperature superionic conductors. The ability to use crystallite size to tune the structure, and hence ionic conduction, of Cu_2Se could allow for the development nanostructured Cu_2Se superionic materials for applications like solid-state electrolytes for energy storage devices and ionic switches.[16]

3.3 Results

3.3.1 Cation exchange as a route to 2 nm Cu_2Se clusters

Ultrasmall Cu_2Se clusters were obtained though solution phase cation exchange of magic-size CdSe clusters with Cu^+ ions. Magic-size CdSe clusters are a class of single-sized, stable clusters approximately 2 nm in diameter that have an extremely sharp $1S_h$-$1S_e$ excitonic absorption peak.[17–19] After the addition of an

excess of Cu^+ ions in solution, the narrow $1S_h$-$1S_e$ excitonic absorption band is replaced by band-edge absorption from Cu_2Se clusters. (Fig. 3.1A) High angle annular dark field scanning transmission electron microscopy (HAADF-STEM) images after cation exchange were used to verify that the resulting Cu_2Se clusters were spherical and maintained a diameter of 2 nm, preserving the size and morphology of the initial CdSe clusters. (Fig. 3.1B & 3.1C) To further validate that the initial selenium anionic sub-lattice of the initial CdSe clusters is preserved, we performed a second cation exchange of the Cu_2Se clusters with Cd^{2+} ions in solution to return the clusters to the initial CdSe composition. The $1S_h$-$1S_e$ excitonic absorption band, the energy of which is highly size-dependent due to quantum confinement of the exciton and hence an indication of particle size, reappears at the same energy wavelength (406 nm) verifying that the clusters preserve their size through multiple cation exchange transformations. (Fig. 3.1D) We do observe broadening of the exciton which could be attributed to residual Cu impurities and/or native defects in the lattice.

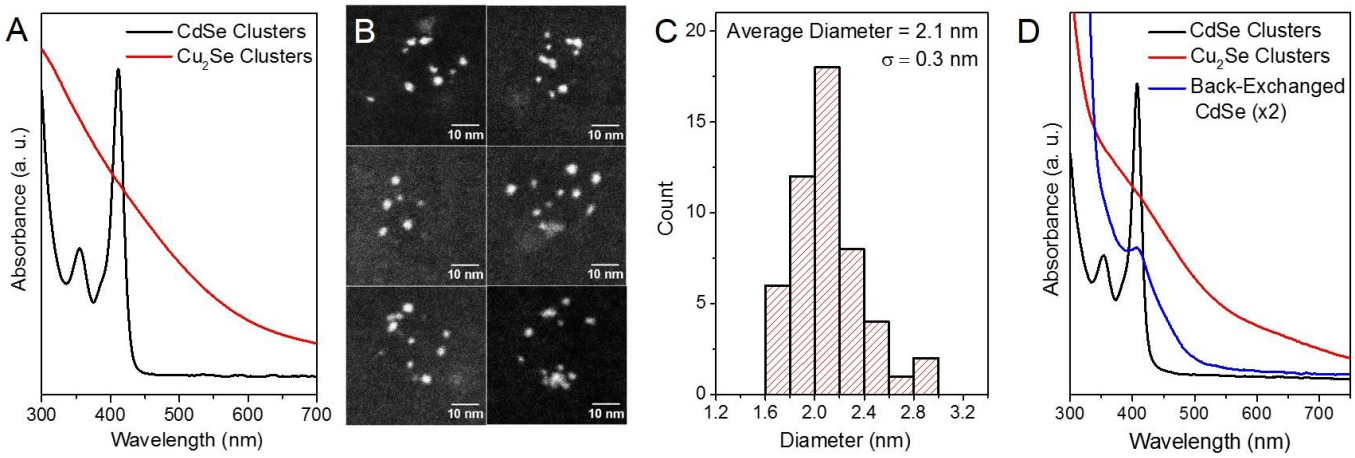

Figure 3.1 Cation exchange as a route to 2 nm Cu_2Se clusters. *Excitonic absorption spectra (A) of ultrasmall CdSe clusters before (black spectrum) and after (red spectrum) cation exchange with Cu^+ ions in solution is characterized by the disappearance of the CdSe exciton at 406 nm and the appearance of band-edge absorption of the indirect bandgap semiconductor Cu_2Se. HAADF-STEM images (B) of Cu_2Se clusters after exchange were used to show that cation exchange of CdSe clusters results in discrete Cu_2Se clusters with an average diameter of 2.1 nm ± 0.3 nm. Further evidence that the size and monodispersity of the original CdSe clusters is preserved during cation exchange comes from the return of the size-dependent excitonic energy to 406 nm (C, blue spectrum) after a second cation exchange of the clusters from Cu_2Se to CdSe through exposure to an excess of Cd^{2+} ions in solution.*

3.3.2 Cu_2Se clusters sustain localized surface plasmon resonances

Despite structural differences between ultrasmall Cu_2Se clusters and larger NCs, Cu_2Se clusters exhibit a hallmark property of Cu_2Se nanomaterials: tunable localized surface plasmon resonances (LSPRs). Cu_2Se can exist at a range of stoichiometries: $Cu_{2-x}Se$ in which $0 \leq x \leq 0.3$. Upon exposure to air, O_2 removes Cu^0 from the lattice, creating Cu vacancies and a positive charge carrier density capable of sustaining a LSPR in the near-infrared.[10] (Fig. 3.2D) We compared the evolution of plasmonic absorption spectra of 2 nm Cu_2Se clusters during oxidation in air to that of 6 nm Cu_2Se NCs made through a similar synthesis and cation exchange procedure. (Fig. 3.2A and 3.6A) It was observed that Cu_2Se clusters undergo oxidation in air at a slower rate than larger particles (Fig. 3.2C); but that the peak energy of the LSPR was similar for both clusters and NCs (1.06 eV and 0.99 eV respectively, Fig. 3.2A and 3.6A). Upon exposure to a reducing agent such as cobaltocene, electrons are injected back into Cu_2Se clusters and the NIR LSPR red-shifts while decreasing in intensity. (Fig. 3.2B) Similar behavior is observed for larger 6 nm NCs. (Fig. 3.6B).

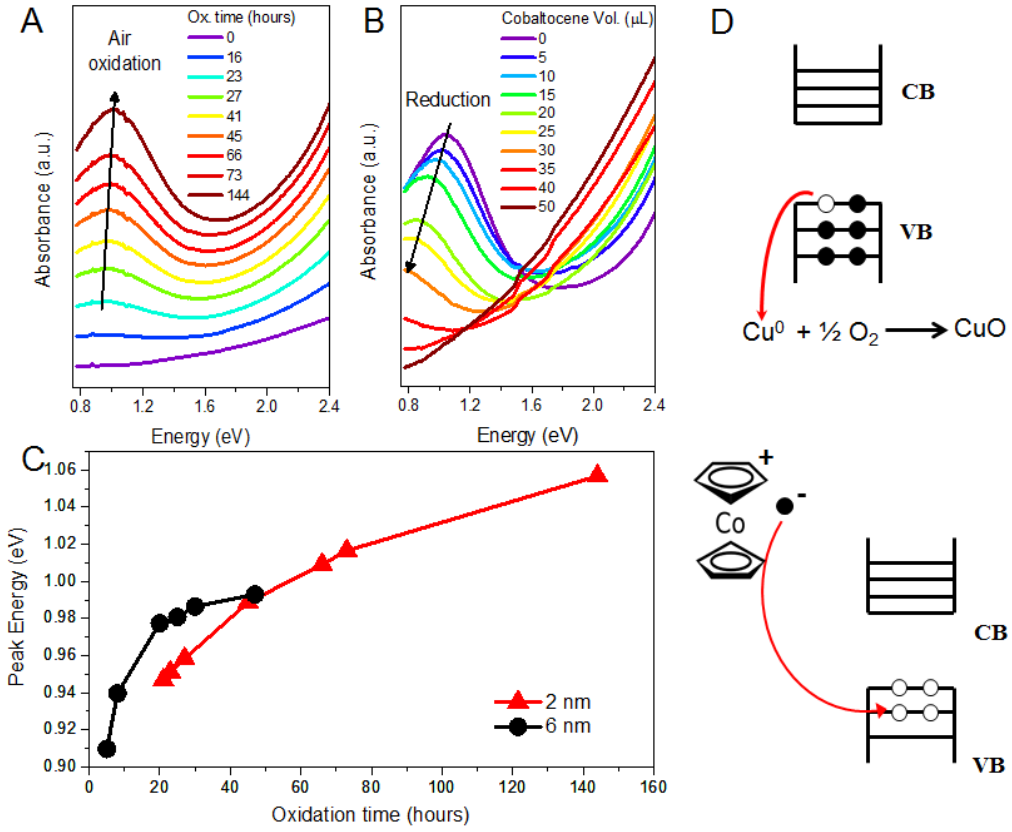

Figure 3.2 Cu_2Se clusters display tunable NIR LSPRs. *As Cu_2Se clusters are exposed to O_2 in air, a LSPR absorption band in the NIR region appears. (A) The addition of cobaltocene reverses this effect. (B) The increase in carrier density during oxidation occurs at a slower rate in Cu2Se clusters than in larger 6 nm Cu_2Se NPs. A schematic of oxidation and reduction of Cu_2Se is shown in (D).*

3.3.3 Unique structural properties of Cu_2Se clusters.

Aside from being a plasmonic semiconductor, Cu_2Se has unique structural and electronic properties including the fact that, at high temperature, it undergoes an order-disorder phase transition to a superionic conducting phase. At temperatures above 130 °C, stoichiometric Cu_2Se (HT α-Cu_2Se) forms a cubic structure in which Se ions form a rigid, face-centered cubic (*fcc*) sub-lattice and Cu ions form a liquid-like mobile sub-lattice. Upon cooling, the structure of Cu_2Se (LT β-Cu_2Se) loses symmetry and relaxes into a larger and distorted supercell with a pseudo-cubic structure and Cu^+ ions become localized at lower energy, interstitial sites.

As shown by multiple x-ray and neutron diffraction studies, the HT α-Cu_2Se phase has a cubic lattice similar to the anti-fluorite structure in which Se ions occupy *fcc* positions and Cu atoms form a mobile sub-lattice by migrating between *8c* tetrahedral lattice sites via interstitial *32f* trigonal lattice sites.[12,20–22] As a result, the mobile Cu ion sub-lattice can be described as occupying predominantly *8c* tetrahedral lattice sites with some occupancy of *32f* trigonal lattice sites. Competing models of the structure of LT β-Cu_2Se exist with most claiming that LT β-Cu_2Se forms a slightly distorted version of the cubic anti-fluorite structure in which there is an elongation along the {111} lattice plane lowering the symmetry as compared to the HT α-Cu_2Se unit cell.[13,22–24] No longer in a liquid-like mobile phase, Cu ions localize into lower energy interstitial sites in the distorted LT β-Cu_2Se structure with the highest occupancy being on the *32f* trigonal sites. Ordering of the resulting tetrahedral vacancies in relation to specific lattice planes contributes to a change in the periodicity of the LT β-Cu_2Se phase along those same lattice planes.

3.3.4 Electron microscopy detects the absence of Cu vacancy ordering in Cu_2Se clusters

During the HT α-Cu_2Se to LT β-Cu_2Se phase transition, Cu atoms migrate from *8c* tetrahedral sites and become localized at *32f* tetragonal positions, increasing the number of vacant *8c* tetrahedral sites. Rather than randomly arranging, tetrahedral Cu vacancies stack every four Cu layers along the {111} axis creating a superstructure that can be observed via electron diffraction patterns and electron microscopy images.[13,24] To probe the effects of crystallite size on the structure of 2 nm Cu_2Se clusters, we compared high-resolution transmission electron microscopy (HR-TEM) images of 2 nm Cu_2Se clusters to images of larger 4 nm and 6 nm Cu_2Se nanocrystals (NCs) prepared through a similar synthesis and cation exchange procedures. (Section 3.6)

Several images of 2 nm, 4 nm, and 6 nm Cu_2Se NCs were analyzed for the presence of tetrahedral vacancy ordering and the resulting superstructure. Representative images of four NCs in each size regime are shown in Fig. 3.3 and all images used for analysis are shown in Fig. 3.7, 3.8, and 3.9. We observed a stark contrast between the high-resolution lattice images of 6 nm, 4 nm, and 2 nm Cu_2Se NCs. Along the {111} axis of 6 nm NCs, fringes display a contrast periodicity with a period that is twice that typically seen for the {111}. The distance between fringes of high and low contrast was measured to be 0.67 nm, which corresponds to the distance between Cu vacancy planes and matches the assigned tetrahedral vacancy distance in previous studies.[13] This contrast pattern arising from vacancy-ordered superstructure was measured between {111} planes in 80% of the 6 nm NCs in which lattice fringe patterns corresponding to the {111} planes were observed. When the size of the NCs was reduced to 4 nm, it was observed in only 10% of NCs in which lattice fringe patterns corresponding to the {111} planes were observed. Remarkably, it was completely absent in 2 nm clusters where lattice fringes displayed only the typical 0.32 nm periodicity associated with interatomic spacing along the {111}.

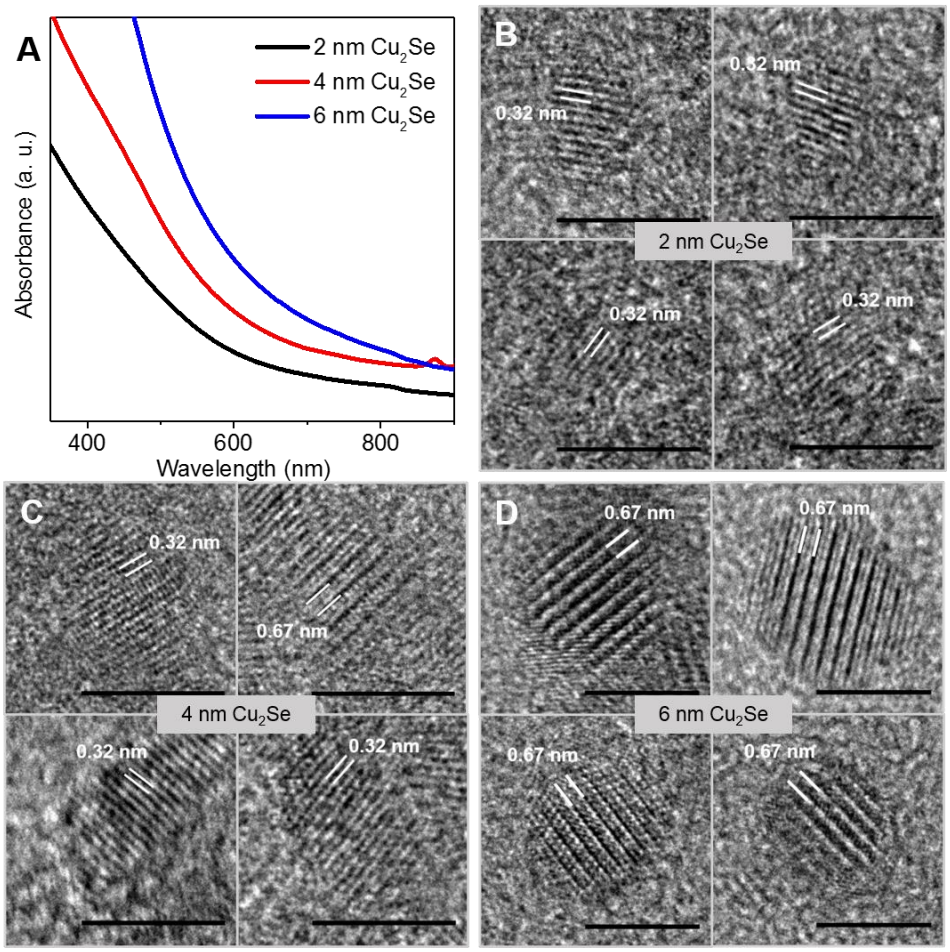

Figure 3.3 Superstructure in 2 nm, 4 nm, and 6 nm Cu_2Se nanocrystals. *High resolution transmission electron microscopy (HRTEM) reveals that superstructure is absent in 2 nm Cu_2Se clusters. Measured lattice spacings between {111} planes are shown for representative HRTEM images of four NCs in each size regime. Image analysis was performed on ca. 30 NCs in each size regime and the percentage of NCs displaying superstructures is given in Table 3.1. All images used for analysis are shown in Fig. 3.7, 3.8, and 3.9. Scale bar shown corresponds to 5 nm.*

Table 3.1 *Percentage of nanocrystals with superstructure visible in HRTEM images. All images used for analysis in Fig. 3.7, 3.8, and 3.9.*

Table 3.1 NC superstructure	
NC diameter	% of NCs with superstructure
2 nm	0%
4 nm	10%
6 nm	80%

3.3.5 X-ray diffraction yields insight into cationic sub-lattice in Cu_2Se clusters

Further evidence that crystallite size plays a role in the structure of Cu ion sub-lattice and the LT β-Cu_2Se to the HT α-Cu_2Se phase transition temperature came from powder x-ray diffraction (PXRD) measurements. We compared the XRD pattern of 2 nm Cu_2Se clusters to patterns of 4 nm and 6 nm Cu_2Se NCs. (Fig. 3.4A) All three patterns closely match that of cubic Cu_2Se with a lattice parameter matching the bulk value of a = 5.85 Å. The notable differences going from 6 nm to 2 nm Cu_2Se include: (1) the intensity of the {200} peak ($2\theta = 30.5^o$) relative to the {111} peak ($2\theta = 26.4^o$) increases, and (2) the intensity of the {311} peak ($2\theta = 51.8^o$) decreases.

We performed a series of XRD simulations using the program PowderCell which generates a PXRD pattern based on a structure factor calculation from unit cell parameters. (Fig. 3.4B) As a result, we generated model lattice structures for 2 nm, 4 nm, and 6 nm Cu_2Se that match the experimental XRD patterns well. Since there is a relatively small change in the selenium sub-lattice during the LT β-Cu_2Se to the HT α-Cu_2Se phase transition, our model structures retain a cubic *fcc* Se sub-lattice rather than a distorted cubic sub-lattice but the atomic positions of the Cu ion sub-lattice have been adjusted so that the calculated XRD patterns match experimental patterns. We found that the XRD pattern we obtained experimentally for 6 nm Cu_2Se matched the simulated XRD pattern proposed for LT β-Cu_2Se in which the majority of Cu ions (~5 ions) occupy trigonal positions and the remaining Cu ions (~3 ions) occupy tetrahedral positions.[13] For the 4 nm NCs, an increase in the intensity of the {200} peak relative to the {111} peak is observed. We found that this strongly correlates with an increasing occupancy of Cu^+ ions in tetrahedral positions. (Fig. 3.4C) We found that the best match from out simulated XRD patterns came from the anti-fluorite structure in which all *8c* tetrahedral lattice sites are occupied by Cu ions and no *32f* trigonal positions are occupied. Also observed is a clear broadening of the {200} peak relative to the {111} peak in both 4 nm NCs and 2 nm clusters. In superionic phase of ionic solids like Cu^+ and Ag+ chalcogenides, peaks associated with Ag-Ag distances or Cu-Cu distances often broaden as a result of mixing of interatomic distances in the mobile cationic lattice.[25,26] Peaks arising from Cu-Cu interatomic distances along the {100} plane, such as the {200} reflection, are likely to be broad relative to the {111} reflection. Furthermore, broadening of the {220} peak in Cu_2Se has been strongly correlated with the superionic phase.[25,21] While the peak position of the {220} peak remains constant in all three size NCs, there is a clear asymmetric broadening of the peak for Cu_2Se clusters, similar to that observed in total scattering measurements for superionic Cu_2Se.[25]

We found that the XRD pattern for 2 nm clusters could not be reproduced using only *8c* tetrahedral and *32f* trigonal lattice sites. The 2 nm cluster pattern, in which the {111} and {200} peaks are nearly equivalent in intensity, requires some occupation of the *4b* octahedral positions. (Fig. 3.4D) In addition, rather than interstitial trigonal positions, we found that the *24e* interstitial positions were occupied. (Scheme of all Cu

positions in Fig. 3.4) Some occupation of *4b* octahedral positions in the HT α-Cu_2Se phase has been suggested by x-ray and neutron diffraction studies, whereas occupation of octahedral positions in the LT β-Cu_2Se is unlikely due to high Cu-Cu ion repulsion energy. In general, as the temperature is raised further above the phase transition temperature in HT α-Cu_2Se, the Cu ion density broadens away from the tetrahedral sites.[27]

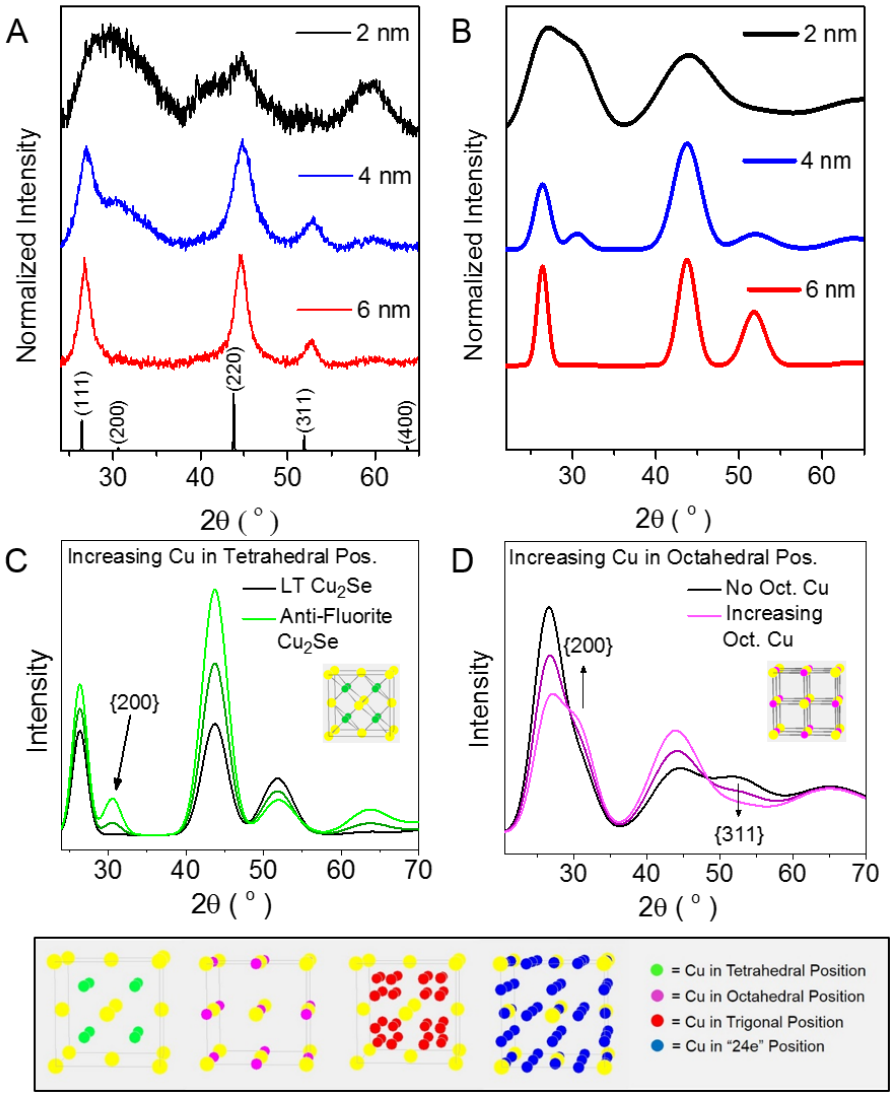

Figure 3.4 Experimental and calculated X-ray diffraction of 2 nm, 4 nm, and 6 nm Cu_2Se nanocrystals. *Experimental PXRD patterns of 2 nm, 4 nm, and 6 nm NCs are shown in 4A. The experimental pattern for 6 nm cubic Cu_2Se matches the calculated LT-Cu_2Se phase determined from literature.*[13] *In the experimental pattern for 4 nm cubic Cu_2Se, the {200} reflection is present. In 4C, starting from the LT-Cu_2Se phase (black pattern), the series of calculated XRD patterns shows that the result of removing Cu^+ ions from trigonal positions and placing them in tetrahedral positions is an increase in the {200} reflection. In 4D, starting from a phase in which all Cu^+ atoms are in tetrahedral and 24E positions (black pattern), the series shows the result of removing Cu^+ ions from 24E positions and placing more Cu^+ ions in octahedral positions.*

Table 3.2 *Parameters for Calculated Diffraction Patterns in Fig. 3.4B.*

6 nm – Cu_2Se				Space Group: *Fm-3m*, *a* = 5.85 Å	
Element	**Wycoff Pos.**	**x**	**y**	**z**	**Occ.**
Se	4a	0	0	0	1
Cu	8c	0.25	0.25	0.25	0.37
Cu	32f	0.34	0.34	0.34	0.1575
4 nm – Cu_2Se				Space Group: *Fm-3m*, *a* = 5.85 Å	
Element	**Wycoff Pos.**	**x**	**y**	**z**	**Occ.**
Se	4a	0	0	0	1
Cu	8c	0.25	0.25	0.25	1
2 nm – Cu_2Se				Space Group: *Fm-3m*, *a* = 5.85 Å	
Element	**Wycoff Pos.**	**x**	**y**	**z**	**Occ.**
Se	4a	0	0	0	1
Cu	8c	0.25	0.25	0.25	0.3
Cu	4b	0.5	0.5	0.5	0.3
Cu	24e	0.25	0	0	0.183

Table 3.3 *Parameters for Calculated Diffraction Patterns in Fig. 3.4C.*

4 nm – Cu_2Se				Space Group: *Fm-3m*, *a* = 5.85 Å	
Element	**Wycoff Pos.**	**x**	**y**	**z**	**Occ.**
Se	4a	0	0	0	1
Cu	8c	0.25	0.25	0.25	0.37
Cu	32f	0.34	0.34	0.34	0.1575
4 nm – Cu_2Se				Space Group: *Fm-3m*, *a* = 5.85 Å	
Element	**Wycoff Pos.**	**x**	**y**	**z**	**Occ.**
Se	4a	0	0	0	1
Cu	8c	0.25	0.25	0.25	0.685
Cu	32f	0.34	0.34	0.34	0.07875
4 nm – Cu_2Se				Space Group: *Fm-3m*, *a* = 5.85 Å	
Element	**Wycoff Pos.**	**x**	**y**	**z**	**Occ.**
Se	4a	0	0	0	1
Cu	8c	0.25	0.25	0.25	1
Cu	32f	0.34	0.34	0.34	0

Table 3.4 *Parameters for Calculated Diffraction Patterns for Fig. 3.4D.*

2 nm – Cu_2Se				Space Group: *Fm-3m*, a = 5.85 Å	
Element	**Wycoff Pos.**	**x**	**y**	**z**	**Occ.**
Se	4a	0	0	0	1
Cu	8c	0.25	0.25	0.25	0.3
Cu	4b	0.5	0.5	0.5	0
Cu	24e	0.25	0	0	0.2333
2 nm – Cu_2Se				Space Group: *Fm-3m*, a = 5.85 Å	
Element	**Wycoff Pos.**	**x**	**y**	**z**	**Occ.**
Se	4a	0	0	0	1
Cu	8c	0.25	0.25	0.25	0.3
Cu	4b	0.5	0.5	0.5	0.15
Cu	24e	0.25	0	0	0.2083
2 nm – Cu_2Se				Space Group: *Fm-3m*, a = 5.85 Å	
Element	**Wycoff Pos.**	**x**	**y**	**z**	**Occ.**
Se	4a	0	0	0	1
Cu	8c	0.25	0.25	0.25	0.3
Cu	4b	0.5	0.5	0.5	0.3
Cu	24e	0.25	0	0	0.1833

3.4 Discussion

The similarity in optical behavior between Cu_2Se clusters and NCs upon electronic doping (Fig. 3.2) verifies that, despite being ultrasmall clusters that are predominantly comprised of surface atoms, Cu_2Se clusters preserve the hallmark materials properties of $Cu_{2-x}Se$. The similarity in LSPRs of ultrasmall clusters and larger NCs suggests that Cu_2Se clusters are capable of supporting the same Cu vacancy concentration, and hence hole density, as larger NCs. The small difference in LSPR maxima, a 0.07 eV shift or a 7% increase in the plasma frequency, ω_p, indicates a carrier density increase of, at most, 14%, or a change in stoichiometry of $Cu_{1.85}Se$ to $Cu_{1.83}Se$ between Cu_2Se clusters and NCs. This finding also contradicts the notion that a large number of charge carriers are necessary to produce a collective resonance and, in fact, a collective resonance can be seen in ultrasmall clusters with a similar carrier density, but only a few charge carriers.[28] As shown in larger CdS nanorods[29], oxidation and reduction reactions can lead to changes in the free carrier density of ultrasmall Cu_2Se clusters. In fact, ultrasmall clusters are likely much more sensitive probes capable of detecting single electron or ion transfer events. Doped semiconductors, like the copper chalcogenides reported here (1) have free carrier densities that can be tuned through redox chemistry and (2) support collective LSPR resonances with much fewer mobile carriers than metals: two properties that allow a high degree of chemical control over the step-by-step build-up of a collective plasmonic resonance

as observed by optical absorption studies. Ultrasmall Cu_2Se clusters could be the ideal platform for probing the intermediate state between single electron intraband excitations and collective free carrier resonances.[28]

Size-dependent depression of the phase transition temperature for high-temperature superionic materials like Cu_2S, AgI and Ag_2Se has been reported previously.[4,6,30] Although the presence of a superionic phase is often verified using ionic or electronic transport measurements, this can be unfeasible when probing ultrasmall clusters on the order of 2 nm in diameter. Instead, electron microscopy and x-ray diffraction offer insight into the structure of the cationic sub-lattice and the dominant crystal phase as a function of crystallite size. In Fig. 3.3 and Fig. 3.7, 3.8, and 3.9, HRTEM images of Cu_2Se nanocrystals show a distinct decrease in the presence of vacancy ordering as the crystallite size is decreased from 6 nm to 2 nm. Previous studies show that vacancy ordering, viewed via TEM images as a lattice fringe contrast pattern with a periodicity of 0.67 nm, is a strong indication of the presence of the LT β-Cu_2Se phase.[12,13,24] Liu et al. showed that in bulk Cu_2Se, this superstructure contrast pattern was observed in HR-TEM at ambient temperature signifying the LT β-Cu_2Se phase. Upon heating to 150 ^oC, above the HT α-Cu_2Se phase transition temperature, the superstructure pattern was replaced by a pattern corresponding to the typical {111} d-spacing of 0.32 nm. The complete absence of vacancy-ordered superstructure in the 2 nm clusters suggests that the critical temperature of phase transition from the LT β-Cu_2Se phase to the HT α-Cu_2Se phase is depressed in small clusters to below room temperature.

Experimental XRD patterns obtained from 6 nm Cu_2Se NCs also provide strong evidence of the absence of the symmetric anti-fluorite structure associated with the superionic HT α-Cu_2Se phase. In the LT β-Cu_2Se phase, Cu ions localize at specific sites in the lattice. A high population of Cu ions on either of the symmetric sites associated with high Cu mobility, tetrahedral or octahedral sites, would result in the presence of a {200} reflection present in the XRD. Instead, the {200} peak is absent, signifying that most Cu ions are localized at the interstitial trigonal sites. Comparison of the experimental XRD pattern with a simulated pattern shows that it matches a structure in which a majority of the Cu^+ ions are at lower energy trigonal positions associated with the LT β-Cu_2Se phase. It should be noted that several studies observe a peak in the XRD pattern of the bulk LT β-Cu_2Se phase at $2\theta \approx 40^o$, which is correlated with the lowering of the lattice symmetry upon cooling to the LT β-Cu_2Se phase.[12,13] We do not observe a peak at $2\theta \approx 40^o$ in any of our diffraction patterns, which could be a result of slight differences in the periodicity of the lattice asymmetry in 2-6 nm nanocrystals as compared to the bulk.

XRD patterns from the intermediate-sized 4 nm NCs provide strong evidence that, with decreasing crystallite size, the population of Cu ions occupying tetrahedral sites increases. This fits well with the smaller portion of 4 nm NCs displaying tetrahedral vacancy ordering via HRTEM. As crystallite size decreases to the size of a few lattice units, determining periodic structure through electron microscopy

lattice fringes and x-ray diffraction becomes more challenging. Scherrer broadening and surface reconstruction can shift and broaden diffraction peaks and Fourier transforms of lattice fringes. From an analysis of the 2 nm XRD patterns, we find a higher ratio of the {200} peak intensity to the {111} peak intensity compared to 4 and 6 nm samples, which suggests that the Cu^+ occupancy of the octahedral positions is higher in the 2 nm NC. An increase in the Cu ion occupancy of the tetrahedral, and possibly octahedral, lattice sites is consistent with the presence of a disordered superionic structure, wherein Cu migration takes place via hopping between tetrahedral sites through intermediary octahedral sites. Typically a high cationic occupancy of tetrahedral positions leads to repulsion between Cu ions making these higher energy positions. This is more dramatic for octahedral positions which have an even higher Cu-Cu repulsion energy.[31] The exact physical reason for the stabilization of octahedral Cu atoms in 2 nm Cu_2Se is lacking, but a number of effects, in particular compressive lattice strain in the 2-nm NCs may be responsible. A density functional theory (DFT) based investigation of the electronic origin of this effect is currently underway in the Jain lab.

3.5 Conclusion

In summary, cation exchange is a useful synthetic technique for accessing materials in a new size regime. Through cation exchange of CdSe clusters, we are able to synthesize and isolate ultrasmall, 2 nm Cu_2Se clusters. Through comparison of the optical and structural properties of ultrasmall Cu_2Se clusters to larger Cu_2Se nanocrystals (NCs) made though a similar synthetic method, we have discovered that crystallographic structures are affected by a decrease in crystallite size. Notably, we have found that the crystal phase of ultrasmall Cu_2Se more closely resembles that of the superionic HT α-Cu_2Se phase rather than the LT β-Cu_2Se phase at ambient temperature, suggesting that the phase transition temperature is depressed to below room temperature in this ultrasmall size regime. The ability to use crystallite size to tune the atomic structure, and hence ionic conduction, of Cu_2Se could allow for the development nanostructured Cu_2Se superionic materials for applications like solid-state electrolytes for energy storage devices and ionic switches.

3.6 Methods

Synthesis of 2 nm CdSe clusters. The procedure for the synthesis of CdSe clusters was adapted from Yu, K. et al.[19] Cadmium acetate (0.20 mmol, 53.3 mg) and oleic acid (0.13 mmol, 41 μL) were added to a 25 mL three-neck flask. The flask was repeatedly purged with Ar to remove O_2. Under argon, 5 g of TOP was

added to the flask via syringe and the solution was heated to 120 °C, and exposed to vacuum for 45 min. Then, the flask was exposed to argon, the temperature was dropped to 100 °C and a TOP-Se solution (0.05 mmol (4 mg) of selenium powder) in 0.4 mL of TOP) was added to the flask. The temperature was raised to 120 °C and the reaction was allowed to proceed for 60 min. The solution was a light yellow color. After synthesis, the clusters were washed repeatedly with toluene and methanol and dispersed in toluene.

Synthesis of 4 nm CdSe NCs (zincblende). The procedure for synthesis of 4 nm CdSe NCs was adapted from Yang, et al.[32] Cadmium myristate (192 mg, 0.34 mmol) was added to a flask with 3.4g octadecene (ODE) (4.3mL), which was heated to 140 °C under argon. The solution was cooled to 100 °C and put under vacuum for 30 min. The solution was then put under Ar and cooled to room temperature. A solution of TOPSe was prepared in a glove box by dissolving 0.17 mg of Se (0.17 mmol) in 126 mg of TOP (0.34 mmol). The TOPSe was injected into the reaction flask. The temperature was raised to 210 °C (~9min). After reaching 210 °C, oleic acid in ODE (48mg in 0.5mL) was injected into the flask to stabilize growth. Then the reaction proceeded at 210 °C for 50min. After synthesis, the NCs were washed repeatedly with toluene and methanol and dispersed in toluene.

Synthesis of 6 nm CdSe NCs (wurtzite). The procedure for synthesis of 4 nm CdSe NCs was adapted from Carbone *et al*.[33] Cadmium Oxide (0.06 g), Octadecylphosphonic acid (0.28 g), and TOPO (3.0 g) were added to a 50 ml three-neck round-bottom flask. The flask was degassed under vacuum at 150 °C for 1.5 h. The flask was then put under Ar and the temperature was gradually increased to 300 °C over the course of 2 h. While slowly ramping the temperature up to 320 °C, the solution becomes optically clear. After reaching 320 °C, 1.8 mL of TOP was slowly injected into the mixture. A solution of TOPSe was prepared in a glove-box by dissolving 0.6 g Se in 4.48 ml TOP and stirred at room temperature overnight. The temperature of the mixture in the flask was raised to 360 °C and 0.45 mL of the TOPSe solution was injected rapidly. After injection, the solution is heated at 360 °C for 70 sec, or until the solution is a dark red color, after which the heating mantle was removed. The nanocrystals were washed repeatedly with toluene and methanol and dispersed in toluene.

Synthesis of 6 nm CdSe NCs (zincblende). The procedure for synthesis of 6 nm CdSe NCs was adapted from Liu, et al.[34] 78.4 mg of Se and 15 mL of ODE were added to 50mL 3-arm RB flask. The RBF was heated to 100 °C and put under vacuum for 30 min. At the same time 266 mg of Cd(Ac)2 was added to 25mL RBF with 5mL of oleic acid and heated to 100 °C and put under vacuum for 30 min. Both flasks were put under Ar again. The flask with Cd was heated to 150 °C and the flask with Se was heated to 280 °C for 30 min. The Se solution turned yellow indicating SeODE complex. Then the solution of Cd was quickly added to the other flask and the temperature was brought to 275 °C and proceeded for 40 min. After synthesis, the NCs were washed repeatedly with hexanes and ethanol and redispersed in toluene.

Ligand Exchange with octylamine. For 4 nm and 6 nm CdSe NCs, it was found that an initial ligand exchange with octylamine increased colloidal stability of Cu_2Se NCs after cation exchange. Before cation exchange, solutions of 4 nm and 6 nm CdSe NCs dispersed in toluene was mixed with ~0.5 mL of octylamine, after which the NCs were washed with methanol and redispersed in toluene.

Exchange with Cu^+. All exchange procedures were carried out in an oxygen-free, moisture-free glove box. CdSe clusters were dispersed in toluene. A solution of tetrakis(acetonitrile) copper(I) hexafluorophosphate ($[(CH_3CN)_4Cu]PF_6$) in a methanolic solution (10% methanol in acetonitrile by volume) was then added dropwise to the solution. Solutions were stirred vigorously after each addition. Exchange was monitored by UV-Vis absorption spectroscopy. In exchange reactions with 2 nm Cu_2Se clusters, 1.5 equivalents of trioctylphosphine was added to the methanolic solution for each equivalent of $[(CH_3CN)_4Cu]PF_6$ to form TOP-Cu. This improved the colloidal stability of exchanged Cu_2Se clusters.

Double Exchange with Cd^{2+}. For double-exchange of CdSe clusters, an initial ligand-exchange with octylamine was performed. 1 mL of octylamine was added to the CdSe cluster solution after synthesis. The solution immediately turns from a semi-opaque to a transparent yellow color. The amine-capped clusters were washed repeatedly with chloroform and methanol and dispersed in chloroform. UV-vis characterization of amine-capped clusters reveals a shift of the excitonic absorption from 406 nm before ligand exchange to 415 nm after ligand exchange. A solution of tetrakis(acetonitrile) copper(I) hexafluorophosphate ($[(CH_3CN)_4Cu]PF_6$) in methanol was then added dropwise to the solution. Solutions were stirred vigorously after each addition. Exchange was monitored by UV-Vis absorption spectroscopy. Double exchange was carried out without cleaning. A solution of cadmium nitrate tetrahydrate in methanol with 50 μL of tributylphosphine was then added to the solution of Cu_2Se clusters. To improve colloidal stability of the clusters during exchange, 40 μL of octylamine and 40 μL of oleic acid were added. Exchange with Cd^{2+} was monitored via UV-vis absorption spectroscopy and took ~2 hours.

Oxidation of Cu_2Se clusters. After cation exchange with the Cu^+, a small amount (50 microliters) of oleic acid was added to both the 2 nm and the 6 nm solutions for improving the colloidal stability of the NCs. The samples were then washed with methanol and dispersed in toluene and sonicated for 20 minutes. Spectra were taken at regular intervals of 1 hour at the beginning of the onset of the oxidation using NIR cuvettes from Spectrocell, but later on the spectra were taken with larger intervals. The absorption was measured over a range of 300-2000 nm, and the region where the toluene absorption occurs were taken out by hand. Each time the sample was sonicated before taking any spectra, and about an aliquot of the sample was used every time so that any changes affecting the level of the solvent due to slight evaporation overnight was replenished carefully with toluene taken from the glovebox.

Reduction of Cu_2Se clusters. The reduction reaction with cobaltocene solution was carried out in the wavelength range of 300-2000 nm. The range was put to 300-2000 nm, and the region where the toluene absorption occurs, i.e., ~1633-1740 nm were taken out by hand. About 51 mg of cobaltocene was mixed with 4 ml of toluene in the glovebox. The reduction was carried out inside the glovebox so as to prevent the effect of unwanted oxidation as cobaltocene is a very strong reducing agent and reacts very efficiently with oxygen. For this purpose, 3.5 ml of the solution was taken in a NIR cuvette from Spectrocell, and the lid was tightly closed. Additional carbon tape was used to prevent air exposure. The additions were made in increments of 5 μLs inside the glovebox. After every addition, the solution was allowed to stir for 40 minutes before taking it out of the glovebox carefully and quickly and taking a spectra in the range of 300-2000 nm. The solution was replaced in the glovebox quickly afterwards.

***Electron microscopy*.** High resolution transmission electron microscopy (HRTEM) and high-angle annular dark field scanning transmission electron microscopy (HAADF-STEM) images were acquired on a JEOL 2010F operating at 200 kV. Samples were prepared by drop casting NCs in toluene on an ultrathin carbon grid followed by repeated washing with methanol. Size analysis of each sample was done using HAADF-STEM images. Analysis of superstructure in each NC sample was done using HRTEM images.

X-Ray diffraction. PXRD patterns were collected on a Rigaku Miniflex 600 powder x-ray diffraction system operated at full power (40kV - 15 mA) with Cu K alpha radiation wavelength. Data was collected in reflection mode from $2\theta = 15^o$ to $2\theta = 65^o$ using step-wise scans of 0.04^o with scans running for 2-3 hrs. Samples were drop-cast as a thick layer on a zero-background quartz slide.

Calculated X-ray diffraction. Calculated powder diffraction patterns were generated using the program PowderCell, which generates a powder pattern based on a structure factor calculation from lattice parameters and atomic positions. The calculated powder patterns also reflect peak broadening due to crystallite size (here assumed to be either 2 nm, 4 nm, or 6 nm). Input parameters for each pattern are given in Tables 3.1, 3.2, and 3.3.

3.7 Additional figures

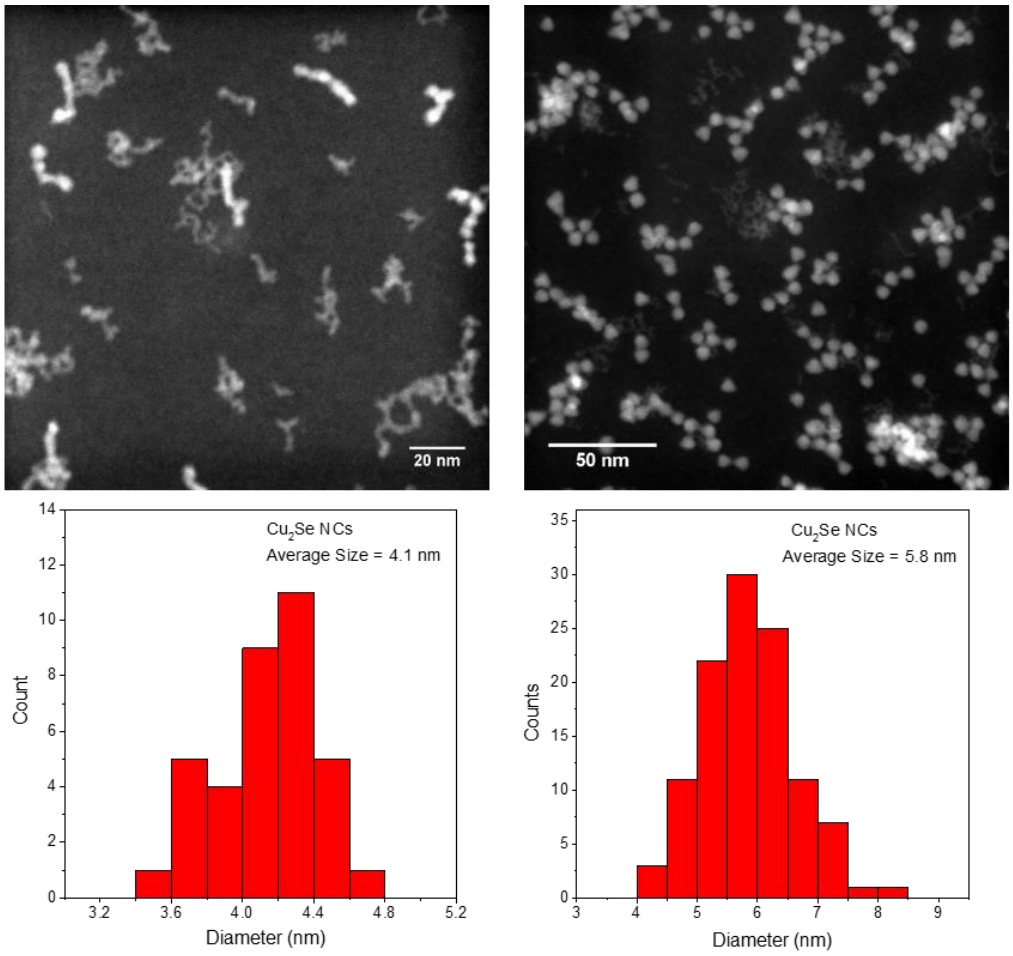

Figure 3.5 *High-angle annular dark field scanning electron transmission microscopy (HAADF-STEM) of 4 nm and 6 nm Cu_2Se nanocrystals (NCs). Top panel shows representative HAADF-STEM images for 4 nm and 6 nm NCs obtained from cation exchange. NC sizes were estimated manually in Image J from STEM images. The diameter of the quasi-spherical NC domains was measured using the line tool. Data from ca. 40 NC domains was used to make the size histograms shown in the bottom panel and to determine average diameters. Samples were prepared by titrating solutions of 4 nm and 6 nm zincblende CdSe nanocrystals in toluene with a methanolic solution of Cu^+, as described in Section 3.6. Exchange to Cu_2Se was monitored via UV-Vis absorption spectroscopy. Fully exchanged samples were precipitated with methanol, dispersed in toluene, drop-cast onto an ultrathin carbon TEM grid, and washed with methanol several times. HAADF-STEM images were acquired on a JEOL 2010F at 200 kV with a 0.5-nm size beam.*

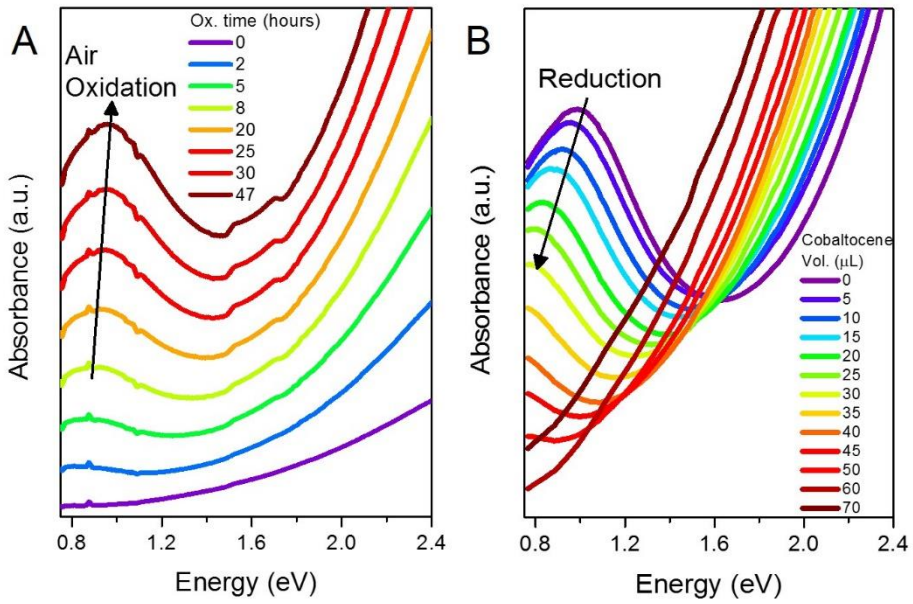

Figure 3.6 *A) UV-vis absorption spectra of 6 nm Cu_2Se NCs in the course of oxidation in air. Air oxidation results in the removal of Cu in the form of copper oxide, leading to formation of holes in the valence band. Hole formation is manifested in the emergence of a localized surface plasmon resonance (LSPR) band. With increasing oxidation time, the LSPR band blue-shifts, signifying an increase in the hole density. The peak energy of the LSPR eventually stabilizes to a value of 0.99 eV. B) UV-vis absorption spectra of the oxidized 6 nm Cu_2Se NCs in the course of titration with a solution of the reducing agent cobaltocene. Cobaltocene injects electrons into the NCs annihilating the holes in the valence band. As a result, the LSPR redshifts and decreases in intensity, signifying a decrease in the hole density. The 6 nm Cu_2Se NCs were prepared by the cation exchange of 6 nm wurtzite CdSe NCs.*

Figure 3.7 *HRTEM images of several more 2 nm Cu_2Se clusters. Measured lattice spacings between {111} planes are shown for many of the clusters in the wide-field images.*

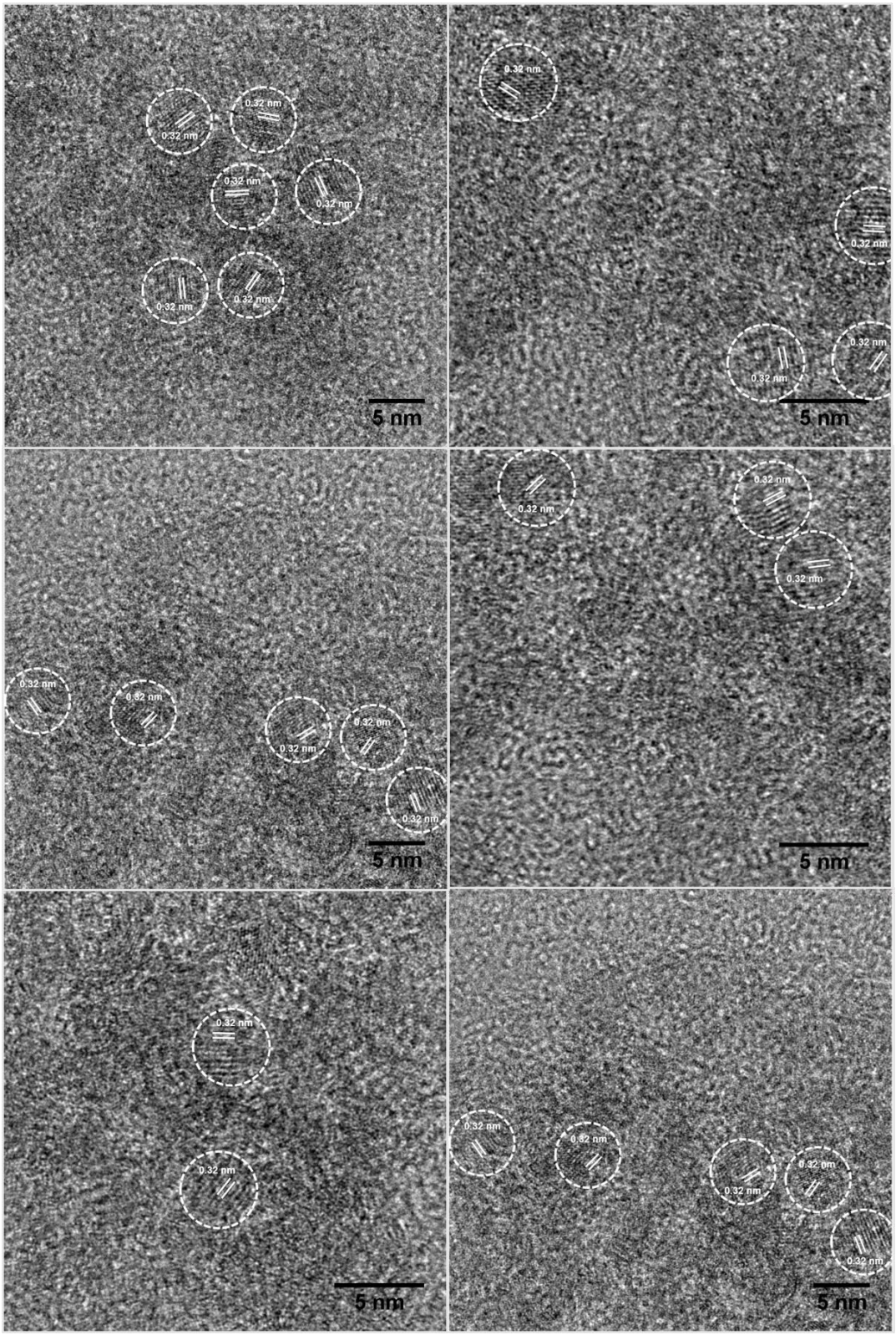

Figure 3.7 *continued.*

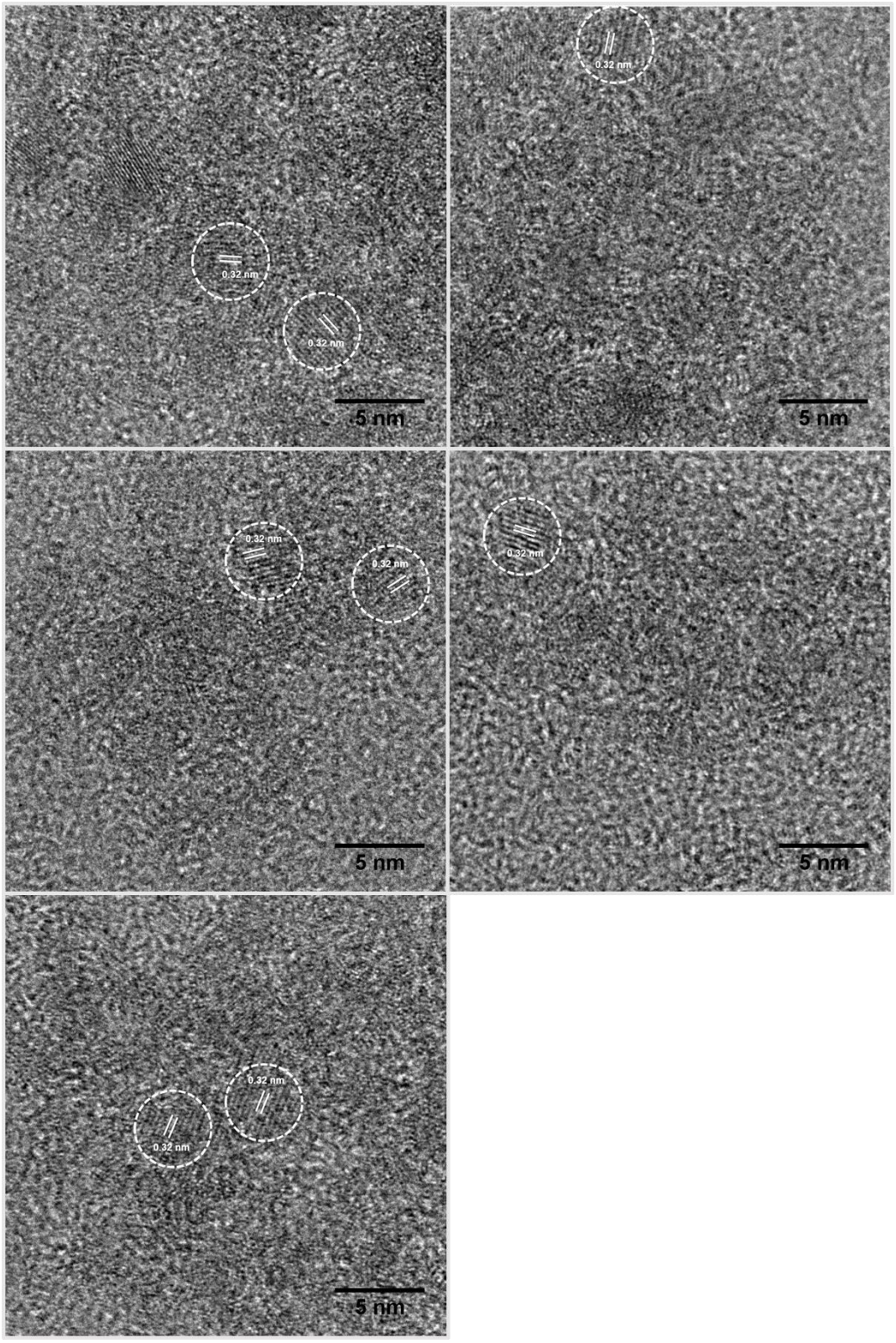

Figure 3.8 *HRTEM images of several more 4 nm Cu_2Se NCs. Measured lattice spacings between {111} planes are shown for many of the NCs in the wide-field images.*

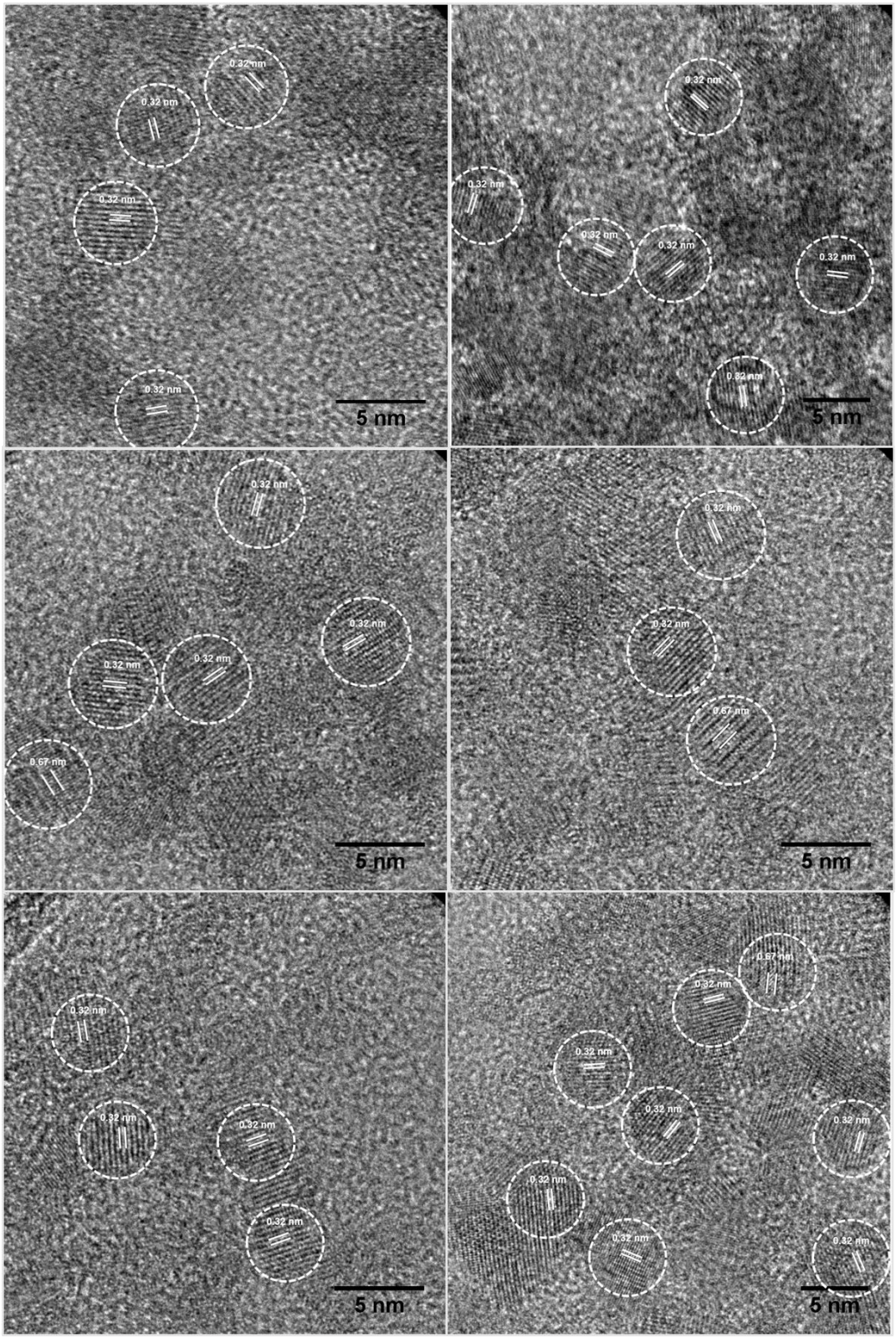

Figure 3.9 *HRTEM images of several more 6 nm Cu_2Se NCs. Measured lattice spacings between {111} planes are shown for all NCs. Scale bar shown corresponds to 5 nm.*

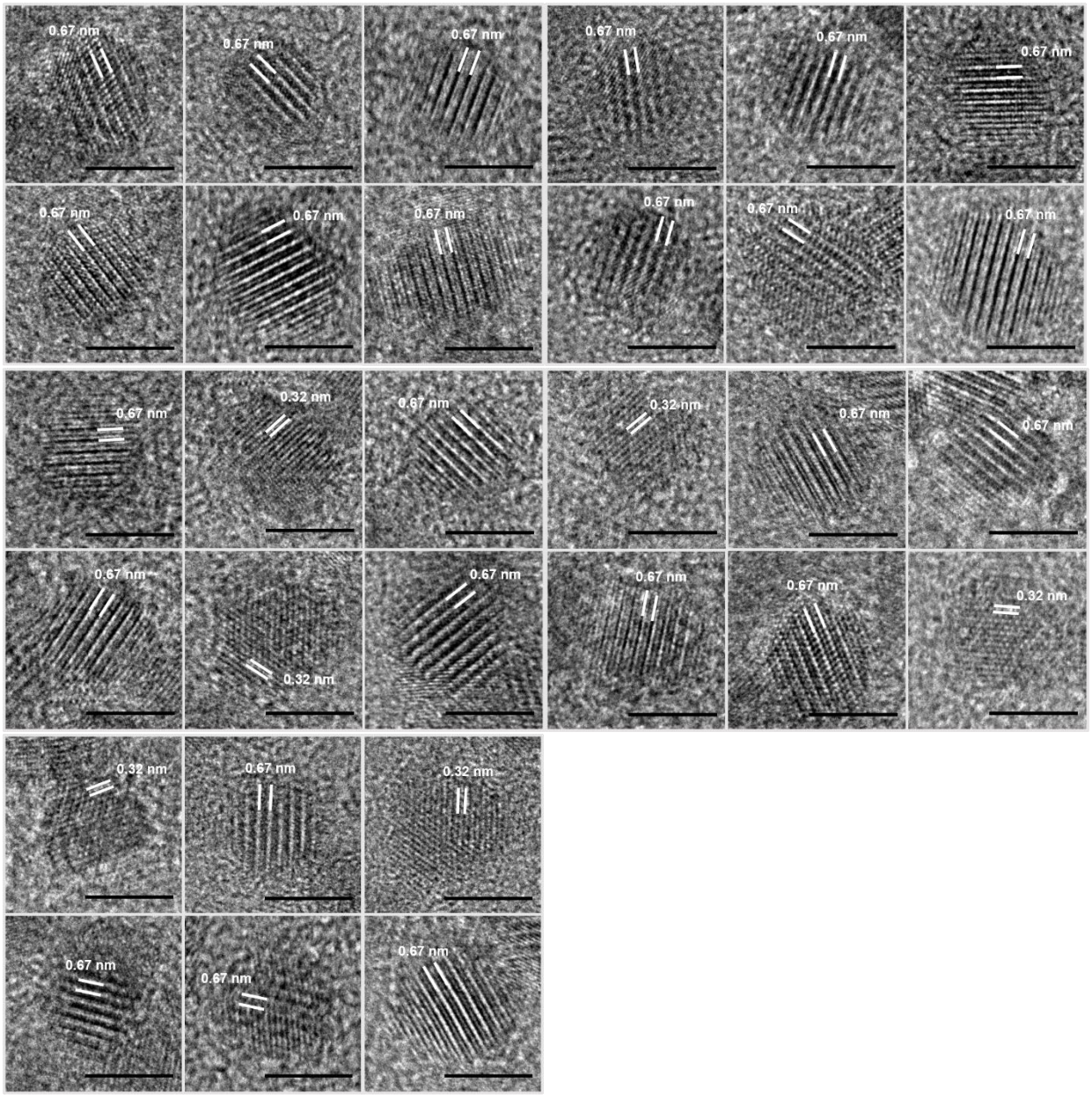

3.8 References

1. Scholl, J. a, Koh, A. L. & Dionne, J. a. Quantum plasmon resonances of individual metallic nanoparticles. *Nature* **483,** 421–7 (2012).

2. A. P. Alivisatos. Semiconductor Cluster, Nanocrystals, and Quantum Dots. *Science* **271,** 933-937 (1996).

3. Tolbert, S. H. & Alivisatos, a P. Size Dependence of a First Order Solid-Solid Phase Transition: The Wurtzite to Rock Salt Transformation in CdSe Nanocrystals. *Science* **265,** 373–376 (1994).

4. Makiura, R. *et al.* Size-controlled stabilization of the superionic phase to room temperature in polymer-coated AgI nanoparticles. *Nat. Mater.* **8,** 476–480 (2009).

5. Buffat, P. & Borel, J. P. Size effect on the melting temperature of gold particles. *Phys. Rev. A* **13,** 2287–2298 (1976).

6. Rivest, J. B., Fong, L.-K., Jain, P. K., Toney, M. F. & Alivisatos, a. P. Size Dependence of a Temperature-Induced Solid–Solid Phase Transition in Copper(I) Sulfide. *J. Phys. Chem. Lett.* **2,** 2402–2406 (2011).

7. Maier, J. Nanoionics: ion transport and electrochemical storage in confined systems. *Nat. Mater.* **4,** 805–815 (2005).

8. Lee, J.-S., Adams, S. & Maier, J. Transport and Phase Transition Characteristics in AgI:Al[sub 2]O[sub 3] Composite Electrolytes Evidence for a Highly Conducting 7-Layer AgI Polytype. *J. Electrochem. Soc.* **147,** 2407 (2000).

9. Rivest, J. B. & Jain, P. K. Cation exchange on the nanoscale: an emerging technique for new material synthesis, device fabrication, and chemical sensing. *Chem. Soc. Rev.* 89–96 (2013).

10. Luther, J. M., Jain, P. K., Ewers, T. & Alivisatos, A. P. Localized surface plasmon resonances arising from free carriers in doped quantum dots. *Nat. Mater.* **10,** 361–6 (2011).

11. Routzahn, A. L., White, S. L., Fong, L. K. & Jain, P. K. Plasmonics with doped quantum dots. *Israel Journal of Chemistry* **52,** 983–991 (2012).

12. Liu, H. *et al.* Copper ion liquid-like thermoelectrics. *Nat. Mater.* **11,** 422–425 (2012).

13. Kashida, S. & Akai, J. X-ray diffraction and electron microscopy studies of the room-temperature structure of Cu_2Se. *J. Phys. C Solid State Phys.* **21,** 5329–5336 (1988).

14. Endo, H., Yao, M. & Ishida, K. Ionic conductivity and electronic properties of liquid Ag chalcogenides up to 1500 degrees C. *J. Phys. Soc. Japan* **48,** 235–237 (1980).

15. Rice, M. J., Strässler, S. & Toombs, G. A. Superionic conductors: Theory of the phase transition to the cation disordered state. *Phys. Rev. Lett.* **32,** 596–599 (1974).

16. Terabe, K., Hasegawa, T., Nakayama, T. & Aono, M. Quantized conductance atomic switch. *Nature* **433,** 47–50 (2005).

17. Kasuya, A. *et al.* Ultra-stable nanoparticles of CdSe revealed from mass spectrometry. *Nat. Mater.* **3,** 99–102 (2004).

18. Beecher, A. N. *et al.* Atomic structures and gram scale synthesis of three tetrahedral quantum dots. *J. Am. Chem. Soc.* **136,** 10645–10653 (2014).

19. Yu, K. *et al.* Thermodynamic equilibrium-driven formation of single-sized nanocrystals: Reaction

media tuning CdSe magic-sized versus regular quantum dots. *J. Phys. Chem. C* **114,** 3329–3339 (2010).

20. Danilkin, S. A. *et al.* Crystal structure and lattice dynamics of superionic copper selenide $Cu_{2-x}Se$. *J. Alloys Compd.* **361,** 57–61 (2003).

21. Danilkin, S. A. *et al.* Neutron scattering study of short-range correlations and ionic diffusion in copper selenide. *Ionics (Kiel).* **17,** 75–80 (2011).

22. Yamamoto, K. & Kashida, S. X-ray study of the average structures of Cu_2Se and $Cu_{1.8}S$ in the room temperature and the high temperature phases. *J. Solid State Chem.* **93,** 202–211 (1991).

23. Vučić, Z., Milat, O., Horvatić, V. & Ogorelec, Z. Composition-induced phase-transition splitting in cuprous selenide. *Phys. Rev. B* **24,** 5398–5401 (1981).

24. Milat, O., Vučić, Z. & Ruščić, B. Superstructural ordering in low-temperature phase of superionic Cu_2Se. *Solid State Ionics* **23,** 37–47 (1987).

25. Brown, D. R. *et al.* Phase transition enhanced thermoelectric figure-of-merit in copper chalcogenides. *APL Mater.* **1,** (2013).

26. Blanton, T., Misture, S., Dontula, N. & Zdzieszynski, S. In situ high-temperature X-ray diffraction characterization of silver sulfide, Ag_2S. *Powder Diffr.* **26,** 114–118 (2012).

27. Boyce, J. B., Hayes, T. M., Mikkelsen, J. C. EXAFS investigation of mobile-ion density: CuI and Cu_2Se contrasted. *Solid State Ionics* **5,** 497–500 (1981).

28. Jain, P. K. Plasmon-in-a-Box: On the Physical Nature of Few-Carrier Plasmon Resonances. *J. Phys. Chem. Lett.* **5,** 3112–3119 (2014).

29. Jain, P. K. *et al.* Doped nanocrystals as plasmonic probes of redox chemistry. *Angew. Chemie - Int. Ed.* **52,** 13671–13675 (2013).

30. Hu, T., Wittenberg, J. S. & Lindenberg, a M. Room-temperature stabilization of nanoscale superionic Ag_2Se. *Nanotechnology* **25,** 415705 (2014).

31. Boyce, J. B., Hayes, T. M. & Mikkelsen, J. C. EXAFS investigation of mobile-ion density: Cul and Cu_2Se contrasted. *Solid State Ionics* **5,** 497–500 (1981).

32. Yang, Y. A., Wu, H., Williams, K. R. & Cao, Y. C. Synthesis of CdSe and CdTe nanocrystals without precursor injection. *Angew. Chemie - Int. Ed.* **44,** 6712–6715 (2005).

33. Carbone, L. *et al.* Synthesis and micrometer-scale assembly of colloidal CdSe/CdS nanorods prepared by a seeded growth approach. *Nano Lett.* **7,** 2942–2950 (2007).

34. Liu, L. *et al.* Shape control of CdSe nanocrystals with zinc blende structure. *J. Am. Chem. Soc.* **131,** 16423–16429 (2009).

Chapter 4: Regio-selective plasmonic coupling in metamolecular analogs of benzene derivatives*

4.1 Abstract

In analogy with benzene-derived molecular structures, we construct plasmonic metamolecules by attaching Au nanospheres to specific sites on a hexagonal Au nanoplate. We employ a ligand exchange strategy that allows regio-selective control of nanosphere attachment and study resulting structures using correlated electron microscopy/optical spectroscopy at the single-metamolecule level. We find that plasmonic coupling within the resulting assembly is strongly dependent on the structure of the metamolecule, in particular the site of attachment of the nanosphere/s. We also uncover a synergy in the polarizing effect of multiple nanospheres attached to the nanoplate. Regio-selective control of plasmonic properties demonstrated here enables the design of novel structure-dependent electromagnetic modes and applications in three-dimensional spatial nanosensors.

4.2 Introduction

Metal nanoparticles have received a lot of attention for their localized surface plasmon resonances (LSPR) for decades; in recent years, however, there has been an upsurge in the work on the construction of complex architectures composed of multiple plasmonic nanoparticles. The level of control and complexity in such assemblies has been constantly improving. The advances in this area can be thought of in the same vein as the synthesis of complex molecules from the chemical bonding of simpler atomic units. This loose analogy is not limited to aspects of the fabrication, but also to the emergence of new optical properties and function in complex architectures. For instance, when two metal nanoparticles are assembled, so as to be in close proximity, their dipolar plasmon oscillations couple via short-range near-fields, often producing new plasmonic modes, which can be of bonding or anti-bonding type, in analogy to concepts of molecular hybridization.[1–3] Dimers of plasmonic nanospheres (NSs),[4–6] nanoshells,[7,8] nanoprisms,[4] nanocubes,[9] and nanorods[1] and their hybrid plasmon modes have been studied. Bonding plasmon modes, characterized by strongly concentrated electric fields at the dimer junction,[4] have been exploited for optical sensing,[10–13]

* Reproduced with permission from: Fang, A.(co-first); White, S. L.(co-first); Jain, P. K.; Zamborini, F. P. Regio-selective plasmonic coupling in metamolecular analogs of benzene derivatives. *Nano Lett.* **15,** 542–548 (2015).

single-molecule detection by surface-enhanced Raman spectroscopy (SERS),[14–18] and wave-guiding of light.[19,20]

An added level of complexity has been achieved by means of heterodimers of plasmonic nanoparticles, i.e., dimers in which the two nanoparticles are dissimilar in size, shape, or composition. Heterodimers often display new coupling modes and unique spectral features that are not observed with homodimers,[21,22] including symmetry breaking, appearance of otherwise dark out-of-phase hybrid modes, avoided crossing behavior, Fano resonances, and asymmetric scattering properties. More recently larger clusters of plasmonic nanoparticles[23] and multi-nanoparticle core-satellite nanostructures[24–29] have been fabricated and studied for their plasmonic coupling as well as unique optical and magnetic modes that arise from inter-nanoparticle interactions.

In this Letter, we describe a further advance in the addition of control and complexity to plasmonic architecture design by the construction of plasmonic metamolecules that resemble benzene-derived molecules. These novel assemblies are designed by the controlled attachment of Au NSs to specific sites on the surface of a larger hexagonal Au nanoplate (NP), where we take advantage of past work on ligand exchange reactions on Au surfaces.[30,31] We achieve control on both the site of NS attachment and the number of NSs attached. The optical properties of plasmonic metamolecules constructed in this manner are characterized by single-particle dark-field scattering spectroscopy. Plasmonic spectra are correlated to assembly morphologies on the level of individual metamolecules, so as to avoid the loss of useful structure/optical property relationships due to ensemble-averaging over a heterogeneous sample.

In these metamolecules, we find hitherto undescribed regio-selective behavior, whereby the plasmonic spectrum of a NP/NS assembly is strongly dependent on the site of NS attachment. NSs attached to vertices of the hexagonal NP couple most strongly to the NP, greatly perturbing its native LSPR response; whereas other sites are found to offer weaker electromagnetic coupling. The number of attached NSs and the relative arrangement of NSs are also found to influence the plasmonic response. In particular, a positive synergy is found in the polarizing effect of multiple NSs. In addition, asymmetric distributions of multiple NSs attached to the sides of the NP result in complex, broadened, multi-peaked spectra with large plasmonic shifts. Thus, we demonstrate, in analogy to the molecular realm, that structural complexity on the nanoscale leads to new properties. The kind of regio-selective control and behavior described here has utility for the discovery of new emergent optical properties and the design of three-dimensional spatial nanosensors.[23]

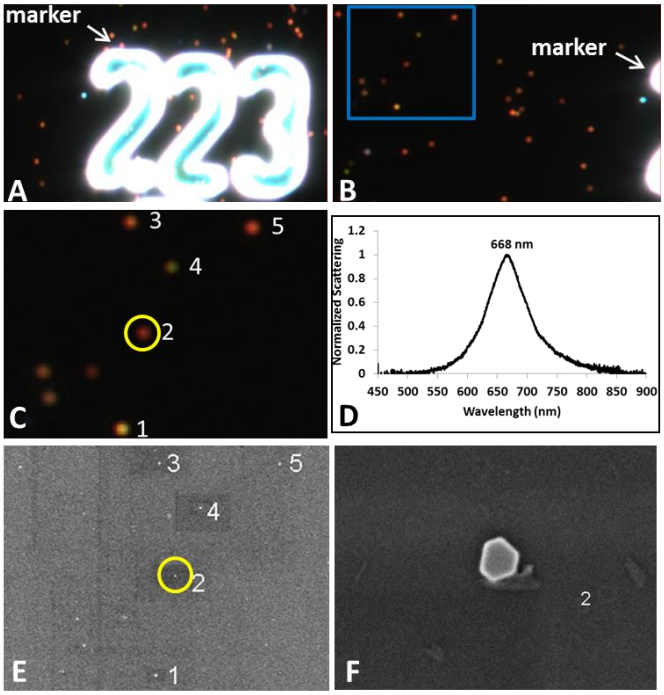

Figure 4.1 Correlated single-nanoparticle dark-field spectroscopy/ electron microscopy. *Dark-field microscopy image of Au NP scatterers on a glass slide in the region of an etched marker labeled '223' (A) and in a region directly to the left of the marker (B). The region marked by the blue rectangle in (B) is shown at a higher magnification in (C) with five NPs selected and numbered. The light-scattering spectrum of the Au NP labeled 2 is shown in (D). The spectrum shows a wavelength maximum, λ_{max}, of 668 nm. An SEM image of the same region as (C) is shown in (E). A higher magnification SEM image of the NP labeled 2 is shown in (F)*

4.3 Results and discussion

4.3.1 Attachment of Au NSs to Au NPs

The experimental strategy used for this study is shown in Fig. 4.1. We synthesized Au NPs directly on glass slides using a small modification of our previously described seed-mediated growth procedure.[31–33] This procedure helped us achieve an optimal density and size (~100 nm wide and 30 nm thick) of Au NPs, amenable to dark-field scattering spectroscopy at the single NP level. The glass slides contained etched numerical markers which were used to correlate dark-field scattering spectra of single NPs with scanning electron microscopy (SEM) images of the same NP. As shown in Fig. 4.1, we first obtained dark-field images of the sample near a number marker. We next obtained a dark-field scattering spectrum of 15-20 individual NPs identified in defined regions near the marker (Fig. 4.1C and 4.1D). After obtaining individual scattering spectra of each NP, we sputter-coated the glass sample with a thin 1-2 nm layer of Pt before obtaining SEM images. We confirmed that there were no changes in the NP shape due to Pt coating by comparing test Au NPs (synthesized on Si substrates) before and after the same Pt coating. Using SEM, the same NPs were identified (Fig. 4.1E) and high-resolution images were obtained for the determination of the size and morphology of each NP (Fig. 4.1F). In a few cases, we obtained AFM images directly after acquiring light-scattering spectra to determine the NP thickness. In cases where we attached NSs to NPs, we obtained light-scattering spectra of 15-20 NPs before and after NS attachment and obtained SEM images after the attachment.

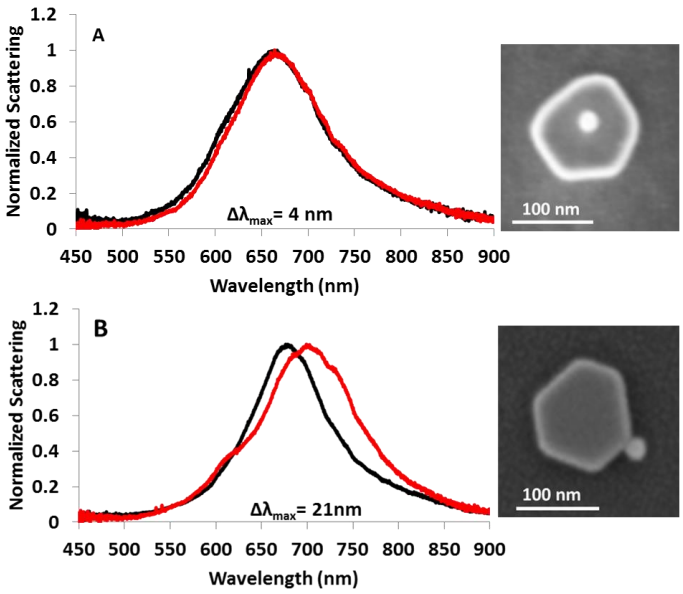

Figure 4.2 Terrace site vs. edge site attachment *(A) Scattering spectrum of a single Au NP before (black line) and after (red line) attachment of a 24-nm diameter Au NS on an inner terrace site of the NP, as shown in the SEM image to the right. (B) Scattering spectrum of a single Au NP before (black line) and after (red line) attachment of a 27-nm diameter Au NS on a vertex site, as shown in the SEM image to the right. The* λ_{max} *values were determined by fitting the spectra to single Lorentzian peaks. The shift in* λ_{max} *upon NS attachment is indicated.*

We attached 25 ± 3 nm diameter, citrate-coated Au NSs selectively to either the sides or the terrace sites of the Au NPs using thiol self-assembly and ligand place-exchange reactions,[30] described previously by our group.[31–33] For selective attachment to the sides, we first assembled on the Au NP surfaces hexanethiol (HT) ligands, which are inert to the Au NSs. The HT ligands were then place-exchanged with 4-aminothiophenol (4-ATP) ligands, which electrostatically bind the negatively-charged Au NSs through the terminal NH_3^+ groups at slightly acidic pH.[34] The pH value of the Au NS solution, maintained at 4.8 for all experiments, dictates the level of NH_2 protonation on 4-ATP and thereby influences NS attachment. A feature of the place-exchange is that 4-ATP ligands bind most preferentially to the vertices and edges of the hexagonal Au NPs, due to the lower steric hindrance at those locations. Consequently, there is selective attachment of Au NSs at vertices/side faces and negligible attachment at terrace locations.[30,31] For selective terrace site attachment, we performed the ligand modifications in reverse order. In this case, we first assembled 4-ATP ligands on the Au NP and then place-exchanged the 4-ATP with HT. The exchange occurs preferentially at the vertices and edges, leading to relative blocking of those regions from Au NS attachment and selective binding of NSs to the terrace sites. The full details of the process of selective Au NS attachment to Au NPs will be described in more detail elsewhere (unpublished results).

SEM images (Fig. 4.2) show the successful achievement of regio-selective attachment of NSs on the NP, which we exploited for studying the influence of the attachment site on the plasmonic response of the resulting metamolecule. We see a marked difference between the behaviors for attachment to terraces versus sides (Fig. 4.2). For instance, a representative single NP with an initial λ_{max} of 660 nm, upon attachment of an Au NS at a terrace site on the NP, shows a modest red-shift of its λ_{max} by 4 nm. A part of this shift (1-2 nm as indicated by control experiments without Au NSs) may simply be a result of an increase in the local refractive index caused by the binding of mixed HT/4-ATP monolayers. Thus, the Au NP has only weak, if any, plasmon coupling with a NS attached to the terrace. On the other hand, another Au NP with an initial λ_{max} of 678 nm shows a large 21-nm red-shift after the attachment of a NS to one of the vertices on the sides of the NP. This red-shift is indicative of strong plasmon coupling of a NP with a vertex-attached NS.

In order to confirm that this site-dependence of plasmon coupling is indeed statistically significant, we performed the same analysis on five other NPs with Au NSs attached to the terrace region and three other NPs with Au NSs attached to the vertices/side faces. The Au NS diameter ranged from 22-29 nm. The results are summarized in Tables 4.1 and 4.2, respectively. The red-shift in λ_{max} for terrace site attachment ranged from 2-4 nm with an average of 3 ± 1 nm. On the other hand, for vertex/side face attachment, the red-shift in λ_{max} ranged from 14-29 nm with an average of 22 ± 5 nm. The range in the magnitude of shift resulted most likely from heterogeneities like: (i) binding on different terrace sites (inner terrace vs. closer to an edge) or different sites on the sides (vertex vs. edge of a side face vs. center of a side face), (ii) differences in the Au NS diameter, or, (iii) differences in the original NP size and shape. Despite these heterogeneities, there is reproducibly an order-of-magnitude larger shift in λ_{max} for vertex/side face attachment as compared to terrace attachment, conclusively indicating the strong dependence of plasmon coupling strength on the attachment location.

4.3.2 Discrete-dipole approximation

Electrodynamic simulations using the discrete-dipole approximation (DDA) method confirmed the observed regio-selective nature of plasmon coupling in NP/NS dimers (Fig. 4.3). Validation of the simulation method is shown in Fig. 4.7 and additional simulation results are shown in Fig. 4.8-4.10. The simulated shifts are somewhat lower than those in experiment; it is possible that the actual surface-to-surface distance is lower than 1 nm, the value used in the simulation model. After all, coupling-induced shifts increase rapidly with decreasing inter-particle distance[1,13,35] as shown in Fig. 4.11. Nevertheless the simulated site-dependence of the shift is in qualitative agreement with the observations.

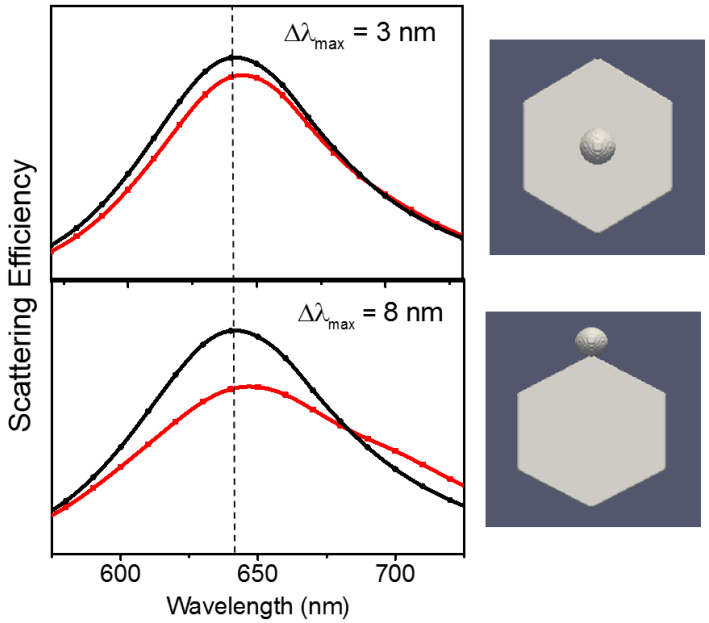

Figure 4.3 Simulated plasmonic coupling between a Au NP and a site-selectively attached Au NS. *DDA simulations show that the attachment of a Au NS to a vertex on the side of the NP (bottom panel, red data-points connected by a cubic spline) results in a 8-nm LSPR red-shift with respect to the LSPR of a NP with no NS attached (black data-points connected by a cubic spline). In contrast, when a Au NS is attached to the terrace of the NP (top panel, red data-points connected by a cubic spline), the coupling is weaker, as manifested by a smaller 3-nm red-shift. Simulations were performed as described in the SI. The NS was 27 nm in diameter. Simulated configurations and NS locations are shown for each case and are representative of experimental structures. The surfaces of the NP and the NS were separated by a distance of 1 nm, measured along the long-axis of the hexagon for the NS placed on the vertex and along the thickness direction for the NS placed on the terrace.*

It is instructive to spatially resolve the site-dependence of plasmon coupling even further, for instance, by determining if there is a systematic difference in the magnitude of shift between specific locations on the terrace or between those on the sides of the NP. While this was difficult to perform in a statistically significant manner using the limited experimental cases, simulations proved useful in this regard (Fig. 4.9 and S4.4). Simulations showed that attachment of a NS closer to the edge of a terrace gave rise to a shift of 3 nm, similar to the case of a NS placed at the center of the terrace. Attachment on the NP sides exhibited a more sensitive site-dependence: the shift for attachment at a vertex site ($\Delta\lambda_{max}$ = 8 nm) was significantly larger than that for attachment at the center of a side face ($\Delta\lambda_{max}$ = 4 nm).

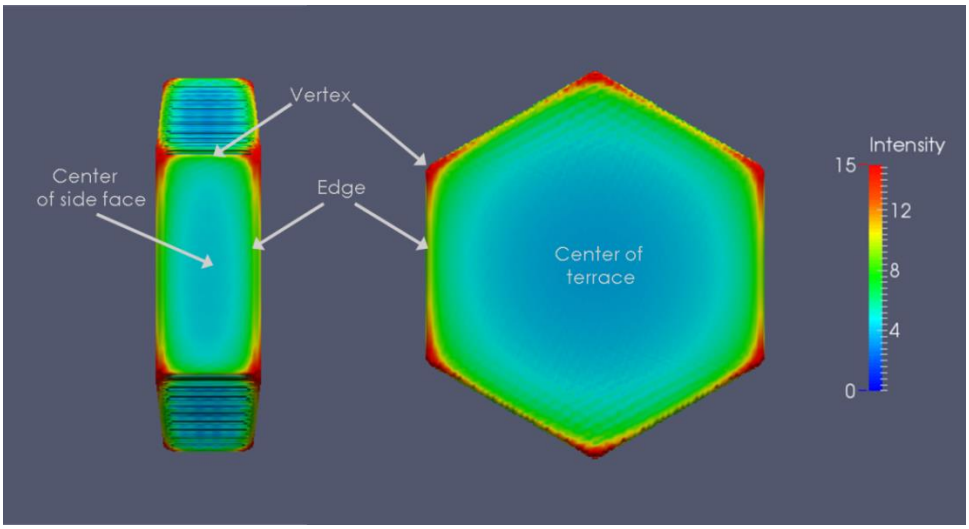

Figure 4.4 Spatial map of the NP polarizability. *Simulated near-field over the surface of a Au NP excited by 645-nm unpolarized light. The near-field is depicted in the form of an amplitude enhancement ($|E|/|E_0|$) on a color scale. The near-field appears to be most intense at the vertices followed by the edges of the NP. On the other hand, the central areas of the terraces and side faces exhibit little field enhancement. Simulations were performed for a hexagonal Au NP with a long axis of 137 nm, a thickness of 31 nm, and a 1 nm thick ligand shell of HT and ATP, representative of the experimental structure.*

The observed site-dependence originates from the spatio-polar variation of the polarizability of the NP, qualitatively analogous to the tensorial nature of the molecular polarizability of benzene.[36] A simulation of the near-field around a resonantly excited NP (Fig. 4.4) serves as a map of the polarizability of the NP. Under in-plane excitation, the NP is most polarizable at its vertices, followed by the edges. The NP is least polarizable at the central regions of terraces and side faces. Thus, a NS, with an induced dipole excited in the plane of the NP, is able to polarize a NP most strongly when it is attached along the sides in contact with the vertices of the NP. In addition to vertex attachment, there is an additional requirement for strong coupling: the excitation must be polarized along the NP/NS axis, such that the dipolar plasmon oscillation of the NP is aligned head-to-tail with the dipolar plasmon oscillation of the NS (Fig. 4.8). These conditions lead to a strong attractive interaction, resulting in a large red-shift of the NP localized surface plasmon resonance (LSPR).[1]

On the other extreme, attachment of the NS at the terrace causes minimal polarization of the NP. While the side-by-side interaction does not allow for a strong interaction between the dipolar LSPR oscillations of the NP and the NS, there is an observable attractive coupling between the dipolar oscillation of the NS and an induced image dipole on the much larger NP surface, as seen from field maps shown in Fig. 4.12. However, this interaction has only a weak effect on the NP dipolar LSPR, manifested as a small red-shift of the latter. Furthermore the nature of this interaction is such that the lateral position of the terrace-attached NS in

relation to the NP edges is not too important in determining the magnitude of the coupling-induced shift (Fig. 4.10). In summary, the overall trend seen in the coupling-induced red-shift, i.e., vertices > side faces > terrace sites, is essentially a reflection of the spatial map of the NP polarizability under in-plane excitation. Experimentally, however, we were unable to resolve a difference in coupling strength for vertex vs. side face sites from the limited number of structures available (Table 4.2). This inability likely resulted from the heterogeneities in (i) the exact position of the NS relative to a vertex (Fig. 4.9), (ii) the actual distance of the NS from the NP surface, (iii) the degree of roundedness of the NP sides, and (iv) the size of the NS, all of which influence the coupling-induced shift, apart from the attachment location of the NS.

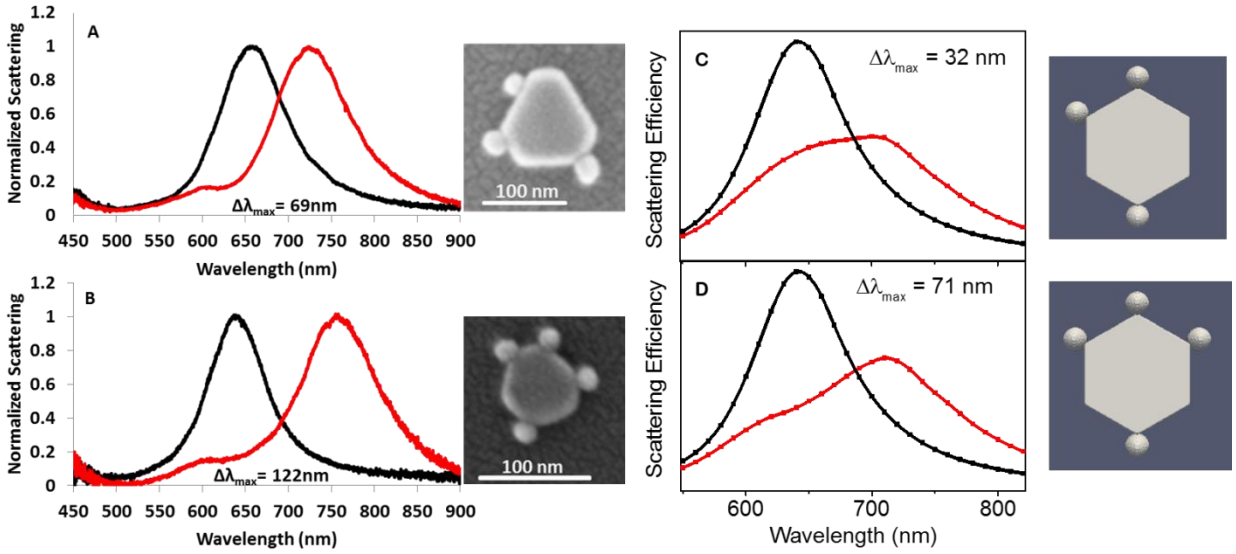

Figure 4.5 *Experimental (A & B) and simulated (C & D) plasmonic coupling between a Au NP and multiple NSs.* ***Dark-field scattering spectra of Au NPs before (black) and after (red) three (A) and four (B) ~25 nm diameter Au NSs are attached to the sides of the Au NPs. The SEM images of the corresponding assemblies are shown on the right. Both experiments and simulations show that each additional Au NS attached to vertices on the sides of the NP (left) results in stronger coupling and a larger red-shift of the LSPR. In fact, coupling with three attached NSs is strong enough that a multipolar mode begins to emerge blue of the dipolar LSPR peak. With four attached NSs, the multipolar mode is strong enough to be clearly resolved from the LSPR peak. Simulations were performed as described in the SI. Here, 27 nm diameter Au NSs were placed at three (C) or four (D) vertices along the sides of the NP (red data-points connected by cubic splines). Simulated configurations and NS locations are shown for each case and are representative of experimental structures. For attachment of three NSs, the LSPR wavelength maximum was determined by fitting the simulated scattering spectrum to a single Lorentzian peak. For four NSs, the spectrum was fit to two Lorentzian peaks. The red-shift $\Delta\lambda_{max}$ indicated for each case is relative to the λ_{max} for a NP without an attached NS (spectrum shown by black data-points connected by a cubic spline). Unpolarized light was used for excitation in the simulations, similar to the conditions in experiment.*

Further studies with multiply attached NSs indicate a unique synergistic effect, whereby the polarizing effect of a NS on the NP is positively assisted by the presence of other attached NSs. As discussed earlier, the attachment of a single NS to the NP sides results in a 22 nm red-shift, on average. With three NSs attached to the sides (Fig. 4.5A), a 69 nm red-shift is seen, amounting to a shift of 23 nm per attached NS. However, the attachment of four NSs around the NP sides is seen to result in a total red-shift of 122 nm (Fig. 4.5B), which amounts to a shift of 31 nm/NS, considerably larger than the effect produced by a single NS. This observation is in contrast to the behavior observed in core-satellite assemblies, where a linear LSPR shift is observed with an increasing number of satellite NSs.

While experimental heterogeneity makes it difficult to unequivocally confirm this synergistic effect, the accompanying simulations provide support for this conclusion. In simulations, the attachment of one NS to a vertex position results in a 8-nm shift, as discussed earlier (Fig. 4.3). However, with three NSs attached to three vertices of the NP (Fig. 4.5C), the red-shift is 32 nm, amounting to a shift of ca. 11 nm/NS. Four NSs attached to four vertices of the NP (Fig. 4.5D), give rise to an overall shift of 71 nm or ca. 18 nm/NS. The synergistic effect found here is analogous to the positive enhancement in the molecular polarizability of benzene by certain activating functional groups.[37]

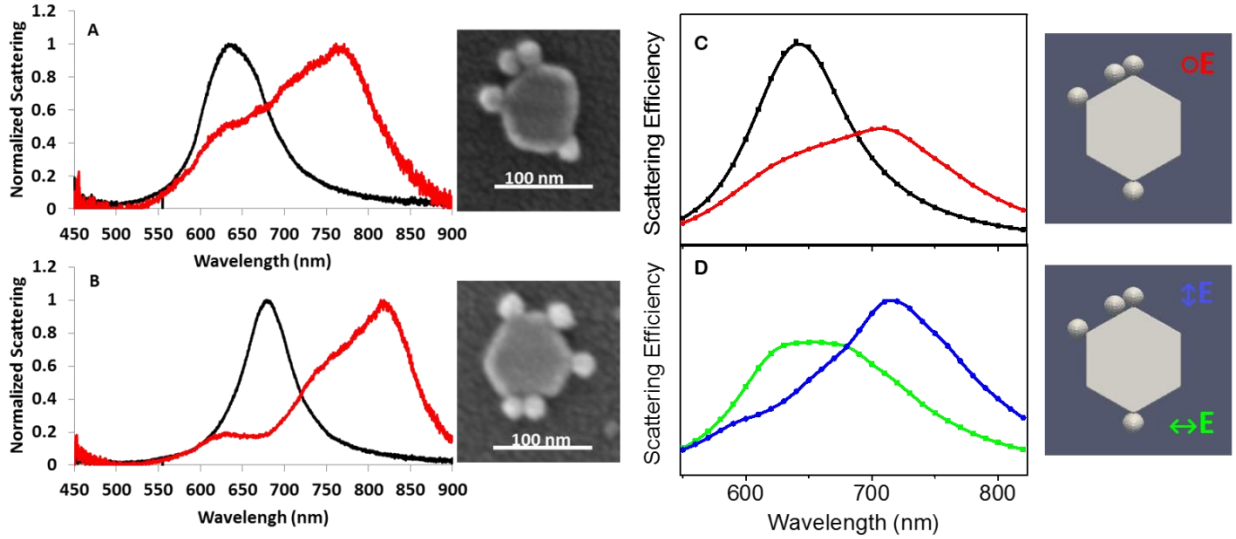

Figure 4.6 *Experimental (A & B) and simulated (C & D) plasmonic coupling between a Au NP and multiple asymmetrically distributed NSs.* ***Dark-field light-scattering spectra of a roughly hexagonal Au NP before (black) and after (red) attachment of four (A) and five (B) asymmetrically distributed NSs to the sides of the NP. The SEM images of the corresponding assemblies are shown on the right. Both experiments and simulations show that when multiple NSs are distributed asymmetrically around the NPs, a spectrum with multiple bands is seen. Simulations were performed as described in the SI. Here, four 27-nm diameter Au NSs were placed along the sides of the NP. The simulated configuration, representative of the experimental configuration in (A), is shown besides each simulated spectrum. In (C), the simulated spectrum of the NP/NS assembly (red data-points connected by a cubic spline) under unpolarized light excitation is shown alongside the simulated spectrum of a NP with no NSs attached (black data-points connected by a cubic spline), also for unpolarized light excitation. In (D), simulated spectra of the NP/NS assembly are shown for light polarized along the NP short-axis (green data-points connected by a cubic spline) and for light polarized along the long-axis (blue data-points connected by cubic spline). The spectrum for long-axis polarization, fit to two Lorentzian peaks, shows a lower energy band centered at 721 nm, red-shifted from the NP LSPR by as much as 79 nm. The spectrum for short-axis polarization, fit to one Lorentzian peak, shows a band centered at 656 nm.***

In assemblies with multiple NSs, the respective placement of NSs on the NP must dictate the nature of plasmonic coupling and the resulting spectral characteristics of the assembly. In contrast to the uniform distribution of NSs, shown in Fig. 4.5, we found some instances of NSs asymmetrically distributed around the NP sides (Fig. 4.6). These structures exhibited broad, asymmetric, and complex spectra, quite unlike those seen with the symmetric distributions. The strongest scattering band of these asymmetric structures appears to be much more strongly red-shifted than in the case of an equivalent (with the same number of NSs) symmetric distribution, e.g., $\Delta\lambda_{max}$ = 132 nm in Fig. 4.6A vs. 122 nm in Fig. 4.5B. DDA simulations of such a NP/NS assembly, excited with unpolarized light, reproduced the broad, asymmetric nature of the LSPR spectrum (Fig. 4.6C) with the strongest scattering band red-shifted by as much as 79 nm. This red-

shift is larger than that for the symmetric distribution with four NSs in Fig. 4.5D ($\Delta\lambda_{max}$ = 71 nm under unpolarized excitation).

The complex nature of the spectrum is a result of the large polarization anisotropy of the asymmetric NP/NS assemblies, as shown by further polarization-dependent simulations. Due to the asymmetry of the structures, the strength of coupling between the NP and NSs is strongly dependent on the polarization direction. The latter is manifested by the large disparity in the simulated scattering spectra for the two orthogonal polarization directions (Fig. 4.6D). The symmetric distributions also show similar polarization anisotropy (Fig. 4.14), but this effect is much starker for the asymmetric distributions. For the representative asymmetric structure simulated, three NSs are located along the long-axis direction, whereas only one NS is located in the short-axis direction. As a result, coupling along the long-axis direction is significantly stronger than that along the short-axis direction. The spectrum under long-axis polarization exhibits at least two modes, including a strong highly red-shifted mode centered at 721 nm and a weaker blue-shifted (as discussed later, a quadrupolar) mode around 613 nm. On the other hand, the short axis-polarization results in a broad band centered around 656 nm. With unpolarized light excitation, which samples all directions equally, the spectrum comprises of these multiple coupled modes corresponding to different polarization directions and therefore the spectrum is multi-peaked and asymmetric. This is unlike the case of symmetric distributions where modes polarized along the two orthogonal directions are closer to each other in energy and in intensity; therefore the composite spectrum is more symmetric and the composite red-shift is somewhat smaller. A similar effect is shown in Fig. 4.13 for multiple NSs distributed on terrace sites of somewhat asymmetric NPs.

An additional effect is seen with multiply attached NSs, both in experiment and in simulations (Fig. 4.5 and 4.6). Strong coupling with multiple NSs attached on the NP sides induces a new mode around 625 nm, blue of the dipolar LSPR of the NP (Fig. 4.5A and 4.5C). Whereas a weak shoulder is seen with one NS attached (Fig. 4.2B), with four NSs attached, this new mode is strong enough to be clearly resolved from the LSPR peak (Fig. 4.5B and 4.5D). An electric-field simulation indicates that this mode is the result of a quadrupolar excitation of the NP/NS assembly polarized along the short in-plane axis of the NP (Fig. 4.14 and 4.15).

4.4 Conclusion

In summary, we designed, in analogy with benzene-derived molecular structures, complex plasmonic nanoassemblies by regio-selectively attaching Au NSs to specific sites on the surface of a large hexagonal Au NP. In these assemblies, we find that the site of NS attachment dictates the plasmonic response of the

NP: NSs attached on the sides, especially at vertices, couple strongly with the NP, whereas NSs attached on the terraces cause little perturbation of the NP plasmon resonance. Such regio-selective placement of satellite NSs on the surface of a NP has potential for producing unique structure-dependent electromagnetic modes with interesting spectral attributes and near-field distributions. As one example of unique behavior, we find that the polarizing effect of multiple NSs on the NP is synergistic. As another example, we find that the optical response is dramatically different for an assembly with a uniform distribution of NSs around the NP versus one with an asymmetric distribution. The regio-selectivity of plasmon coupling discussed here can be exploited for 3D spatial sensing with nanometer resolution. For instance, it may be possible to construct a device consisting of a NP linked to a NS via a protein of interest. The device may be designed such that the occurrence of a key conformational change in the protein results in the migration of the attached NS from the sides of the NP to the outer terrace region. Our results show that the spectral shift resulting from such a dynamic configuration change would be optically detectable on the level of single nanodevices. Future work will be geared toward the achievement of increasingly finer and more dynamic regio-selective control and the exploitation of such control in functional plasmonic devices.

4.5 Methods

4.5.1 Experimental methods

Chemicals. Citric acid trisodium salt, L-Ascorbic acid, sodium borohydride, cetyltrimethylammonium bromide (CTAB), mercaptopropyltrimethoxysilane (MPTMS), 1-hexanethiol (HT), 4-aminothiophenol (4-ATP), 2-propanol, ethyl alcohol, and acetone were purchased from Sigma-Aldrich. $HAuCl_4.3H_2O$ was synthesized from metallic Au.

Synthesis of Au seeds and 25-nm diameter Au nanospheres (NSs). Small 3-5 nm diameter Au NSs, termed "Au seeds" were synthesized by adding 0.6 mL of ice cold 0.1 M $NaBH_4$ to 19 mL of an aqueous solution of 2.5 x 10^{-4} M trisodium citrate and 2.5 x 10^{-4} M $HAuCl_4.3H_2O$ under stirring.[38] The Au seed solution was used to synthesize Au nanoplates (NPs) 2 h after their preparation as described in the next section. ~25-nm diameter citrate-stabilized Au NSs were synthesized by adding 10 mL of a 1% sodium citrate solution to 100 mL of a boiling 2.5 x 10^{-4} M $HAuCl_4.3H_2O$ solution. The mixed solution was kept stirring and boiling for 1 h and cooled down to room temperature with stirring before use. The ~25-nm diameter Au NS solutions were used 1 h after preparation.

Synthesis of Au NPs directly on glass surfaces with optimal size and coverage. Glass slides were prepared with etched number markings using photolithography, which was followed by a buffered oxide

etch at the University of Louisville Micro/Nano Technology Center. Au nanostructures were synthesized directly on the glass slides using a seed-mediated growth method reported by our group recently,[31] but with a small modification designed to decrease the size and density of the NPs on the surface so that they would be amenable to single nanoparticle dark-field scattering studies. The glass slides were first functionalized with 3-mercaptopropyltrimethoxysilane (MPTMS) by soaking in a solution of 10 mL of 2-propanol, 100 μL of MPTMS, and a few drops of water at a temperature of 95 °C for 30 min. After rinsing thoroughly with 2-propanol and drying under N_2, the MPTMS-functionalized slides were then placed into a 1:10 diluted solution of Au seeds for 5 min, rinsed with Nanopure® water, and dried under N_2. Next, the samples were placed into a Au growth solution containing 9.0 mL of 0.1 M cetyltrimethylammonium bromide (CTAB), 450 μL of 0.01 M $HAuCl_4.3H_2O$, and 50 μL of 0.1 M ascorbic acid for 5 min, followed by rinsing with Nanopure® water, and drying under N_2. In our previous work, we placed them in a growth solution for 1 h, which led to much larger Au NPs that are unsuitable for our single-nanoparticle scattering studies because of their broader, more red-shifted and complex scattering peaks. Following growth, the samples on the glass slides contain a mixture of Au NPs and Au NSs. The NSs and some NPs were removed by sonication for 10 min. This procedure led to samples with >90% Au NPs at a low area-density, which is necessary for the single nanoparticle dark-field scattering experiments. The NPs were determined to be typically ~100 nm wide and ~30 nm thick according to scanning electron microscopy (SEM) and atomic force microscopy (AFM) images.

Controlled attachment of Au NSs to the side faces/vertices of Au NPs. HT ligands were assembled onto the Au NPs and then place-exchanged with 4-ATP ligands. 4-ATP is a good bi-functional organic ligand that allows the coupling of citrate-coated Au NSs to Au NPs, since it has a thiol group that attaches well to the Au NPs and an NH_2 group that, when protonated to NH_3^+, allows electrostatic attachment of negatively-charged, citrate-coated Au NSs. The pH of the Au NS solution, which was maintained at 4.8 for all experiments, dictates the level of NH_2 protonation on 4-ATP and has a large impact on NS attachment.

In this procedure, we placed the glass slide with Au NPs in a 1 mM ethanol solution of HT overnight. We rinsed the sample thoroughly with ethanol, followed by drying under N_2, and then exchanged the HT monolayer with 4-ATP by placing the sample in a 6 mM ethanol solution of 4-ATP for 1 h. We again rinsed the sample thoroughly with ethanol and dried under N_2. The substrates were then immersed in a 10-mL solution of ~25-nm diameter Au NSs for 30 min, rinsed thoroughly with Nanopure® water, and dried under N_2. The thiol place-exchange occurs preferentially at side face/vertex sites of the NPs, which leads to a high density of 4-ATP at these sites and subsequent electrostatic binding of Au NSs at those sites.

Controlled attachment of Au NSs to terrace sites of Au NPs. In order to selectively bind the NSs to terrace sites, the samples were first placed in a 1 mM ethanol solution of 4-ATP overnight, rinsed

thoroughly with ethanol, and dried under N_2. Then, we exchanged the 4-ATP with HT by placing the sample into a 6 mM ethanol solution of HT for 4 h. We again rinsed thoroughly with ethanol and dried under N_2. Finally, the substrates were immersed in 10 mL of a pH 4.8 solution of ~25-nm diameter Au NSs for 30 min, rinsed thoroughly with Nanopure® water, and dried under N_2. In this procedure, the original 4-ATP ligands on the Au NPs were displaced by HT preferentially at the side face/vertex sites, leading to the blocking of those regions from Au NS attachment and controlled binding of Au NSs to the terrace sites.

Spectroscopic and microscopic characterization. Scattering spectra were collected from individual NPs or coupled NP/NS assemblies using resonant Rayleigh dark-field scattering spectroscopy. Dark-field imaging was performed with an inverted Nikon Eclipse Ti microscope with a halogen lamp light source and a dark-field condenser (N = 0.95-0.80) for sample illumination and a 100x variable aperture oil immersion objective (N = 0.5-1.3) for collection of the scattered light from individual NPs or coupled NP/NS assemblies. An Infinity camera from Lumenera Corporation was used to obtain high-resolution video images for selecting individual particles. The detector used for measuring light scattering intensity as a function of wavelength was a multichannel air-cooled CCD camera used in a Horiba XPLORA-Inv confocal Raman system.

Scattering spectra obtained as a function of wavelength, were plotted in terms of energy units (eV) and then fit in OriginLab to single or multiple Lorentzian peaks, as noted. Peak maxima of scattering bands obtained in energy units (eV) were converted to wavelength units (nm). Coupling-induced LSPR shifts ($\Delta\lambda_{max}$) were determined from wavelength maxima.

4.5.2 Computational methods

DDA simulations of Au hexagonal NPs and coupled NP/NS assemblies. The discrete-dipole approximation (DDA) method was used for the simulation of LSPR spectra of Au NPs and for studying plasmon coupling of Au NPs with Au NSs. The DDA method numerically solves Maxwell's equations for one or a series of arbitrarily shaped objects by discretizing each object into a cubic array of N polarizable point dipoles and self consistently solving for the polarizability of each dipole interacting with the incident field and all other N-1 dipoles. We employed the open source DDSCAT 7.3.0 code from Draine and Flatau.

The hexagonal NP target was generated via tools available on nanoHUB.org. A triangular mesh description of the hexagonal geometry was generated using the open-source 3D design tool "Blender". Using the "DDSCAT Convert" tool (doi: 10.4231/D3FB4WM99), the geometry was discretized into a three-dimensional virtual dipole array, the input for DDSCAT. To simulate the dielectric properties of the ligand shell of NPs with Au NSs attached at the side faces/vertices, a 1-nm thick layer of HT (n =1.448)[39] was added to the surfaces of the top and bottom NP terraces and a 1-nm thick layer of 4-ATP (n =1.663)[40] was

added to the surfaces of the side faces. Coupling between hexagonal NPs and NSs was simulated by attaching NSs to various sites on the side faces/vertices of the NP. To simulate the dielectric properties of the ligand shell of NPs with Au NSs attached at the terraces, a 1-nm thick layer of HT (n =1.448) was added to the surfaces of the side faces and a 1-nm thick layer of 4-ATP (n =1.663) was added to the surfaces of the top and bottom terraces. Au NSs of 27-nm diameter were generated using the DDSCAT subroutine CALLTARGET and combined with the NP target. For every case, the surface-to-surface separation distance between the NP and the NS was 1 nm, i.e., the NS was in contact with the ligand shell, which is the likely scenario in experiments. Note that this interparticle distance is measured along the thickness direction for NSs placed on the terraces and along one of the hexagonal axes for NSs placed on the side faces/vertices.

In order to match experimental conditions of dark-field scattering spectroscopy, all target structures were excited with unpolarized light, simulated by a circularly polarized plane wave, unless otherwise noted. Light, incident normal to the face of the NP, propagated along the thickness of the NP. In all simulations, the refractive index of the ambient medium was set at n_m = 1.1, representative of a mixture of air ($n \approx 1$) and glass ($n \approx 1.5$). The relative contribution of air and glass was determined by the relative volume fraction of each within the surrounding medium, the surrounding medium being defined as the additional volume when the NP dimensions were extended 50% from the center of the NP along each axis. The bulk experimental dielectric function of Au from Johnson and Christy was utilized for all calculations without any corrections.

Scattering spectra (scattering efficiency vs. wavelength) were obtained from each simulation. Spectra were plotted in energy units (eV) and then fit in OriginLab to single or multiple Lorentzian peaks, as noted. Peak maxima of scattering bands obtained in energy units (eV) were converted to wavelength units (nm). Standard error was ca. 1 nm for all Lorentzian fits. Coupling-induced LSPR shifts ($\Delta\lambda_{max}$) were determined from wavelength maxima.

In addition to spectra, for four of the targets (a single NP, a NP coupled with a single NS for two different interparticle distances, and a NP coupled with four NSs), near-field calculations were performed for specific light excitation conditions, i.e., wavelength and polarization. These near-field calculations utilized DDSCAT 7.3 subroutine NEARFIELD. The macroscopic field amplitude |E| at each grid-point of a volume surrounding the target structure was obtained relative to the incident field amplitude $|E_0|$, with the latter set to a value of 1. Near-field enhancements ($|E|/|E_0|$) were plotted over the surface of the target, using the open source application ParaView.

4.6 Additional figures

Table 4.1 *LSPRs and SEM images of representative single Au NPs with a NS attached on the terrace.*

Initial λ_{max} (nm)	Initial Peak Width (nm)	Final λ_{max} (nm)	Final Peak Width (nm)	Shift (nm)	NS Size (nm)	Morphology
657	79	659	82	2	25	
659	112	661	104	2	26	
660	134	664	124	4	24	
679	103	682	105	3	23	
686	116	688	123	2	29	
707	120	709	117	2	25	
				Average =3±1	Average = 25±2	

Table 4.2 *LSPRs and SEM images of representative single Au NPs with a NS attached on a side face/ vertex.*

Initial λ_{max} (nm)	Initial Peak Width (nm)	Final λ_{max} (nm)	Final Peak Width (nm)	Shift (nm)	NS Size (nm)	Morphology
653	89	667	133	14	22	
673	82	696	88	23	20	
673	96	702	120	29	28	
678	94	699	138	21	27	
				Average =22±5	Average = 24±4	

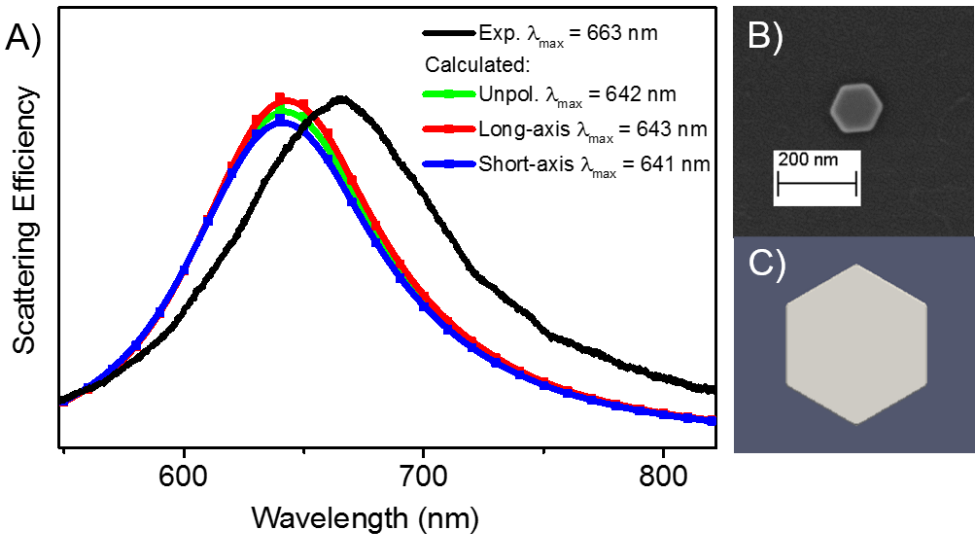

Figure 4.7 *(A) Light-scattering spectrum of a single Au NP obtained via dark-field spectroscopy (black curve) and DDA simulations (red, green, and blue data points). Wavelength maxima listed were determined by fitting spectra to single Lorentzian peaks. In simulations, unpolarized light (green data-points connected by a cubic spline shown by the solid green curve) was employed for excitation, similar to the experimental conditions. Simulated spectra are also shown for incident light linearly polarized along the long in-plane axis of the NP (red data-points connected by a cubic spline shown by the solid red curve) and light polarized along the short in-plane axis of the NP (blue data-points connected by a cubic spline shown by the solid blue curve). Scattering spectra are similar for different polarization conditions, indicative of the small in-plane anisotropy of the hexagonal shape. (B) SEM image of the experimental nanoplate with a long-axis length of 136 nm and thickness of 33 nm. (C) Rendition of the simulated structure, a Au NP with a long-axis length of 137 nm and a thickness of 31 nm, dimensions chosen to be closely representative of those obtained from SEM images for several experimental NPs. In summary, simulated spectra show good agreement with the experimental ones. Small differences are likely due to minor differences in the dimensions and/or curvature of the hexagonal NP edges between the experimental and simulated NPs.*

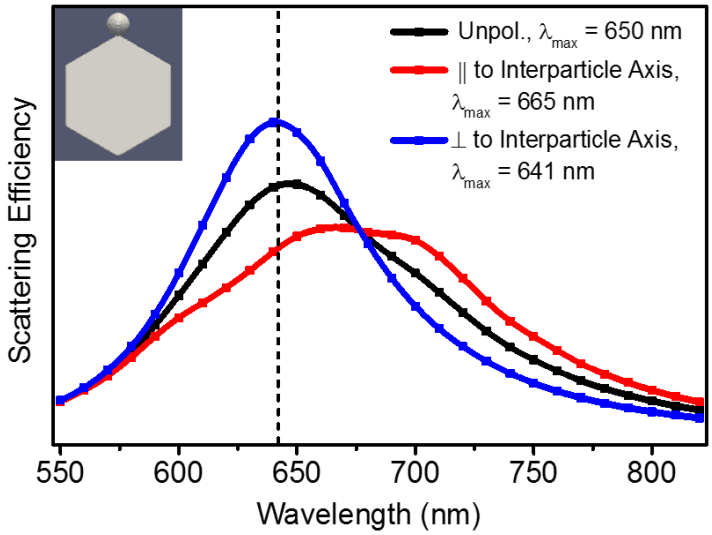

Figure 4.8 *Simulated effect of incident light polarization on the plasmon coupling between a Au NP and a Au NS attached to a vertex on the side of the NP***.** *Simulations were performed for a hexagonal Au NP with a long axis of 137 nm, a thickness of 31 nm, and a 1-nm thick ligand shell of HT and 4-ATP, representative of the experimental structure. A single Au NS, with a diameter of 27 nm, was attached to a vertex on the side of the NP, in the plane of the hexagon, as shown by the rendition in the inset. The distance between the surfaces of the NP and the NS was 1 nm, measured along the long-axis of the hexagon. Wavelength maxima of scattering spectra were determined by fitting to single Lorentzian peaks. The dashed black line shows the* λ_{max} *for a NP without an attached NS. Relative to the peak position of this uncoupled case, coupling with the NS gives rise to a red-shift of 23 nm when the excitation light is polarized along the interparticle axis (red data-points connected by a cubic spline). On the other hand, there is a blue shift of 1 nm when light is polarized perpendicular to the interparticle axis (blue data-points connected by a cubic spline). This difference is consistent with the excitonic model of LSPR coupling.*[5] *In the former case, the dipolar plasmon oscillations of the NP and NS are aligned head-to-tail, resulting in favorable coupling. In the latter case, the dipolar plasmon oscillations of the NP and NS are parallel to one another and therefore coupling between them is weakly repulsive. With unpolarized light excitation (black data-points connected by a cubic spline), the net strength of coupling and the extent of LSPR red-shift is intermediate to the two polarization extremes.*

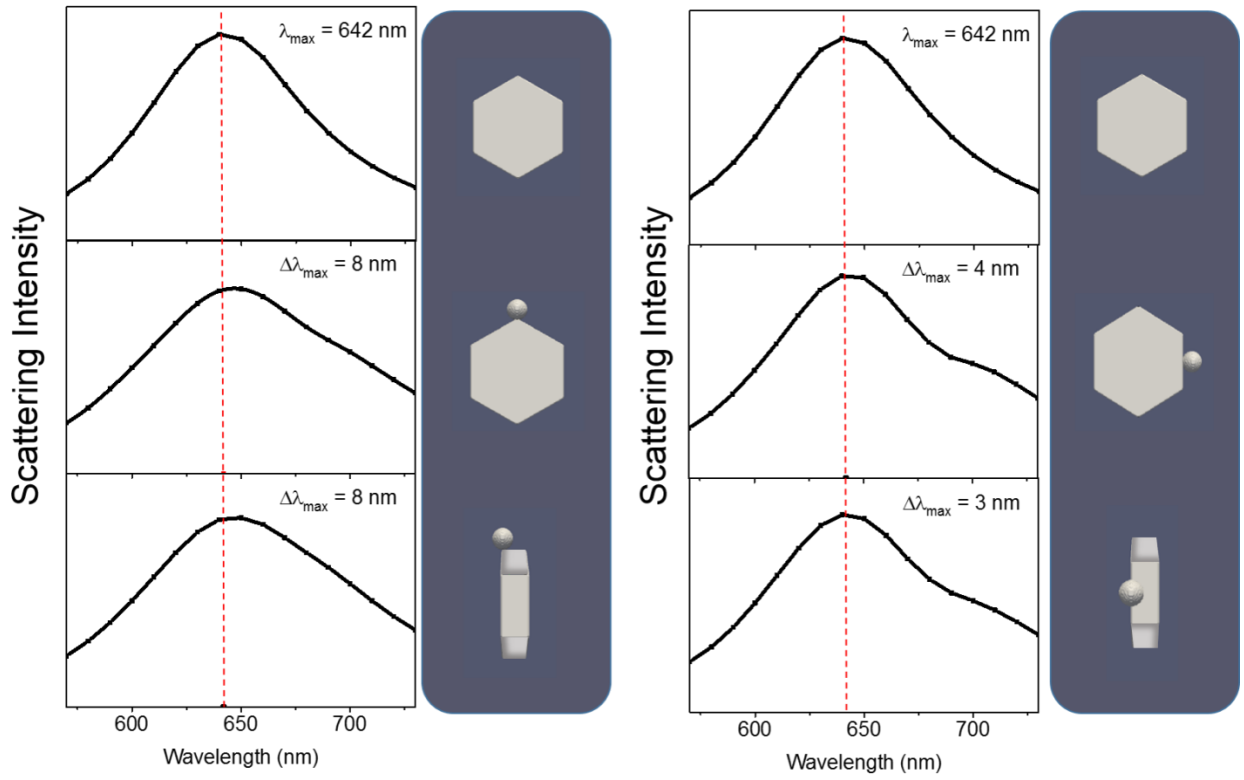

Figure 4.9 *Simulated plasmon coupling between a Au NP and a Au NS: effect of the attachment location of the NS along the sides of the NP. Simulations were performed for a hexagonal Au NP with a long axis of 137 nm, a thickness of 31 nm, and a 1-nm thick ligand shell of HT and 4-ATP, representative of the experimental structure (top panel). A single Au NS, 27 nm in diameter, was then placed at one of four select locations along the sides of the NP: at a vertex in the plane of the hexagon (left, middle panel), at the center of a side face in the plane of the hexagon (right, middle panel), at a vertex out of the plane of the hexagon (left, bottom panel), and at the center of a side face out of the plane of the hexagon (right, bottom panel). Renditions of these simulated configurations are shown besides each spectrum. The surfaces of the NS and the NP were separated by a distance of 1 nm, measured along one of the axes of the hexagon. Excitation was performed with unpolarized light. Spectra are shown as data-points connected by cubic splines (solid black curves). Wavelength maxima of scattering spectra were determined by fitting to single Lorentzian peaks. The dashed red line shows the* λ_{max} *for a NP without an attached NS. Relative to the peak position for this uncoupled case, coupling with the NS gives rise to a red-shift, indicated by* $\Delta\lambda_{max}$*. Of the cases considered, coupling is strongest (*$\Delta\lambda_{max}$ *= 8 nm) when the NS is located at the vertex. Coupling is weaker for the cases where the NS is located at the center of a side face, away from the vertices. Also, for the cases where the NS is located on the side face of the NP, a noticeable shoulder emerges in the scattering spectrum; this feature affects somewhat the apparent red-shift obtained from the fit to a single Lorentzian peak. The coupling is slightly weaker for the out-of-plane side face location (*$\Delta\lambda_{max}$ *= 3 nm) as compared to the in-plane side face location (*$\Delta\lambda_{max}$ *= 4 nm).*

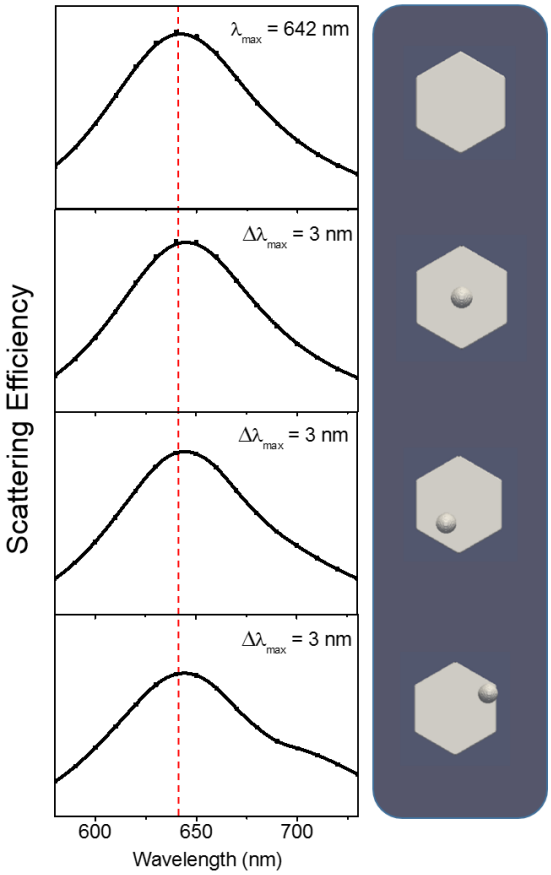

Figure 4.10 *Simulated plasmon coupling between a hexagonal Au NP and an Au NS: effect of the location of the NS on the terrace of the NP. Simulations were performed for a hexagonal Au NP with a long axis of 137 nm, a thickness of 31 nm, and a 1-nm thick ligand shell of HT and 4-ATP, representative of the experimental structure (topmost panel). A single Au NS, 27 nm in diameter, was then placed at one of three select locations on the terrace of the NP: at the center of the terrace (second panel from top), close to the edge of the terrace (bottommost panel), and midway between these two locations (third panel from top). Renditions of these simulated configurations are shown besides each spectrum. The surfaces of the NS and the NP were separated by a distance of 1 nm, measured along the thickness of the NP. Excitation was performed with unpolarized light. Spectra are shown as data-points connected by cubic splines (solid curves). Wavelength maxima of scattering spectra were determined by fitting to a single Lorentzian function. The dashed red line shows the λ_{max} for a NP without an attached NS. Relative to the peak position of this uncoupled case, coupling with the NS gives rise to a red-shift, indicated by $\Delta\lambda_{max}$. For all three positions, the $\Delta\lambda_{max}$ is 3 nm. Fig. 4.12 shows that a terrace NS couples to the surface of the NP but not necessarily to the NP dipolar mode, making the lateral position of the NS in relation to the NP edges less important. For the case where the NS is located at the edge of the terrace (bottommost panel), a noticeable shoulder emerges in the scattering spectrum; this feature affects somewhat the apparent red-shift obtained from the fit to a single Lorentzian peak.*

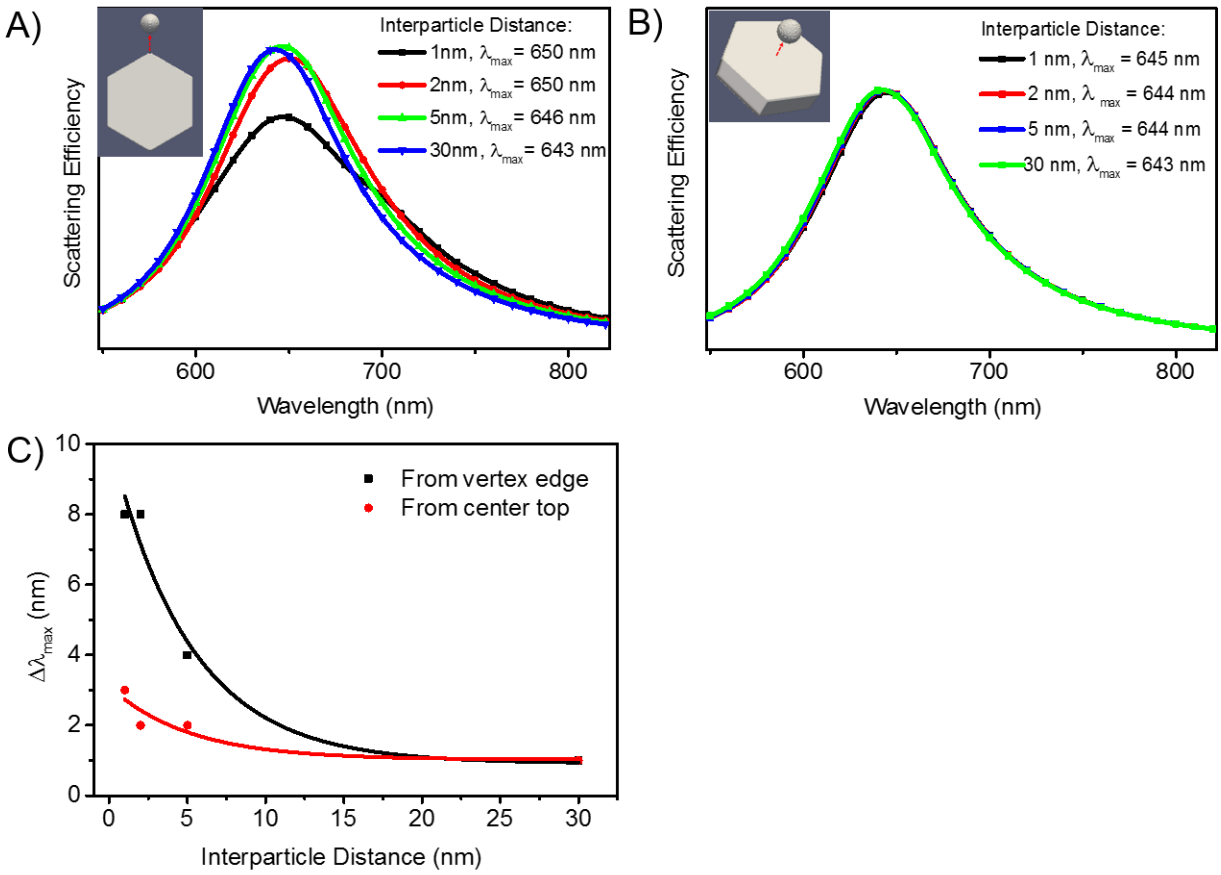

Figure 4.11 *Simulated distance-dependence of plasmon coupling between a Au NP and a single Au NS for two cases: a NS placed at a vertex on the side (A) and a NS placed at the center of the terrace (B) as shown by the renditions in the insets. Simulations were performed for a hexagonal Au NP with a long axis of 137 nm, a thickness of 31 nm, and a 1-nm thick ligand shell of HT and 4-ATP, representative of the experimental structure. A single Au NS, 27 nm in diameter, was then placed either at the vertex on the side in the plane of the hexagon (A) or at the center of the terrace (B) at varying surface-to-surface interparticle distances. This distance was measured along the NP long-axis for (A) and along the thickness direction for (B). Excitation was performed with unpolarized light. Spectra are shown as data-points connected by cubic splines (solid curves). Wavelength maxima of scattering spectra were determined by fitting to single Lorentzian peaks. The coupling-induced red-shift $\Delta\lambda_{max}$, relative to the LSPR peak position of a NP without an attached NS, is plotted in (C) as a function of surface-to-surface interparticle distance. The coupling strength, as indicated by the magnitude of the red-shift, increases with decreasing interparticle distance.*

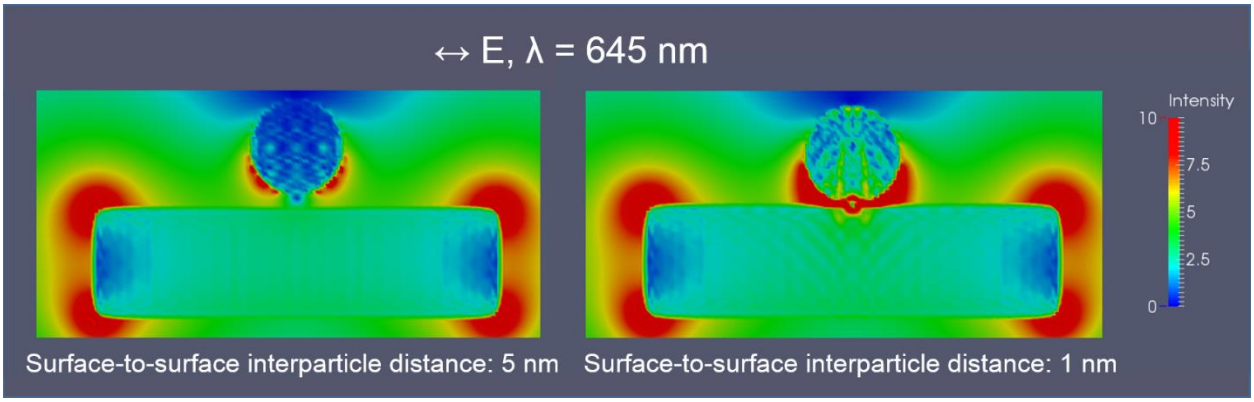

Figure 4.12 *Simulated near-field of a Au NP coupled to a Au NS placed on the terrace of the NP. The images represent a side-view of a cross-section taken along the polarization direction. The near-field is depicted in the form of an amplitude enhancement ($|E|/|E_0|$) on a color scale. Simulations were performed for a hexagonal Au NP with a long axis of 137 nm, a thickness of 31 nm, and a 1-nm thick ligand shell of HT and 4-ATP, representative of the experimental structure, and a 27 nm diameter Au NS. For the left image, the surface-to-surface interparticle distance is 5 nm and for that on the right, it is 1 nm. Corresponding spectra are shown in Fig. 4.11. The near-field pattern shows a strong dipolar mode excited in the NP. The NS placed 5-nm away from the NP exhibits an asymmetric near-field distribution: the near-field is concentrated on the NS surface that is closer to the NP. At a distance of 1-nm, the near-field is concentrated in the gap between the NS and NP, which is indicative of an attractive interaction between the dipolar plasmon oscillation of the NS and image dipoles induced on the surface of the NP.*

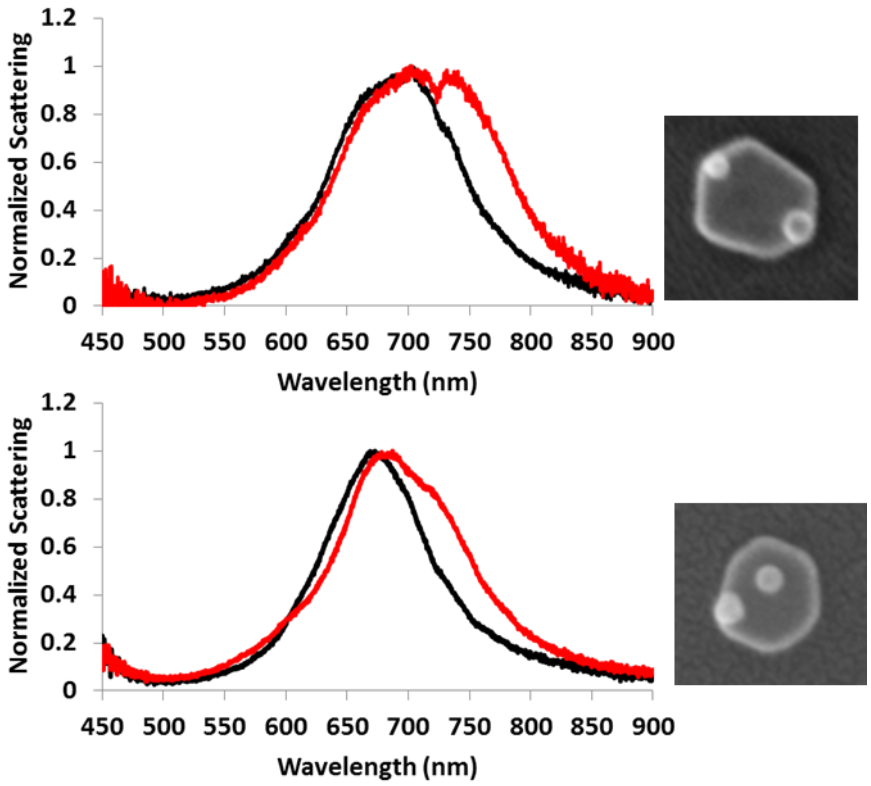

Figure 4.13 *Single-particle dark-field light-scattering spectra of a roughly hexagonal Au NP before (black) and after (red) attachment of multiple NSs to NP terrace sites. Final morphologies are displayed on the right. When multiple NSs were distributed non-symmetrically on inner terrace sites and near terrace edges, we often observed broadening resulting from the appearance of a new peak red-shifted as much as 35-40 nm relative to the initial dipolar mode of the NP. This phenomenon is a result of increased symmetry breaking in the coupled NP/NS assemblies. This effect appeared to be starker when the initial NP itself was not very symmetric, as seen from the representative cases shown in this figure.*

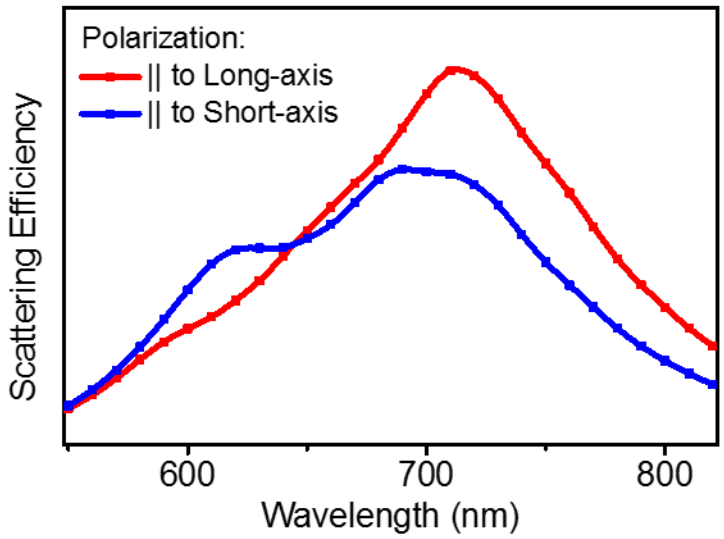

Figure 4.14 *Simulated effect of the incident light polarization on the plasmon coupling between an Au NP and four NSs. Simulations were performed for a hexagonal Au NP with a long axis of 137 nm, a thickness of 31 nm, and a 1-nm thick ligand shell of HT and ATP, representative of the experimental structure. Four Au NSs, each with a diameter of 27 nm, were attached to four of the vertices of the NP, (configuration is shown in Fig. 4.15). The surface-to-surface distance between the NP and each NS was 1 nm, measured along the long-axis of the hexagon. The redshift in the dipolar LSPR resulting from coupling is smaller when light is polarized parallel to the short axis of the hexagon (blue data-points connected by a cubic spline) as compared to the case when light is polarized parallel to the long-axis of the hexagon (red data-points connected by a cubic spline). However, under short-axis polarization, coupling results in the emergence of a prominent high energy mode centered at 613 nm, in addition to the dipolar mode at 705 nm. These* λ_{max} *values were determined by fitting the spectrum to two Lorentzian peaks. The scattering spectrum for long-axis polarization, fit to two Lorentzian peaks, yields a strong dipolar mode with a* λ_{max} *at 717 nm and only a weak shoulder in the blue region.*

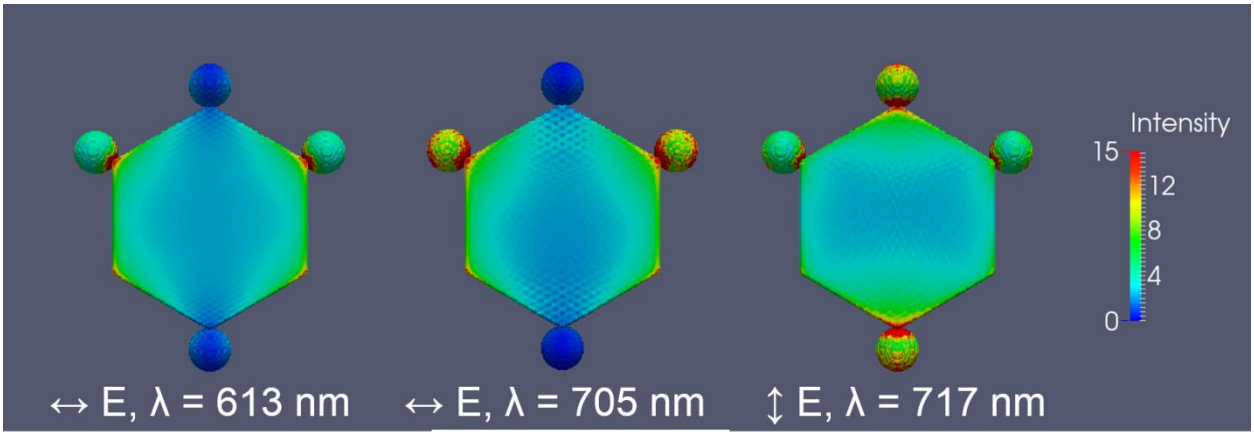

Figure 4.15 *Simulated near-field over the surface of a Au NP coupled to four Au NSs. The near-field is depicted in the form of an amplitude enhancement ($|E|/|E_0|$) on a color scale. Simulations were performed for a hexagonal Au NP with a long axis of 137 nm, a thickness of 31 nm, and a 1-nm thick ligand shell of HT and 4-ATP, representative of the experimental structure. Four Au NSs, each with a diameter of 27 nm, were attached to four of the vertices of the NP, as depicted. The surface-to-surface distance between the NP and each NS was 1 nm, measured along the long-axis of the hexagon. Three different simulations were run: the direction of polarization and wavelength of incident light employed in each simulation are noted for each near-field plot. An electrostatic charge distribution corresponding to each near-field plot is also shown below each plot. When the incident light is polarized parallel to the long axis of the hexagon (right panel), the near-field appears to be concentrated most at the extremities of the NSs located along the polarization direction, as well as at the junctions between the NS and NP vertices. As indicated by its respective electrostatic charge distribution, the field plot represents a dipolar mode of coupling between the NP and the two NSs, which is manifested as the LSPR peak centered at 717 nm in Fig. 4.14. A similar dipolar mode of excitation is seen when light with a wavelength of 705 nm is polarized along the short axis of the hexagon (middle panel). However, when the short axis of the hexagon is excited using 613-nm wavelength light, corresponding to the higher energy peak in Fig. 4.14, the field appears to be concentrated primarily at the junctions between the NS and NP vertex (left panel). There is lower field enhancement at the extremities of the NSs along the polarization direction. This field pattern is indicative of a higher-energy quadrupolar mode of excitation, as depicted by its respective electrostatic charge distribution.*

4.7 References

1. Jain, P. K., Eustis, S. & El-Sayed, M. A. Plasmon coupling in nanorod assemblies: Optical absorption, discrete dipole approximation simulation, and exciton-coupling model. *J. Phys. Chem. B* **110,** 18243–18253 (2006).

2. Jain, P. K. & Deeb, C. *Near-Fields in Assembled Plasmonic Nanostructures*. **0,** (2011).

3. Wang, H., Brandl, D. W., Nordlander, P. & Halas, N. J. Plasmonic nanostructures: Artificial molecules. *Acc. Chem. Res.* **40,** 53–62 (2007).

4. Hao, E. & Schatz, G. C. Electromagnetic fields around silver nanoparticles and dimers. *J. Chem. Phys.* **120,** 357–366 (2004).

5. Nordlander, P., Oubre, C., Prodan, E., Li, K. & Stockman, M. I. Plasmon hybridization in nanoparticle dimers. *Nano Lett.* **4,** 899–903 (2004).

6. Prodan, E., Radloff, C., Halas, N. J. & Nordlander, P. A hybridization model for the plasmon response of complex nanostructures. *Science* **302,** 419–422 (2003).

7. Lassiter, J. B. *et al.* Close encounters between two nanoshells. *Nano Lett.* **8,** 1212–1218 (2008).

8. Khoury, C. G., Norton, S. J. & Vodinh, T. Plasmonics of 3-D nanoshell dimers using multipole expansion and finite element method. *ACS Nano* **3,** 2776–2788 (2009).

9. Kim, D. S. *et al.* Real-space mapping of the strongly coupled plasmons of nanoparticle dimers. *Nano Lett.* **9,** 3619–3625 (2009).

10. Sheikholeslami, S., Jun, Y. W., Jain, P. K. & Alivisatos, A. P. Coupling of optical resonances in a compositionally asymmetric plasmonic nanoparticle dimer. *Nano Lett.* **10,** 2655–2660 (2010).

11. A??imovi??, S. S., Kreuzer, M. P., Gonz??lez, M. U. & Quidant, R. Plasmon near-field coupling in metal dimers as a step toward single-molecule sensing. *ACS Nano* **3,** 1231–1237 (2009).

12. Hall, W. P., Ngatia, S. N. & Van Duyne, R. P. LSPR biosensor signal enhancement using nanoparticle-antibody conjugates. *J. Phys. Chem. C* **115,** 1410–1414 (2011).

13. Sonnichsen, C., Reinhard, B. M., Liphard, J. & Alivisatos, A. P. A molecular ruler based on plasmon coupling of single gold and silver nanoparticles. *Nat. Biotechnol.* **23,** 741–745 (2005).

14. Kneipp, K. *et al.* Single molecule detection using surface-enhanced Raman scattering (SERS). *Phys. Rev. Lett.* **78,** 1667–1670 (1997).

15. Nie, S. Probing Single Molecules and Single Nanoparticles by Surface-Enhanced Raman Scattering. *Science (80-.).* **275,** 1102–1106 (1997).

16. Michaels, A. M. & Brus, L. Ag Nanocrystal Junctions as the Site for Surface-Enhanced Raman Scattering of Single Rhodamine 6G Molecules. *J. Phys. Chem. B* **104,** 11965–11971 (2000).

17. Camden, J. P. *et al.* Probing the structure of single-molecule surface-enhanced Raman scattering hot spots. *J. Am. Chem. Soc.* **130,** 12616–12617 (2008).

18. Talley, C. E. *et al.* Surface-enhanced Raman scattering from individual Au nanoparticles and nanoparticle dimer substrates. *Nano Lett.* **5,** 1569–1574 (2005).

19. Maier, S. a. Waveguiding: The best of both worlds. *Nat. Photonics* **2,** 460–461 (2008).

20. Solis, D. *et al.* Turning the corner: Efficient energy transfer in bent plasmonic nanoparticle chain

waveguides. *Nano Lett.* **13,** 4779–4784 (2013).

21. Brown, L. V., Sobhani, H., Lassiter, J. B., Nordlander, P. & Halas, N. J. Heterodimers: Plasmonic properties of mismatched nanoparticle pairs. in *ACS Nano* **4,** 819–832 (2010).

22. Camargo, P. H. C., Cobley, C. M., Rycenga, M. & Xia, Y. Measuring the surface-enhanced Raman scattering enhancement factors of hot spots formed between an individual Ag nanowire and a single Ag nanocube. *Nanotechnology* **20,** 434020 (2009).

23. Liu, N., Hentschel, M., Weiss, T., Alivisatos, A. P. & Giessen, H. Three-Dimensional Plasmon Rulers. *Science (80-.).* **332,** 1407–1410 (2011).

24. Gandra, N., Abbas, A., Tian, L. & Singamaneni, S. Plasmonic Planet − Satellite Analogues : Hierarchical Self-Assembly of. *Nano Lett.* (2012).

25. Ross, B. M., Waldeisen, J. R., Wang, T. & Lee, L. P. Strategies for nanoplasmonic core-satellite biomolecular sensors: Theory-based Design. *Appl. Phys. Lett.* **95,** (2009).

26. Sebba, D. S., Mock, J. J., Smith, D. R., LaBean, T. H. & Lazarides, A. A. Reconfigurable core-satellite nanoassemblies as molecularly-driven plasmonic switches. *Nano Lett.* **8,** 1803–1808 (2008).

27. Yoon, J. H., Zhou, Y., Blaber, M. G., Schatz, G. C. & Yoon, S. Surface plasmon coupling of compositionally heterogeneous core-satellite nanoassemblies. *J. Phys. Chem. Lett.* **4,** 1371–1378 (2013).

28. Pierrat, S., Zins, I., Breivogel, A. & Sönnichsen, G. Self-assembly of small gold colloids with functionalized gold nanorods. *Nano Lett.* **7,** 259–263 (2007).

29. Xu, L. *et al.* Regiospecific plasmonic assemblies for in Situ Raman spectroscopy in live cells. *J. Am. Chem. Soc.* **134,** 1699–1709 (2012).

30. Hostetler, M. J., Templeton, A. C. & Murray, R. W. Dynamics of place-exchange reactions on monolayer-protected gold cluster molecules. *Langmuir* **15,** 3782–3789 (1999).

31. Beeram, S. R. & Zamborini, F. P. Selective attachment of antibodies to the edges of gold nanostructures for enhanced localized surface plasmon resonance biosensing. *J. Am. Chem. Soc.* **131,** 11689–11691 (2009).

32. Beeram, S. R. & Zamborini, F. P. Effect of protein binding coverage, location, and distance on the localized surface plasmon resonance response of purified Au nanoplates grown directly on surfaces. *J. Phys. Chem. C* **115,** 7364–7371 (2011).

33. Beeram, S. R. & Zamborini, F. P. Purification of gold nanoplates grown directly on surfaces for enhanced localized surface plasmon resonance biosensing. *ACS Nano* **4,** 3633–3646 (2010).

34. Zhu, T., Fu, X., Mu, T., Wang, J. & Liu, Z. pH-dependent adsorption of gold nanoparticles on p-aminothiophenol-modified gold substrates. *Langmuir* **15,** 5197–5199 (1999).

35. Jain, P. K., Huang, W. & El-Sayed, M. A. On the universal scaling behavior of the distance decay of plasmon coupling in metal nanoparticle pairs: A plasmon ruler equation. *Nano Lett.* **7,** 2080–2088 (2007).

36. Stroyer-Hansen, T. & N??rby Svendsen, E. Calculation of bond polarizability parameters of the benzene molecule. in *Journal of Molecular Structure* **410-411,** 349–352 (1997).

37. Hinchliffe, A., Mkadmh, A., Nikolaidi, B., Soscún, H. & Abu-Awwad, F. Enhancement of

molecular polarizabilities by the push-pull mechanism; a DFT study of substituted benzene, furan, thiophene and related molecules. *Open Chem.* **4,** 743–759 (2006).

38. Gole, A. & Murphy, C. J. Seed-mediated synthesis of gold nanorods: Role of the size and nature of the seed. *Chem. Mater.* **16,** 3633–3640 (2004).

39. Ochiai, T., Isozaki, K., Nishiyama, S. & Miki, K. Enhancement of self-assembly of large (>10 nm) gold nanoparticles on an ITO substrate. *Appl. Phys. Express* **7,** (2014).

40. Gabudean, A. M., Biro, D. & Astilean, S. Localized surface plasmon resonance (LSPR) and surface-enhanced Raman scattering (SERS) studies of 4-aminothiophenol adsorption on gold nanorods. in *Journal of Molecular Structure* **993,** 420–424 (2011).

Chapter 5: One-to-one correlation between structure and optical response in a heterogeneous distribution of plasmonic constructs*

5.1 Abstract

Assemblies of coupled plasmonic nanoparticles are used as sensors and rulers for the measurement of nanoscale distances and dynamic distance changes in biological and macromolecular systems. Since such rulers are employed at the single-device level, variations from one construct to another can greatly influence their reliability as sensors. In this work, we performed an experimental and simulation-based analysis of the structural and functional heterogeneity in model assemblies consisting of a Au nanosphere (NS) attached to a highly polarizable Au nanoplate (NP). The spectral characteristics, including the number, nature and energy position of plasmon modes varied significantly from one construct to another. The coupling-induced LSPR shift, which can be the optical readout for sensing applications, ranged over an order-of-magnitude across the set of constructs measured. By correlating scattering spectra with construct morphologies obtained from scanning electron microscopy (SEM) images for a large set of individual constructs, we determined that of all possible structural factors, the NS size was the largest contributor to the heterogeneity in the optical response. Small NSs resulted in spectra with a single LSPR mode, whereas large NSs resulted in complex spectra with multiple polarization-dependent LSPR modes. From the heterogeneous population of constructs, we were able to formulate, with the help of electrodynamic simulations, a systematic structure-property relationship, according to which the magnitude of the coupling-induced shift increases with an increase in the NS size, approaching saturation in the limit of large NS diameter. We discuss the theoretical basis and practical utility of this structure sensitivity in the construction of sensitive plasmon rulers, in the determination of the fidelity of individual ruler constructs, and in the development of new sensors for measuring optical polarizabilities of emitters.

* Reproduced with permission from: Fang, A.(co-first); White, S. L (co-first).; Masitas, R. A.; Zamborini, F. P.; Jain, P. K. One-to-one correlation between structure and optical response in a heterogeneous distribution of plasmonic constructs. *J. Phys. Chem. C* **119,** 24086–24094 (2015).

5.2 Introduction

Heterogeneity in structure and thereby in properties is a hallmark of nanostructured materials, like supported catalysts and nanoparticle-based optoelectronic devices.[1–8] Each nanoparticle in the sample can be sufficiently different from every other, in terms of shape, size, lattice/defect composition, or surface chemistry. Such variability is being mitigated by more controlled colloidal syntheses.[9,10] Nevertheless, heterogeneity is quite inevitable in complex nanostructures composed of closely-linked assemblies of nanoparticles.[11–15] In such constructs, there are significantly more structural degrees of freedom that can suffer from variations. In addition, the emergent properties of the assembly can be much more structure-sensitive. Self-assembled clusters of plasmonic nanoparticles, which show collective optical attributes such as magnetic plasmonic modes, provide a case in point.[16,17] As a specific example, small deviations (on the 0.5-2 nm scale) in the symmetry of the tetrahedral tetramer of Au nanoparticles can induce strong coupling between the electric mode and the dark magnetic mode of the assembly.[18] As a result of this symmetry-breaking, a Fano resonance is seen, which is otherwise missing in the symmetric structure.[16,19,20]

Apart from optical properties, function can also be affected by structural heterogeneities. The plasmon ruler is one such construct where heterogeneity can be detrimental to reliable function. In its simplest form, a plasmon ruler consists of a pair of spherical plasmonic nanoparticles that are electromagnetically coupled to one another.[21–23] The localized surface plasmon resonance (LSPR) of the coupled assembly has an energy position that depends on the strength of inter-particle coupling, which in turn depends near-exponentially on the distance between the two nanoparticles.[24–26] When the dependence of the LSPR energy position on distance is appropriately calibrated for a particular assembly, that assembly can be used to monitor distance changes occurring in molecules sandwiched between the two nanoparticles. The concept was first demonstrated by Alivisatos and co-workers by linking Au and Ag NSs with ss-DNA and monitoring in real-time distance changes and kinetics associated with DNA hybridization.[27] Since then, plasmon rulers have been applied for studying a range of biological processes,[28–31] including processes occurring within live cells.[31] A 3D version of the ruler proposed for studying the mechanics of protein folding has also been demonstrated.[32]

It is known that structural variables, such as the initial separation between the two nanoparticles, can strongly influence the LSPR energy shift, the primary readout of the sensor.[33,34] Even small variations in the morphology from one construct to another can lead to a variable readout of the distance change. Since plasmon rulers are typically used at single-device level, one cannot benefit by "averaging" out of these heterogeneities. The implications are even more severe for complex plasmon rulers that utilize multiple coupled anisotropic nanostructures for obtaining 3D spatial information, including distances and orientations.[15,32,35–38] The latter can suffer from variations in additional factors such as the relative placement

or orientation of the nanostructures in three dimensions. In many cases, the structural variables that most critically affect the LSPR response may not be fully known.

Here, we investigate, by single-particle studies, heterogeneities in complex constructs comprised of a Au nanosphere (NS) linked to the surface of a highly polarizable Au nanoplate (NP) sensor. Our aim was to identify the structural factors most critical to the potential function of the construct as an optical sensor or a 3D plasmon ruler, so that improved synthetic strategies may be developed for producing constructs that offer reproducible, reliable performance. Despite control of the key variables such as the interparticle separation and the location of linkage,[35] we found a wide spread in the spectral properties across a set of constructs investigated: some structures showed a single symmetric LSPR mode, whereas others showed complex multi-peaked spectra. By correlated examination of the scattering spectra and morphology from scanning electron microscopy (SEM) across several constructs and guidance from simulations, we determined that, of the many possible structural variables, NS diameter was the most critical factor dictating the spectral properties of the assembly. Across the set of constructs studied, there was a 15-fold variation in the coupling-induced energy shift. But when this energy shift was correlated construct-by-construct to the NS diameter obtained from SEM, we uncovered a systematic trend, as per which the shift increases with an increase in the NS diameter approaching saturation in the limit of large NS diameters. We discuss the theoretical and practical implications of this finding. This work shows that heterogeneity can be an inherent feature of functional plasmonic devices that needs detailed characterization and eventual mitigation. Structure-property relationships determined by careful single-particle studies can help achieve the latter goals.

5.3 Results and discussion

We constructed model assemblies by attaching a Au NS to the surface of a Au NP (Fig. 5.1A and 5.1B). The Au NP is a highly polarizable, strongly scattering nanostructure, ideal for use in a plasmon sensor or ruler. All of the NPs investigated were hexagonal, truncated triangular, or circular-shaped, of a relatively similar size (~110 nm wide x ~35 nm thick), and exhibiting a single-peaked scattering spectrum. The attachment of the NS, when properly optimized, leads to considerable alteration of the LSPR spectrum of the NP. Fig. 5.1D shows the scattering spectra of several assembled NP/NS constructs measured by darkfield spectroscopy, a well-established method. The scattering spectrum of the corresponding NP before NS attachment is shown for comparison in each case. A large red-shift is seen in the dipolar LSPR mode of the NP as a result of strong coupling with the NS. In an actual plasmon ruler application, these spectral changes, particularly the large LSPR red-shift can serve as the optical readout for measuring distance

changes occurring in the molecular linker of the NP/NS dimer. In these model studies, we used 4-aminothiophenol (4-ATP) as the linker between the NP and NS (Section 5.5.1). The binding-induced LSPR red-shift is thus an optical readout for a distance change from ∞ to 1 nm, the approximate length of 4-ATP. The magnitude of this readout can be used for quantitative comparison of the sensor response of individual constructs, for application in plasmon rulers and coupling-based sensors.[39–42]

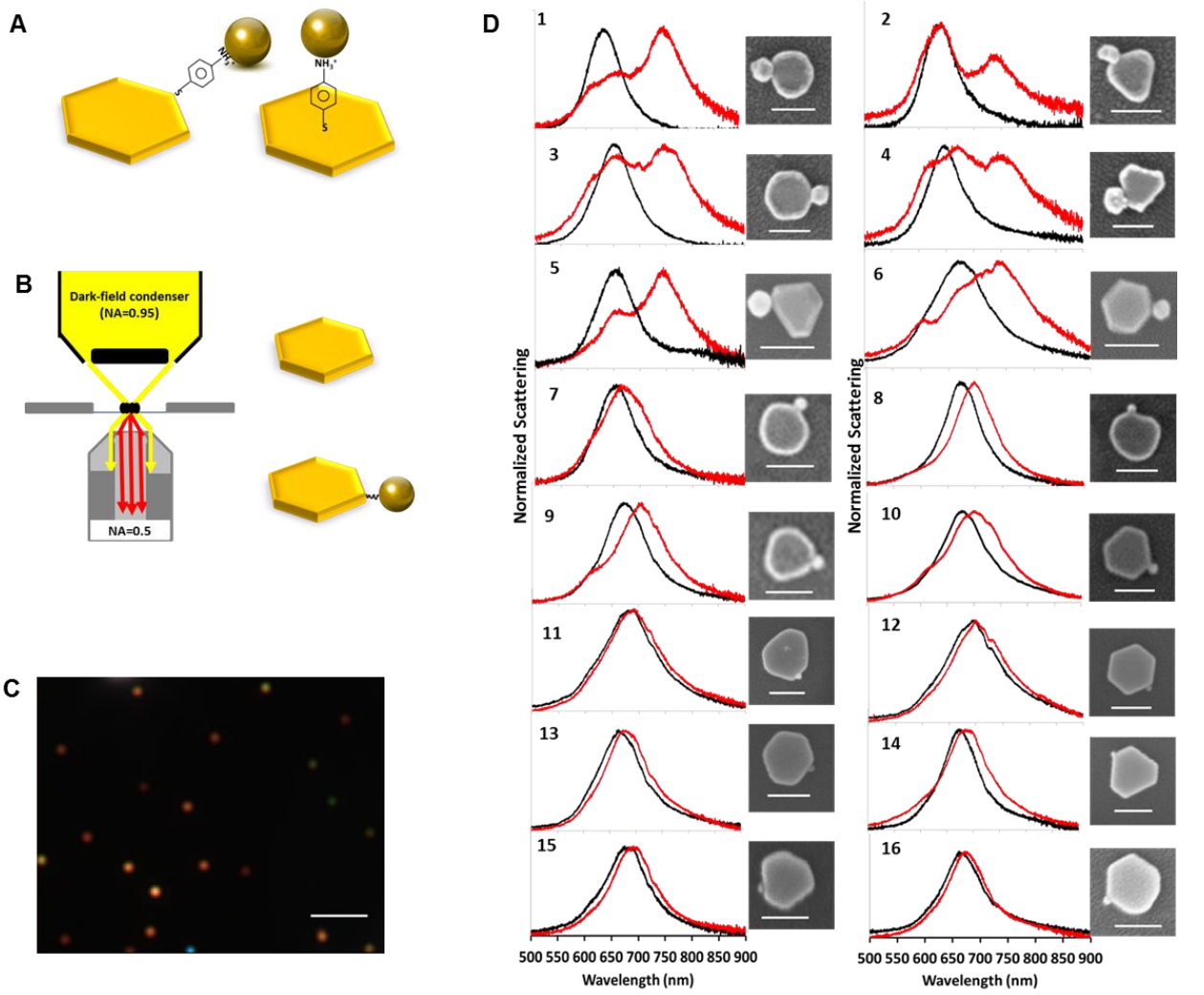

Figure 5.1 Construction and optical characterization of individual constructs comprised of NP/NS dimers. *(A) First, NPs were synthesized on a glass substrate using a method optimized to have an area density for addressing individual NPs. Then, using ligand place-exchange reactions, a NS is attached regioselectively either to a vertex on the side of the NP (left) or on the terrace of the NP (right). Schematic is not to scale. (B) The principle of transmission darkfield optical microscopy (left) used for characterizing a single NP (right, top) and a coupled NP/NS dimer (right, bottom). (C) Representative dark-field scattering image of several single Au NPs on a glass slide. (D) Scattering spectra of 16 single Au NPs before (black line) and after (red line) attachment of a Au NS on a vertex site, as shown in corresponding SEM images to the right. Scale bars are 100 nm in all SEM images and 5 μm in the dark-field image. The scattering intensity of the NS is much weak weaker than that of the NP and therefore the NS LSPR mode does not contribute to the overall scattering spectrum of the dimer.*

Since the attachment location can influence the spectral characteristics of the construct, we also controlled the placement of the NS (Fig. 5.1A) by means of a previously-developed regioselective ligand-directing strategy.[35] In this case (Fig. 5.1D), the NS was attached to the side edges of the NP in all constructs. Despite

the structural control dictated by our construction method, we saw heterogeneity in the spectral properties of the constructs investigated. Considerable variation was seen in the number and position of LSPR modes from one construct to another. It is quite clear that such a variable spectrum cannot be used reliably as a readout in a sensor, which makes it necessary to identify the source of the heterogeneity. The heterogeneity in optical response could be a result of dimer-to-dimer variations in i) the ligand shell and thereby the interparticle distance, ii) the precise location of the NS on the edge and its relative placement with respect to the plane of the NP, iii) the size or shape of the NP, iv) the size or shape of the NS, or other factors. We therefore examined the morphology of each one of the constructs using SEM imaging. While resolution of finer morphological variations (such as small differences in the NS/NP interparticle distance) is difficult using SEM, it was quite clear from the SEM images that the size of the NS in the construct varied from one construct to another. Such size variations are inherent even in size-controlled syntheses (Section 5.5.1). In fact, in Reinhard's work, whereas rulers constructed from nominally "40 nm" diameter NSs showed high reliability, those constructed from NSs of nominally "80 nm" diameter, albeit with a large spread of ~12 nm, showed significant heterogeneities.[25] Therefore, we decided to investigate if NS size variability was primarily responsible for the heterogeneity in optical response.

In order to explore a large size regime, we combined data obtained using three different NS syntheses (Section 5.5.1). In our survey of 16 constructs (see Table 5.1 and Fig. 5.1D), we identified four distinct types of behavior:

Class I: Some constructs (e.g., #7, #11, #12, #13, #14, #15, #16) exhibited a single LSPR mode, marginally red-shifted relative to the LSPR mode of the isolated NP.

Class II: Other constructs (e.g., #8, #9, #10) exhibited an LSPR mode considerably red-shifted relative to the mode of the isolated NP. In addition, a new mode, absent in the single NP, was seen in the form of a shoulder in the 600-nm region.

Class III: A third class (e.g., #2, #5) exhibited two modes: a strongly red-shifted LSPR mode and another mode coincident with the isolated NP mode.

Class IV: Some constructs (e.g., #1, #3, #4, #6) exhibited complex spectra with three modes. The lowest energy mode is considerably red-shifted from that of the isolated NP, e.g. for construct #4, the red-shift ($\Delta\lambda_{max}$) is as large as 111 nm. In addition, there exists another mode with a smaller magnitude of red-shift ($\Delta\lambda_{max}$ = 27 nm) as well as a peak in the 600 nm region.

From this library of paired scattering spectra/SEM image data, it appeared that the constructs with the smallest NSs exhibited remarkably differently spectral properties from those built from the largest-sized NSs. To test this apparent correlation between NS size and the spectral features of the dimer assembly, we used electrodynamic simulations performed using the discrete-dipole approximation (DDA) method, as

described in Section 5.5.2. The simulated scattering spectrum of the assembly indeed showed a systematic dependence on NS size (Fig. 5.2A).

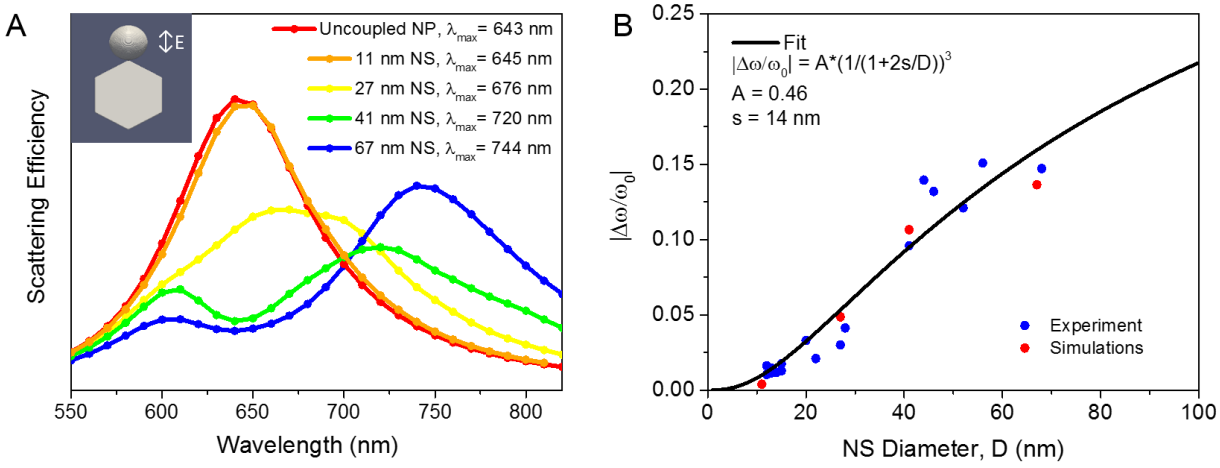

Figure 5.2 Spectral properties of the construct depend strongly on NS size. *(A) DDA simulations show that attachment of a NS to the vertex of the NP red-shifts the dipolar LSPR mode (orange, yellow, green and blue data-points connected by a spline) of the NP relative to the LSPR of a NP with no NS (red data-points connected by a spline). The magnitude of the red-shift increases with increasing NS diameter and for all but the smallest NS diameter, also results in the emergence of a quadrupole resonance in the 600-nm region. The inset shows the simulated configuration for a 67 nm diameter NS at the NP vertex. (B) The fractional energy shift ($|\Delta\omega/\omega_0|$) of the dipolar resonance for each coupled NP/NS pair is plotted versus the diameter of the attached NS. The simulated data from Fig. 5.2A is plotted in red and the experimental data from Fig. 5.1D is plotted in blue. The black curve is a least-squares fit to $y = A(1/(1 + (2s/x))^3$ with R^2 = 0.93. Simulations were performed as described in Section 5.5.2. The incident field was linearly polarized along the interparticle axis. The simulated scattering spectra were fit to two Voigt functions (high-energy quadrupole and low-energy dipole) where necessary. The spectra of the uncoupled NP and the NP with the 11 nm NS, which did not display a quadrupole mode, were fit to one Voigt function. The λ_{max} indicated corresponds to that for the dipolar resonance. The experimental $|\Delta\omega/\omega_0|$ values corresponding to the spectra in Fig. 5.1D were obtained with unpolarized light excitation.*

In simulations, constructs with a NS as small in diameter as 11 nm showed a single LSPR mode (orange line), red-shifted only marginally ($\Delta\lambda_{max}$ = 2 nm) relative to the LSPR of the isolated NP (red line). Class I behavior observed experimentally thus appears to be a result of small NS size. When the NS diameter was increased to 27 nm (yellow line), the magnitude of the red-shift increased by more than an order of magnitude. In addition, a weak shoulder emerged in the scattering spectrum in the 600 nm region. These simulations reproduce Class II behavior seen in the experiments. With further increase in the NS size, the magnitude of red-shift increased even further and the blue mode became strong enough to be resolved as a separate peak. For instance, a simulated construct with a 67-nm diameter NS (blue line) showed a red-shift of about 100 nm and the presence of a distinct high energy LSPR mode. Thus, not one but two optical

readouts, i.e., peak splitting and large LSPR red-shift, are available in these assemblies. Secondly, the larger the diameter of the NS, the larger is the magnitude of these two readouts.

In order to explain the peak splitting into two distinct modes seen in constructs with a larger NS, we examined the near-field profile for both these modes under excitation polarized along the inter-particle axis (‖). Fig. 5.3 shows the result of such an examination for a construct with a 67-nm diameter NS attached to a vertex of the NP. From a vector plot of the induced field, the low energy mode (λ_{max} = 740 nm) can be assigned to a dipolar LSPR mode of the coupled NP/NS construct. In this mode, the dipolar oscillation of the NP is coupled with the dipolar mode of the NS via a bonding interaction. As a result, the resonance of the dimer appears at a considerably lower energy compared to the isolated NP LSPR mode. On the other hand, the higher energy mode (λ_{max} = 600 nm), field vector plots show, is the result of an excitation of a quadrupole-like mode in the NP induced by the NS. An isolated NP does not show such a quadrupolar mode, which is typically spectrally forbidden. But the inhomogeneous electric field resulting from the proximity to the excited NS can induce such an excitation in the NP. The larger the size of the NS, the larger is the inhomogeneity of the near-field of the NS extending across the NP, and the greater is the strength of the quadrupolar excitation within the NP.

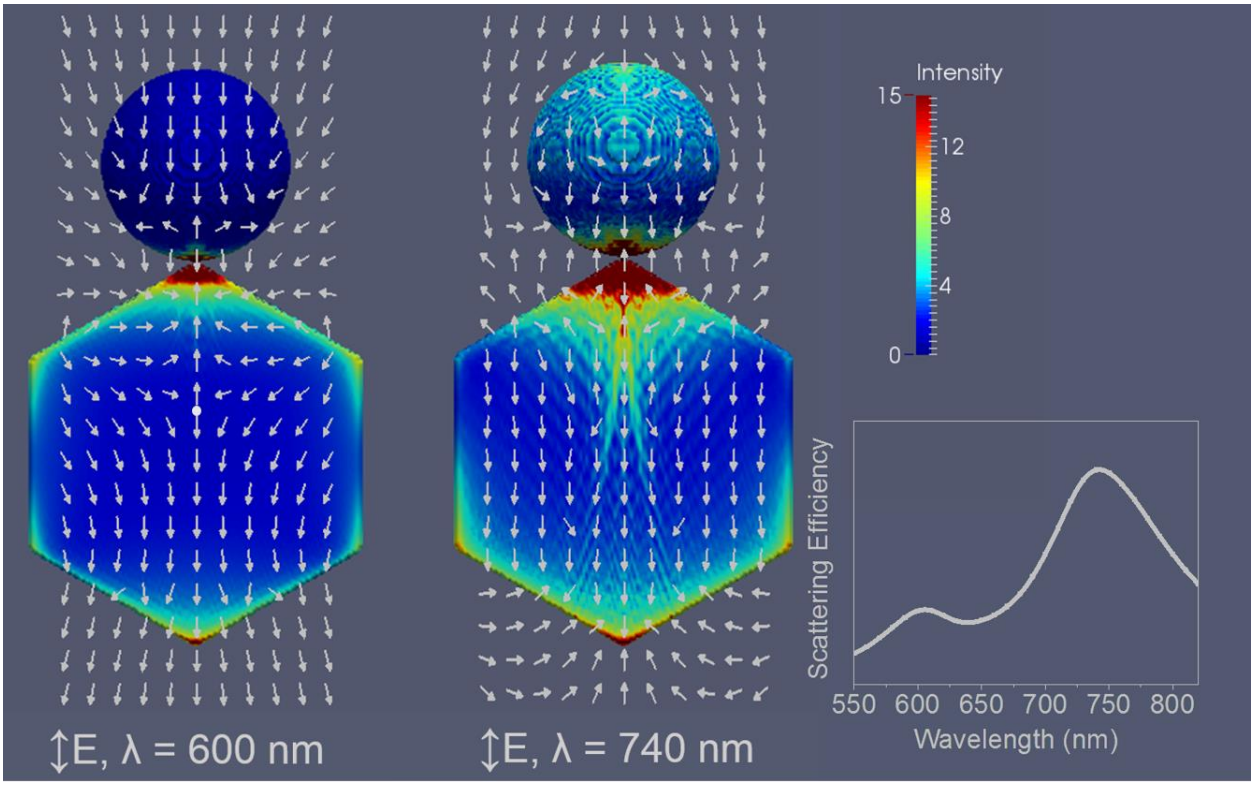

Figure 5.3 Assignment of plasmonic modes in a construct consisting of a Au NP with a 67 nm Au NS attached to its vertex. *The simulated near-field over the surface of the nanostructure is depicted in the form of an amplitude enhancement ($|E|/|E_0|$) on a color scale. As an overlay, vector directions of the induced electric field (indicated by arrows) in the plane of the hexagon passing through the center of the NP are shown. The scattering spectrum for the NP/NS construct, shown at the bottom right, exhibits two modes centered at λ_{max} = 740 nm and 600 nm. Under 740 nm excitation, the nanostructure exhibits a dipolar mode with the oppositely charged poles located at the opposite vertices of the NP. Under 600 nm excitation, a quadrupole-like mode is seen where two anti-parallel dipoles originate at a location (shown by white dot) within the NP. Simulations were performed as described in Section 5.5.2. The incident field was linearly polarized along the interparticle axis.*

In order to explain the multi-peaked spectra seen for several constructs, we had to consider that in darkfield spectroscopy, the excitation is unpolarized. Experimental spectra must contain a combination of modes polarized along different axes of the NP/NS dimer. In simulations wherein light was polarized perpendicular to the interparticle axis (⊥), the construct with the 67 nm NS (Fig. 5.8) showed a single LSPR peak nearly identical to the isolated NP LSPR, except for a marginal red-shift ($\Delta\lambda_{max}$ = 3 nm). Under this polarization condition, the dipolar oscillations of the NP and the NS are oriented side-by-side and interact only weakly. The small red-shift results from the effect of electromagnetic retardation because NS attachment leads to an increase in the overall size of the nanostructure.

When modes from the two orthogonal polarizations (∥ and ⊥) are considered in unison, one can explain the multi-peaked spectra of Class IV constructs (Fig. 5.1D: #1, #3, #4, #6). The spectra contain three modes. The lowest energy mode is a dipolar mode, considerably red-shifted from the isolated NP LSPR due to strong NP/NS coupling. The highest energy mode is a quadrupolar excitation. The intermediate energy mode is the one excited by light polarized perpendicular to the interparticle axis, red-shifted only slightly from the isolated NP LSPR. Multiple peaks (Class IV) are seen only with larger NSs. With smaller NSs, the dipolar mode from ∥ excitation is red-shifted by a magnitude small enough such that it is closely overlapped with the mode from ⊥ excitation. The quadrupolar mode is also much weaker. This is why a multi-peaked spectrum is not seen in Class I and II constructs.

Simulating darkfield scattering spectra via a combination of two orthogonal polarization conditions, while informative, is simplistic in at least one regard. The throughput of the grating spectrometer is sensitive to the polarization of the collected light.[43] As a result, the relative contribution of the scattering signal polarized along different axes is expected to depend on the orientation of the NP/NS dimer relative to the grating axes. For suitably oriented constructs, therefore, the scattering mode from ⊥ (∥) excitation can have a much greater (lower) contribution in the overall spectrum. Class III behavior seems to be a result of such an effect, wherein the quadrupolar mode appears extremely weak, almost indiscernible in comparison to the ⊥-polarized mode. Therefore, only two bands appeared in the acquired spectrum, one close to the isolated NP LSPR and the other considerably red-shifted.

With the heterogeneity in spectral attributes fully explained, we provide a quantitative analysis of the optical response across the entire set of constructs (Fig. 5.2B). The metric we used was the amount by which the lowest energy mode red-shifted upon NS attachment. To account for variations in the LSPR position before NS attachment, the magnitude of the red-shift in energy units ($|\Delta\omega|$) was normalized by the energy ω_0 of the isolated NP LSPR. This fractional energy shift, $|\Delta\omega/\omega_0|$, varied over a large range from 0.01 to 0.15 across the constructs investigated, indicating a 15-fold range in the magnitude of the optical readout. However, when $|\Delta\omega/\omega_0|$ was plotted against the NS diameter determined from SEM for each construct, a systematic trend emerged (blue data-points). As per this trend, $|\Delta\omega/\omega_0|$ increases with increasing NS diameter, but the effect saturates at large NS diameters. Simulation results, shown by red data-points, follow a matching trend. The close agreement between the trend followed by the experimental data from the heterogeneous population of constructs and the NS size-dependence predicted by simulations indicates that NS diameter is the primary structural factor responsible for spectral heterogeneity. It must be noted, however, that there are some local deviations of the experimental data-points from the simulated trend, suggesting that variables other than the NS diameter play a role, even though the overall trend is most reflective of a NS diameter dependence. Possibly, these other factors are controlled more tightly in our synthetic strategy or these

factors do not affect plasmon coupling as sensitively as the NS diameter. Nevertheless, the systematic role of factors other than NS diameter may need further investigation.

The size-dependent trend seen in the heterogeneous collection of constructs was found to follow a simple physical model. As per this model, the fractional shift, which is a measure of the strength of plasmon coupling in the NP/NS dimer, depends directly on the electric near-field of the NS experienced by the NP.[25] Considering only the dipolar excitation of the NS and ignoring the perturbation of the NS LSPR by the NP, the near-field due to the excited NS has an amplitude:[44,45]

$$E_{NS} = \frac{\alpha_{NS}}{4\pi\varepsilon_0 r^3} E_0 \quad (1)$$

at a point at a distance *r* from the center of the NS along the polarization direction. E_0 is the magnitude of the incident field amplitude and ε_0 is the vacuum permittivity. Note E_{NS} does not include the contribution of the uniform incident field.[54] α_{NS} is the frequency-dependent polarizability of the NS given by:[45]

$$\alpha_{NS}(\omega) = 3\varepsilon_0 V \frac{(\varepsilon(\omega)-\varepsilon_m)}{(\varepsilon(\omega)+2\varepsilon_m)} \quad (2)$$

where *V* is the volume of the NS, ε_m is the dielectric constant of the medium, and $\varepsilon(\omega)$ is the complex frequency-dependent dielectric function of Au. Combining (1) and (2) yields:

$$\frac{E_{NS}}{E_0} = A\left(\frac{D}{D+2s}\right)^3 = A\left(\frac{1}{1+2s/D}\right)^3 \quad (3)$$

where $A(\omega) = \frac{(\varepsilon(\omega)-\varepsilon_m)}{(\varepsilon(\omega)+2\varepsilon_m)}$ is the near-field amplitude at the NS surface, *D* is the diameter of the NS, and *s* is the distance from the surface of the NS, i.e., $s = r - D/2$. When the experimental and simulated data in Fig. 5.2B was fit to the expression in eq. (3), good agreement with $R^2 = 0.93$ was obtained (black line). The fit parameter *s*, with a value of 14 ± 3 nm, represents an effective distance of coupling between the NS and the NP. Although the surface of the NP is only 1 nm away from the NS surface, the effective separation is larger due to the finite size of the NP, i.e., parts of the NP extend significantly beyond a distance of 1 nm from the surface of the NS. As a result, the NP experiences, averaged over its span, an electric field that is equivalent in magnitude to the magnitude of the near-field at an effective distance, *s*, of 14 nm from the excited NS surface.

Eq. (3) provides a physical origin for the size-dependent trend followed by the experimental data. With increasing NS diameter *D*, the polarizability of the NS and therefore the strength of its near-field at a fixed distance from its center increases as D^3. At the same time, the increase in NS diameter results in the NP becoming more distant from the center of the NS. Due to the combination of these two effects, the strength of NP/NS coupling (indicated by $|\Delta\omega/\omega_0|$) increases with an increase in the NS diameter, eventually

saturating at large NS diameters ($D >> s$), where the near-field amplitude experienced by the NP reaches a limiting value:

$$\frac{E_{NS}}{E_0} = A\left(\frac{D}{D+2s}\right)^3 \approx A \quad (4)$$

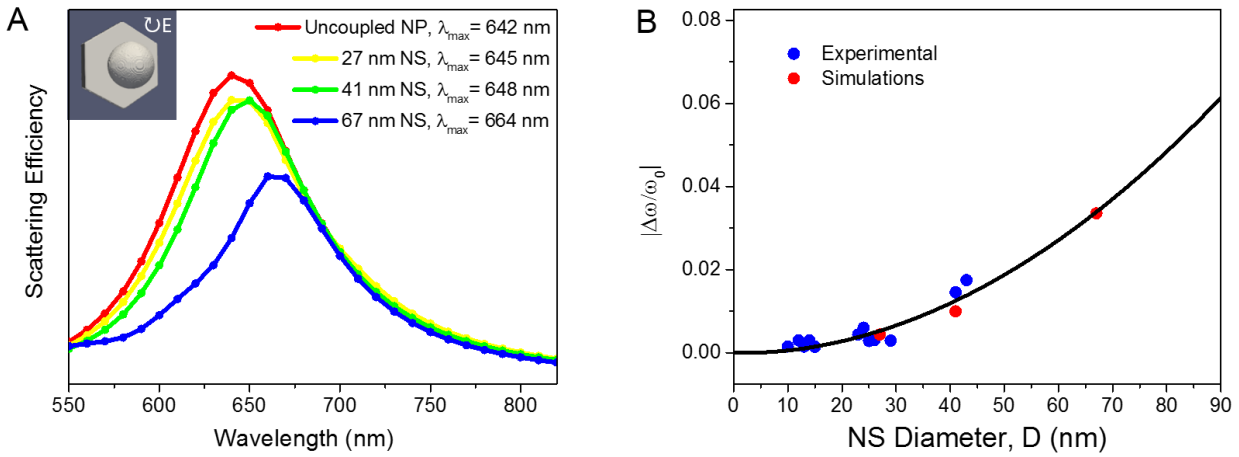

Figure 5.4 Plasmonic coupling in a NP/NS construct with the Au NS attached to the terrace. *(A) DDA simulations show that attachment of a NS to the terrace of the NP red-shifts the dipolar LSPR mode (orange, yellow, green and blue data-points connected by a spline) of the NP relative to the LSPR of a NP with no NS (red data-points connected by a spline). The magnitude of the red-shift increases with increasing NS diameter. The inset shows the simulated configuration for a 67 nm diameter NS placed at the center of the NP terrace. (B) The fractional energy shift ($|\Delta\omega/\omega_0|$) of the resonance for each coupled NP is plotted versus the diameter of the attached NS. The simulated data from Fig. 5.4A is plotted in red and the experimental data from Fig. 5.5 is plotted in blue. The black curve is a guide for the eye. Simulations were performed as described in Section 5.5.2. For the simulations, interparticle surface-to-surface spacing was 1 nm and the incident field was unpolarized.*

Similar studies were performed for constructs where the NS was attached to the terrace of NP. In this geometry, attractive coupling between the NS and NP through the induction of an image dipole on the NP surface leads to a red-shift of the NP LSPR mode.[35] Experimental scattering spectra for 13 such constructs (Fig. 5.5, Table 5.2) indicate significant heterogeneity in the spectral properties of the constructs. While all constructs exhibited only a single LSPR mode, the LSPR red-shift relative to the isolated NP was variable from one construct to another. Examination of the SEM images of individual constructs indicated a correlation between the magnitude of the red-shift and the NS size. DDA simulations verified this apparent correlation, as seen in Fig. 5.4A. The fractional energy shift, $|\Delta\omega/\omega_0|$, of the investigated constructs ranged over an order of magnitude (see Table 5.2), but when this fractional shift was plotted against the NS diameter determined by SEM in each case, the data (Fig. 5.4B, blue data-points) followed a super-linear

trend, similar to that predicted by simulations (Fig. 5.4B, red data-points connected by black line). The close agreement between the experimental data and the trend predicted by simulations indicates that NS diameter is the primary structural variable in this geometry too.

5.4 Conclusion

We showed that complex nanoparticle assemblies, with potential applications in plasmon rulers and sensors, can exhibit significant heterogeneities in morphology and thereby in the spectral response from one individual construct to another. Individual constructs prepared by controlled attachment of a NS to a NP showed marked variations in their scattering spectra, the optical readout for sensing applications. Correlation of structural morphologies and LSPR spectra across multiple constructs revealed that the NS size was the primary structural variable that dictated the spectral properties. Small NSs resulted in spectra with a single LSPR mode, whereas large NSs resulted in complex spectra with multiple LSPR modes. The optical response, quantified by the coupling-induced plasmonic shift, varied over an order of magnitude across the set of constructs investigated. But when the magnitude of the response was correlated with the NS diameter obtained from SEM images, a systematic trend was seen. An increase in the NS size results in an increase in the magnitude of the optical readout, an effect that approaches saturation at very large NS sizes.

In addition to structural parameters that are known to be critical, like the interparticle distance and the location of the NS, there must also be tight control on the NS size for obtaining reliable sensing performance from individual assemblies used as sensors or rulers. From the trend seen here, it seems possible to construct highly effective sensors and rulers by using NSs of size on the order of 100 nm. Nevertheless, this high sensitivity will come at the cost of a complex optical readout consisting of multiple polarization-dependent modes that may vary in strength depending on the orientation of the construct. This work shows that through single-particle measurements, one can learn, even from a heterogeneous population of constructs, meaningful structure-function relationships that are otherwise obscured in ensemble studies. The trend that emerged in our single-particle studies, modeled by eq. 3, shows that the energy shift of the NP LSPR is highly sensitive to the polarizability of the attached nanostructure. Thus, in addition to serving as plasmon ruler components, Au NPs could allow the measurement of optical polarizabilities of molecules, quantum dots, and nanoparticles attached to their surfaces.

5.5 Methods

5.5.1 Experimental methods

Chemicals. Citric acid trisodium salt, L-ascorbic acid, sodium borohydride, cetyltrimethylammonium bromide (CTAB), mercaptopropyltrimethoxysilane (MPTMS), 1-hexanethiol (HT), 4-aminothiophenol (4-ATP), hydrogen peroxide, 2-propanol, ethyl alcohol, and acetone were purchased from Sigma-Aldrich. $HAuCl_4.3H_2O$ was synthesized from metallic Au.

Synthesis of Au nanoplates (NPs) directly on glass. Au NPs were synthesized directly on glass substrates using our previously described seed-mediated growth procedure procedure[46] with some modifications to achieve optimal density and size of Au NPs for obtaining single particle scattering spectra.[35] The as-prepared sample consists of Au nanospheres (NSs) and triangular, hexagonal, or circular Au nanoplates (NPs). We purified the sample to contain >90% Au NPs by removing NSs through sonication, as described previously. Prior to Au NP synthesis, numeric labels were etched onto the glass substrates by photolithography. These numeric labels were used as makers to correlate optical images and spectra with scanning electron microscopy (SEM) images of individual constructs, as described later.

Synthesis of Au nanospheres (NSs) in solution. Au NSs of ~4 nm used in this procedure were synthesized following the protocol of Murphy and co-workers [47] as described previously.[35] Citrate-stabilized Au NSs with a target diameter of ~25 nm were prepared by adding 10 mL of a 1% trisodium citrate solution to 100 mL of a boiling 2.5 x 10^{-4} M $HAuCl_4.3H_2O$ solution. The mixed solution was kept stirring and boiling for 1 h, after which it was cooled to room temperature. Stirring was continued until use. Quasispherical, citrate-stabilized Au NSs with target diameters of ~51 nm and ~13 nm were synthesized by the procedure of Wang and coworkers.[48] Briefly, 100 μL (for the 51 nm size) or 20 μL (for the 13 nm size) of 1 wt % $HAuCl_4 \cdot 3H_2O$ was added to an aqueous solution containing 4.90 mL of nanopure water. Next, 25 μL of 1 wt % trisodium citrate was added into the solution under stirring. Then 5 mL of 30 wt % H_2O_2 was injected followed by immediate addition of 10 μL (for the 51 nm size) or 20 μL (for the 13 nm size) of 4 nm diameter Au seeds.

Attachment of Au NSs to Au NPs supported on glass. We attached citrate-coated Au NSs selectively to either the sides or terraces of Au NPs using thiol self-assembly and ligand place-exchange reactions,[49] as described previously by our group.[35] For selective attachment to the side edges of NPs, we first assembled a monolayer of hexanethiol (HT) on the Au NP surface by placing the sample in 1 mM HT overnight. After rinsing thoroughly with ethanol, we exchanged HT ligands with 4-ATP by immersing the sample in a 6 mM ethanolic solution of 4-ATP for 1 h. Then the sample was subject to a solution of Au NSs. Under acidic conditions, the terminal NH_3^+ groups of 4-ATP can electrostatically bind the negatively-charged surface of a citrate-stabilized Au NS.[50] To ensure robust attachment of 4-ATP molecules to a Au NS, the pH value of

the Au NS solution was maintained at 4.8 for all experiments. Since the edges of Au NPs have lower steric hindrance, 4-ATP ligands bind most preferentially to the edges of the Au NPs in the place exchange step. Consequently, Au NSs, which bind to the 4-ATP ligands, get selectively attached to the edge sites of the NPs. For selective attachment of NSs to terrace sites, we performed the ligand exchange reactions in reverse order. In this case, 4-ATP ligands were first assembled onto the Au NPs and then place-exchanged with HT ligands. The ligand exchange occurs preferentially at the edges, which leads to blocking of those regions from Au NS attachment. As a result, terrace sites with lower prevalence of HT ligands are more likely to have Au NSs attached.

Dark-field light scattering imaging and spectroscopy. Dark-field imaging and spectroscopy were performed on an inverted Nikon Eclipse Ti microscope equipped with a halogen lamp light source and a dark-field condenser (N = 0.95-0.80) for sample illumination. A 100x variable-aperture, oil-immersion objective (N = 0.5-1.3) was used for collecting the scattered light from individual NPs or individual NP/NS dimers supported on the glass substrate. High-resolution dark-field images were obtained with an Infinity camera from Lumenera Corporation. These images were employed for selection of individual scatterers, from which resonant Rayleigh dark-field scattering spectra were collected using a multichannel air-cooled CCD camera coupled to a Horiba XPLORA-Inv confocal Raman spectrometer.

Scanning electron microscopy (SEM) imaging. SEM images of nanostructures supported on glass substrates were obtained at different magnifications on a Carl Zeiss SMT AG SUPRA 35VP field-emission SEM, equipped with an in-lens ion annular secondary electron detector, operating at a voltage of 8.00 kV. Prior to SEM imaging, the glass sample was mounted in a PS2 Sputtering Unit from International Scientific Instruments and sputter-coated with a 1-2 nm layer of Pt in order to increase the conductivity of the sample. The coating thickness was controlled by adjusting the coating time and current parameters of the sputterer. Optimal coating was achieved with a 1 min coating time at a 5 mA current.

5.5.2 Computational methods

Discrete-dipole approximation (DDA) simulations. The DDA method was used for the simulation of the optical properties of Au NPs and coupled NP/NS constructs. The DDA method numerically solves Maxwell's equations for one or a series of arbitrarily shaped objects by discretizing each object into a cubic array of N polarizable point dipoles and self consistently solving for the polarizability of each dipole interacting with the incident electromagnetic field and all other N-1 dipoles. The DDA method was implemented using the open source DDSCAT 7.3.0 code from Draine and Flatau.[51]

Nanostructure targets for simulation were generated via tools available on nanoHUB.org. The hexagonal geometry was generated using the nanoDDSCAT+ tool (DOI: 10.4231/D3MS3K28K), which takes a shape

input in the form of a triangulated mesh and converts it into a cubic array of points, the input for DDSCAT. Coupling in the NP/NS construct was simulated by attaching a NS to either a vertex or terrace of the NP target. Au NSs of various diameters (11 nm, 27 nm, 41 nm, and 67 nm) were generated using the DDSCAT subroutine CALLTARGET and combined with the NP target. For every case, the surface-to-surface separation distance between the NP and the NS was 1 nm, i.e., the NS was in contact with the ligand shell, which is the likely scenario in experiments. For NS attachment at the vertex, a 1 nm thick layer of HT (n =1.448)[52] was added to the surfaces of the top and bottom terraces of the NP and a 1 nm thick layer of 4-ATP (n =1.663)[53] was added to the surfaces of the side faces. To simulate experimental conditions, the NS, when smaller in diameter compared to the NP thickness, was placed with its center lying in the plane of the hexagon passing through the center of the NP. In the case of a NS larger in diameter compared to the NP thickness, the placement was offset such that both the NP and NS were in contact with the underlying substrate. For NS attachment to the NP terrace, a 1 nm thick layer of HT (n =1.448) was added to the surfaces of the side faces and a 1 nm thick layer of 4-ATP (n =1.663) was added to the surfaces of the top and bottom terraces. The NP was placed at the center of the terrace surface.

Excitation of the target was performed with a plane wave, incident normal to the face of the NP, propagating along the thickness of the NP. The excitation in darkfield scattering spectroscopy is thought to be unpolarized. Nevertheless, target structures were excited with (i) unpolarized light, simulated by a circularly polarized plane wave, (ii) with linearly-polarized light with a polarization parallel to the dimer interparticle axis, and/or (iii) with linearly-polarized light with a polarization perpendicular to the dimer interparticle axis, on a case-to-case basis. In all simulations, the refractive index of the ambient medium was set at n_m = 1.1, representative of a mixture of air ($n \approx 1$) and glass ($n \approx 1.5$). The relative contribution of air and glass was determined by the relative volume fraction of each within the surrounding medium, the surrounding medium being defined as the additional volume when the NP dimensions were extended 50% from the center of the NP along each axis. The bulk experimental dielectric function of Au from Johnson and Christy was utilized for all calculations without any corrections.[54]

Scattering spectra (scattering efficiency vs. wavelength) were obtained from each simulation. Spectra were plotted in energy units (eV) and then fit in OriginLab to single or multiple Voigt functions, as noted. From energy maxima (ω_{max}) obtained from fitting of dimer spectra, we determined the coupling-induced red-shift ($|\Delta\omega_{max}|$) and the fractional energy shift ($|\Delta\omega_{max}|/\omega_0$) of the dimer LSPR mode with respect to the LSPR frequency of the isolated NP (ω_0). When spectra exhibited both a dipolar resonance and a higher energy multipolar resonance, both resonances were fit to Voigt functions, but the fractional energy shift refers to the shift of the lower energy dipolar resonance only.

For one of the dimer constructs, i.e., a NP coupled with a 67-nm NS placed at the vertex, near-field calculations were also performed. For these field simulations, the incident electric field E_0 was polarized along the interparticle axis and the excitation wavelength was set to either 740 nm or 600 nm, corresponding to the λ_{max} of the dipole and quadrupole LSPR modes of the dimer, respectively. The near-field calculations utilized the DDSCAT 7.3 subroutine NEARFIELD. With the incident field amplitude $|E_0|$ set to a value of 1, the macroscopic field amplitude $|E|$ at each grid-point of a volume surrounding the nanostructure was obtained. Near-field enhancements ($|E|/|E_0|$) across the surface of the nanostructure were plotted using the open source application ParaView.

Two-dimensional plots of the vector direction of the induced electric field ($E - E_0$) across the NP/NS construct were also generated. The vector direction of the real component of the induced field in the plane of the hexagon was determined by the atan2 function in OriginLab as:

$$\theta = \text{atan2}(\{\text{Re}(E_Z) - E_0\},\text{Re}(E_Y))$$

where E_Y and E_Z represent the total field amplitude along the interparticle axis and that perpendicular to the interparticle axis, respectively. Re denotes the real part. The vector direction (θ) of the induced field at each grid-point in the plane of the hexagon passing through the center of the NP was depicted by an arrow. The magnitude of the induced field was not represented in these plots.

5.6 Additional figures

Table 5.1 *Localized surface plasmon resonance (LSPR) frequencies and scanning electron microscopy (SEM) images of 16 representative constructs consisting of a Au nanoplate (NP) with a Au nanosphere (NS) attached on the edge.*

	Initial ω_{max} (eV)	Final ω_{max} (eV)	Red-shift (eV)	Fractional Energy Shift	NS Size (nm)	Morphology
1	1.9494	1.6553	0.2941	0.1509	56	
2	1.9525	1.6800	0.2725	0.1396	44	
3	1.9045	1.6531	0.2514	0.1320	46	
4	1.9282	1.6444	0.2839	0.1472	68	
5	1.8987	1.6687	0.2300	0.1211	52	
6	1.8533	1.6755	0.1778	0.0959	41	
7	1.8987	1.8588	0.0399	0.0210	22	
8	1.8423	1.7814	0.0609	0.0330	20	
9	1.8423	1.7662	0.0761	0.0413	28	
10	1.8287	1.7737	0.0549	0.0300	27	
11	1.8206	1.7995	0.0211	0.0116	13	
12	1.7943	1.7712	0.0231	0.0129	15	
13	1.8533	1.8233	0.0300	0.0162	12	
14	1.8368	1.8047	0.0321	0.0175	15	
15	1.8233	1.7969	0.0264	0.0145	13	
16	1.8588	1.8368	0.0220	0.0119	14	

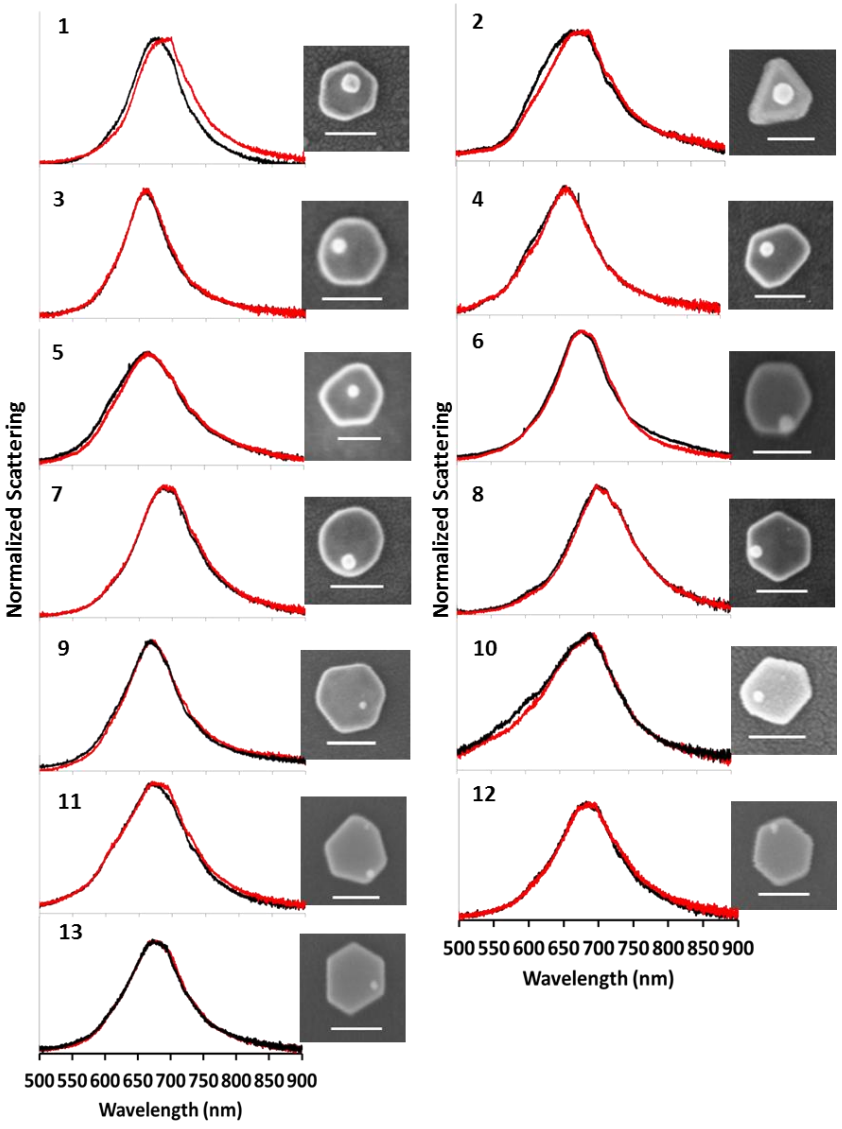

Figure 5.5 *Scattering spectra of 13 single Au NPs before (black line) and after (red line) attachment of a Au NS on a terrace site, as shown by the SEM image to the right. Scale bars represent 100 nm in all SEM images.*

Table 5.2 *Localized surface plasmon resonance (LSPR) frequencies and scanning electron microscopy (SEM) images of 13 representative constructs consisting of a Au nanoplate (NP) with a Au nanosphere (NS) attached on the terrace.*

	Initial ω_{max} (eV)	Final ω_{max} (eV)	Red-shift (eV)	Fractional Energy Shift	NS Size (nm)	Morphology
1	1.8368	1.8047	0.0321	0.0175	43	
2	1.8287	1.8021	0.0266	0.0145	41	
3	1.8871	1.8814	0.0057	0.0030	25	
4	1.8814	1.8757	0.0057	0.0030	26	
5	1.8785	1.8672	0.0113	0.0060	24	
6	1.8260	1.8179	0.0080	0.0044	23	
7	1.8073	1.8021	0.0053	0.0029	29	
8	1.7537	1.7487	0.0049	0.0028	25	
9	1.8588	1.8560	0.0028	0.0015	10	
10	1.7891	1.7865	0.0026	0.0014	15	
11	1.8395	1.8341	0.0054	0.0030	12	
12	1.8153	1.8126	0.0027	0.0015	13	
13	1.8341	1.8287	0.0054	0.0029	14	

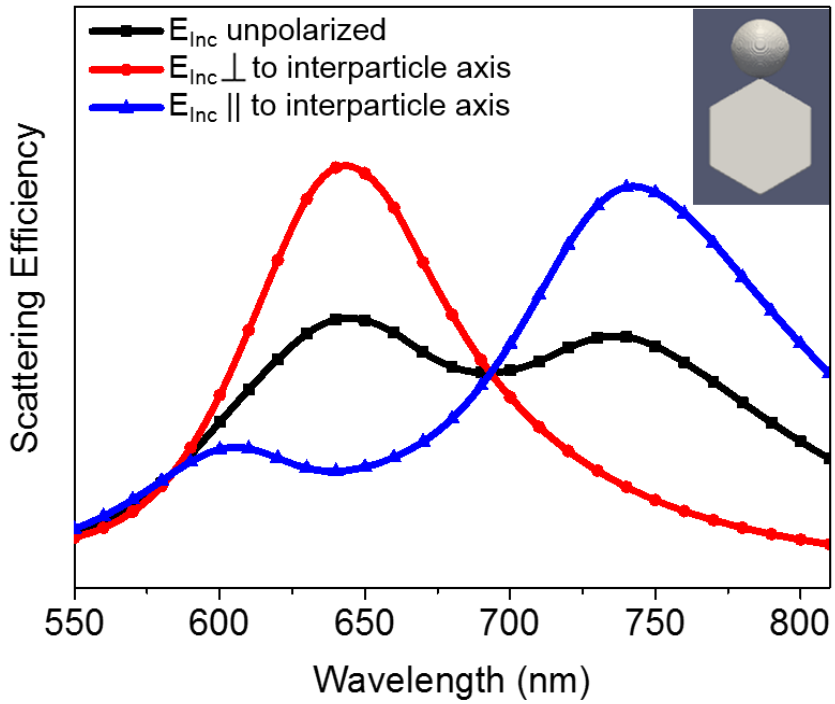

Figure 5.6 *Simulated effect of incident light polarization on the plasmon coupling between a Au NP and a 67 nm Au NS attached to a vertex on the side of the NP (structure shown in the inset)***.** *Simulations were performed for a hexagonal Au NP with a long-axis length of 137 nm, a thickness of 31 nm, and a 1-nm thick ligand shell of HT and 4-ATP, representative of the experimental structure. The distance between the surfaces of the NP and the NS was 1 nm. Wavelength maxima were determined by fitting to single or double Voigt functions. When the excitation light is polarized perpendicular the interparticle axis (red data-points connected by a spline), coupling with the NS red-shifts the dipolar mode of the NP by 3 nm relative to* λ_{max} *of 642 nm for the uncoupled NP (data not shown here). On the other hand, when light is polarized parallel to the interparticle axis (blue data-points connected by a spline), there is a red shift of 102 nm of the dipole mode and the emergence of a quadrupole mode that is blue shifted 40 nm relative to the peak maximum of the uncoupled NP. With unpolarized light excitation (black data-points connected by a spline), the scattering spectrum is a combination of these three plasmonic modes.*

5.7 References

1. Xu, W., Kong, J. S. & Chen, P. Probing the catalytic activity and heterogeneity of Au-nanoparticles at the single-molecule level. *Phys. Chem. Chem. Phys.* **11,** 2767–78 (2009).

2. Routzahn, A. L. & Jain, P. K. Single-nanocrystal reaction trajectories reveal sharp cooperative transitions. *Nano Lett.* **14,** 987–992 (2014).

3. Smith, J. G., Yang, Q. & Jain, P. K. Identification of a critical intermediate in galvanic exchange reactions by single-nanoparticle-resolved kinetics. *Angew. Chemie - Int. Ed.* **53,** 2867–2872 (2014).

4. Talapin, D. V., Lee, J. S., Kovalenko, M. V. & Shevchenko, E. V. Prospects of colloidal nanocrystals for electronic and optoelectronic applications. *Chem. Rev.* **110,** 389–458 (2010).

5. Tang, J. *et al.* Heavy-metal-free solution-processed nanoparticle-based photodetectors: Doping of intrinsic vacancies enables engineering of sensitivity and speed. *ACS Nano* **3,** 331–338 (2009).

6. He, X. *et al.* Gold nanoparticle-based fluorometric and colorimetric sensing of copper(II) ions. *Adv. Mater.* **17,** 2811–2815 (2005).

7. Byers, C. P. *et al.* Single-particle spectroscopy reveals heterogeneity in electrochemical tuning of the localized surface plasmon. *J. Phys. Chem. B* **118,** 14047–14055 (2014).

8. Joshi, G. K. *et al.* Ultrasensitive photoreversible molecular sensors of azobenzene- functionalized plasmonic nanoantennas. *Nano Lett.* **14,** 532–540 (2014).

9. Xiong, Y. *et al.* Understanding the role of oxidative etching in the polyol synthesis of Pd nanoparticles with uniform shape and size. *J. Am. Chem. Soc.* **127,** 7332–7333 (2005).

10. Lee, Y. *et al.* Large-Scale Synthesis of Uniform and Crystalline Magnetite Nanoparticles Using Reverse Micelles as Nanoreactors under Reflux Conditions. *Adv. Funct. Mater.* **15,** 503–509 (2005).

11. Khoury, C. G., Norton, S. J. & Vodinh, T. Plasmonics of 3-D nanoshell dimers using multipole expansion and finite element method. *ACS Nano* **3,** 2776–2788 (2009).

12. Kim, D. S. *et al.* Real-space mapping of the strongly coupled plasmons of nanoparticle dimers. *Nano Lett.* **9,** 3619–3625 (2009).

13. Jain, P. K., Eustis, S. & El-Sayed, M. A. Plasmon coupling in nanorod assemblies: Optical absorption, discrete dipole approximation simulation, and exciton-coupling model. *J. Phys. Chem. B* **110,** 18243–18253 (2006).

14. Sebba, D. S., Mock, J. J., Smith, D. R., LaBean, T. H. & Lazarides, A. A. Reconfigurable core-satellite nanoassemblies as molecularly-driven plasmonic switches. *Nano Lett.* **8,** 1803–1808 (2008).

15. Yoon, J. H., Zhou, Y., Blaber, M. G., Schatz, G. C. & Yoon, S. Surface plasmon coupling of compositionally heterogeneous core-satellite nanoassemblies. *J. Phys. Chem. Lett.* **4,** 1371–1378 (2013).

16. Prodan, E., Radloff, C., Halas, N. J. & Nordlander, P. A hybridization model for the plasmon response of complex nanostructures. *Science* **302,** 419–422 (2003).

17. Liu, N. *et al.* Magnetic plasmon formation and propagation in artificial aromatic molecules. *Nano Lett.* **12,** 364–369 (2012).

18. Barrow, S. J., Wei, X., Baldauf, J. S., Funston, A. M. & Mulvaney, P. The surface plasmon modes of self-assembled gold nanocrystals. *Nat. Commun.* **3,** 1275 (2012).

19. Hao, E. & Schatz, G. C. Electromagnetic fields around silver nanoparticles and dimers. *J. Chem. Phys.* **120,** 357–366 (2004).

20. Nordlander, P., Oubre, C., Prodan, E., Li, K. & Stockman, M. I. Plasmon hybridization in nanoparticle dimers. *Nano Lett.* **4,** 899–903 (2004).

21. Reinhard, B. M., Sheikholeslami, S., Mastroianni, A., Alivisatos, a P. & Liphardt, J. Use of plasmon coupling to reveal the dynamics of DNA bending and cleavage by single EcoRV restriction enzymes. *Proc. Natl. Acad. Sci. U. S. A.* **104,** 2667–2672 (2007).

22. Yang, L., Wang, H., Yan, B. & Reinhard, B. M. Calibration of silver plasmon rulers in the 1-25 nm separation range: Experimental indications of distinct plasmon coupling regimes. *J. Phys. Chem. C* **114,** 4901–4908 (2010).

23. Liu, S. D. & Cheng, M. T. Linear plasmon ruler with tunable measurement range and sensitivity. *J. Appl. Phys.* **108,** (2010).

24. Reinhard, B. M., Siu, M., Agarwal, H., Alivisatos, A. P. & Liphardt, J. Calibration of dynamic molecular rulers based on plasmon coupling between gold nanoparticles. *Nano Lett.* **5,** 2246–2252 (2005).

25. Jain, P. K., Huang, W. & El-Sayed, M. A. On the universal scaling behavior of the distance decay of plasmon coupling in metal nanoparticle pairs: A plasmon ruler equation. *Nano Lett.* **7,** 2080–2088 (2007).

26. Su, K. H. *et al.* Interparticle coupling effects on plasmon resonances of nanogold particles. *Nano Lett.* **3,** 1087–1090 (2003).

27. Sonnichsen, C., Reinhard, B. M., Liphard, J. & Alivisatos, A. P. A molecular ruler based on plasmon coupling of single gold and silver nanoparticles. *Nat. Biotechnol.* **23,** 741–745 (2005).

28. Chen, J. I. L., Chen, Y. & Ginger, D. S. Plasmonic nanoparticle dimers for optical sensing of DNA in complex media. *J. Am. Chem. Soc.* **132,** 9600–9601 (2010).

29. Liu, G. L. *et al.* A nanoplasmonic molecular ruler for measuring nuclease activity and DNA footprinting. *Nat. Nanotechnol.* **1,** 47–52 (2006).

30. Rong, G., Wang, H. & Reinhard, B. M. Insights from a nanoparticle minuet: Two-dimensional membrane profiling through silver plasmon ruler tracking. *Nano Lett.* **10,** 230–238 (2010).

31. Jun, Y. *et al.* Continuous imaging of plasmon rulers in live cells reveals early-stage caspase-3 activation at the single-molecule level. *Proc. Natl. Acad. Sci. U. S. A.* **106,** 17735–17740 (2009).

32. Liu, N., Hentschel, M., Weiss, T., Alivisatos, A. P. & Giessen, H. Three-Dimensional Plasmon Rulers. *Science (80-.).* **332,** 1407–1410 (2011).

33. Elghanian, R., Storhoff, J. J., Mucic, R. C., Letsinger, R. L. & Mirkin, C. a. Selective colorimetric detection of polynucleotides based on the distance-dependent optical properties of gold nanoparticles. *Science* **277,** 1078–1081 (1997).

34. Brown, L. V., Sobhani, H., Lassiter, J. B., Nordlander, P. & Halas, N. J. Heterodimers: Plasmonic properties of mismatched nanoparticle pairs. in *ACS Nano* **4,** 819–832 (2010).

35. Fang, A., White, S., Jain, P. K. & Zamborini, F. P. Regioselective plasmonic coupling in

metamolecular analogs of benzene derivatives. *Nano Lett.* **15,** 542–548 (2015).

36. Ross, B. M., Waldeisen, J. R., Wang, T. & Lee, L. P. Strategies for nanoplasmonic core-satellite biomolecular sensors: Theory-based Design. *Appl. Phys. Lett.* **95,** (2009).

37. Gandra, N., Abbas, A., Tian, L. & Singamaneni, S. Plasmonic Planet − Satellite Analogues : Hierarchical Self-Assembly of. *Nano Lett.* (2012).

38. Pierrat, S., Zins, I., Breivogel, A. & Sönnichsen, G. Self-assembly of small gold colloids with functionalized gold nanorods. *Nano Lett.* **7,** 259–263 (2007).

39. Sannomiya, T., Hafner, C. & Voros, J. In situ sensing of single binding events by localized surface plasmon resonance. *Nano Lett.* **8,** 3450–3455 (2008).

40. Hall, W. P., Ngatia, S. N. & Van Duyne, R. P. LSPR biosensor signal enhancement using nanoparticle-antibody conjugates. *J. Phys. Chem. C* **115,** 1410–1414 (2011).

41. Spadavecchia, J. *et al.* Approach for plasmonic based DNA sensing: Amplification of the wavelength shift and simultaneous detection of the plasmon modes of gold nanostructures. *Anal. Chem.* **85,** 3288–3296 (2013).

42. Göeken, K. L., Subramaniam, V. & Gill, R. Enhancing spectral shifts of plasmon-coupled noble metal nanoparticles for sensing applications. *Phys. Chem. Chem. Phys.* **17,** 422–7 (2015).

43. Poulsen, O. Polarization Calibration of a Grating Spectrometer. *Appl. Opt.* **11,** 1876–1878 (1972).

44. Jain, P. K., Ghosh, D., Baer, R., Rabani, E. & Alivisatos, a. P. Near-field manipulation of spectroscopic selection rules on the nanoscale. *Proc. Natl. Acad. Sci.* **109,** 8016–8019 (2012).

45. Jain, P. K. & El-Sayed, M. A. Plasmonic coupling in noble metal nanostructures. *Chem. Phys. Lett.* **487,** 153–164 (2010).

46. Beeram, S. R. & Zamborini, F. P. Selective attachment of antibodies to the edges of gold nanostructures for enhanced localized surface plasmon resonance biosensing. *J. Am. Chem. Soc.* **131,** 11689–11691 (2009).

47. Gole, A. & Murphy, C. J. Seed-mediated synthesis of gold nanorods: Role of the size and nature of the seed. *Chem. Mater.* **16,** 3633–3640 (2004).

48. Liu, X., Xu, H., Xia, H. & Wang, D. Rapid seeded growth of monodisperse, quasi-spherical, citrate-stabilized gold nanoparticles via H2O2 reduction. *Langmuir* **28,** 13720–13726 (2012).

49. Hostetler, M. J., Templeton, A. C. & Murray, R. W. Dynamics of place-exchange reactions on monolayer-protected gold cluster molecules. *Langmuir* **15,** 3782–3789 (1999).

50. Zhu, T., Fu, X., Mu, T., Wang, J. & Liu, Z. pH-dependent adsorption of gold nanoparticles on p-aminothiophenol-modified gold substrates. *Langmuir* **15,** 5197–5199 (1999).

51. Draine, B. T. & Flatau, P. J. Discrete-dipole approximation for scattering calculations. *J. Opt. Soc. Am. A* **11,** 1491 (1994).

52. Ochiai, T., Isozaki, K., Nishiyama, S. & Miki, K. Enhancement of self-assembly of large (>10 nm) gold nanoparticles on an ITO substrate. *Appl. Phys. Express* **7,** (2014).

53. Gabudean, A. M., Biro, D. & Astilean, S. Localized surface plasmon resonance (LSPR) and surface-enhanced Raman scattering (SERS) studies of 4-aminothiophenol adsorption on gold nanorods. in *Journal of Molecular Structure* **993,** 420–424 (2011).

54. Johnson, P. B. & Christy, R. W. Optical constants of the noble metals. *Phys. Rev. B* **6,** 4370–4379 (1972).

Outlook

Since the completion of our thermodynamic study on co-operativity in cation exchange shown in Chapter 1, subsequent studies have further explored the role of co-operativity in cation exchange reactions. A simultaneous study conducted in our lab probed the kinetics of cation exchange using single nanocrystal (NC) fluorescence of CdSe NCs exposed to Ag^+ ions. This study, conducted by Routzahn *et al.*, found that in an ensemble of NCs, cation exchange consists of sharp transitions of individual NCs from CdSe to Ag_2Se, rather than a slow simultaneous transition of all NCs through a continuous range of alloy compositions/solid solutions.[1] Reaction "waiting times" for each individual NC transition revealed a peaked distribution for the NC ensemble suggesting that each NC transition is limited by a critical intermediate rather than through a diffusion limited exchange mechanism. These results support the co-operative mechanism of cation exchange as proposed in our study. In 2014, Ott *et al.* published a density functional theory (DFT) study in which they found that although single or initial events in cation exchange (the creation of a cationic vacancy and substitution with another aliovalent cation) are energetically costly, Coulomb interactions with neighboring charged impurities from prior exchange events can lower the energetic barrier, which supports what we proposed in 2013.[2]

The agreement of our data with an analytical co-operative reaction model, presented in our 2013 paper, provides phenomenological evidence. However, there are still questions about the precise atomistic-level manner in which such co-operativity manifests itself. There is need for better resolution of the energetics and structure of an NC undergoing exchange. Subsequently we investigated cation exchange of ultrasmall CdSe clusters. Through this study, we learned that surface structure and ligand chemistry affect cation exchange and can even lead to the stabilization of reaction intermediates. In this case, where we could isolate a large population of a distinct, long-lived intermediate, further structural characterization of the reaction intermediate is likely to yield insight into the nature of evolution of structure and energetics in the course of exchange.

Utilizing XRD and XPS, we were able to obtain interesting structural and chemical insights that suggest the distinct intermediate we observe is a Cu-doped CdSe cluster where Cu ions occupy interstitial positions within the cubic Se cage and the Cd sub-lattice has re-organized. However, we lack knowledge of the precise structure of the CdSe, intermediate, or how the final Cu_2Se clusters differ from larger NCs or bulk Cu_2Se. Unfortunately, determination of the atomic structure of ultrasmall nanocrystals is challenging. Although XRD is a useful tool for elucidating the crystal structure of solid-state materials, in nanomaterials, there is an inherent lack of periodicity due to the finite size of crystallites and the effects of surface

reconstruction and strain that can occur due to lower coordination of atoms at the surface. This is compounded when trying to resolve the crystallographic position of dopant atoms, which almost certainly are not periodically arranged in ultrasmall clusters. As we have shown, XRD can still be used to provide average interatomic spacings along different lattice indices in nanocrystals, but it becomes challenging to propose a structure based on these averages.

The determination of high-resolution atomic structures would also improve the insights we can make in Chapter 3. Only with this data can we understand how the structure of these ultrasmall clusters truly deviates from the structure of larger, more bulk-like NCs. In some cases, such as imaging the presence of superstructure in Cu_2Se nanoparticles, we found that HRTEM was very useful. We could clearly see the presence of a vacancy-ordered super structure in larger Cu_2Se NCs and its absence in ultrasmall clusters. One setback is that this low-throughput method is highly dependent on the orientation of each nanostructure. Electron-diffraction of nanostructures benefits from being a shorter wavelength, and hence higher resolution, probe of atomic structure than XRD. However, it suffers from the smaller sample size and shorter acquisition time typically required of the measurement. Electron beams can also damage nanocrystalline samples.

Resolution of the atomic structure of CdSe and Cu_2Se clusters will require the growth of oriented supra-crystals of these clusters and the collection of total X-ray scattering in diffraction measurements, which includes high-resolution Bragg diffraction and diffuse scattering. Total scattering can be used to determine pair distribution functions for atoms, which when combined with refined structural models will provide an atomistic structure, including information about both order and disorder in these nanomaterials.[3] The co-ordination and chemical environment of ionic species in each type of cluster could also be better resolved using other X-ray techniques including X-ray absorption fine structure (EXAFS) and x-ray absorption near-edge (XANES), which are often used to probe the chemical environment of dopants atoms.[4,5] Finally, understanding of the effect of crystallite size on the phase transition of behavior of Cu_2Se will require temperature-dependent XRD and/or total scattering measurements.

References

1. Routzahn, A. L. & Jain, P. K. Single-nanocrystal reaction trajectories reveal sharp cooperative transitions. *Nano Lett.* **14,** 987–992 (2014).
2. Ott, F. D., Spiegel, L. L., Norris, D. J. & Erwin, S. C. Microscopic theory of cation exchange in CdSe nanocrystals. *Phys. Rev. Lett.* **113,** (2014).
3. Billinge, S. J. L. & Levin, I. The problem with determining atomic structure at the nanoscale. *Science* **316,** 561–565 (2007).

4. Meulenberg, R. W. *et al.* Structure and composition of Cu-doped CdSe nanocrystals using soft X-ray absorption spectroscopy. *Nano Lett.* **4,** 2277–2285 (2004).

5. Amit, Y. *et al.* Unraveling the impurity location and binding in heavily doped semiconductor nanocrystals: The case of Cu in InAs nanocrystals. *J. Phys. Chem. C* **117,** 13688–13696 (2013).